Fabrication and Characterization of Implantable Polymer Microinterfaces

DOI:10.18136/PE.2020.746

Thesis

Anita Zátonyi

Supervisor: Zoltán Fekete, PhD

University of Pannonia

FACULTY OF ENGINEERING

Doctoral School of Chemical Engineering and Material Sciences

2020

Pannon Egyetem, Vegyészmérnöki- és Anyagtudományok Doktori Iskola

Működési Szabályzat

Idegszövetbe implantálható, polimer alapú mikroelektród-hálózatok kialakítása és vizsgálata

Az értekezés doktori (PhD) fokozat elnyerése érdekében készült a Pannon Egyetem, **Vegyészmérnöki- és Anyagtudományok** Doktori Iskolája keretében

Vegyészmérnöki- és anyagtudományok tudományágban

Írta: **Zátonyi Anita**

Témavezető: **Dr. Fekete Zoltán**

Elfogadásra javaslom (igen / nem) …….

(témavezető)

A jelölt a doktori szigorlaton ..... %-ot ért el,

Veszprém, …….

(a Szigorlati Bizottság elnöke)

Az értekezést bírálóként elfogadásra javaslom:

Bíráló neve: .... igen / nem …….

(bíráló)

Bíráló neve: .... igen / nem …….

(bíráló)

A jelölt az értekezés nyilvános vitáján …….....%-ot ért el.

Veszprém, …….

(a Bíráló Bizottság elnöke)

A doktori (PhD) oklevél minősítése…….....

Veszprém, …….

(az EDHT elnöke)

Pannon Egyetem, Vegyészmérnöki- és Anyagtudományok Doktori Iskola

Működési Szabályzat

Fabrication and Characterization of Implantable Polymer Microinterfaces

Thesis for obtaining a PhD degree in the Doktoral School of **Chemical Engineering and Material Sciences** of the University of Pannonia

in the branch name of **Chemical Engineering and Material** Sciences

Written by: **Anita Zátonyi**

Supervisor: **Zoltán Fekete**, PhD

propose acceptance (yes / no) ……
(Supervisor)

The PhD-candidate has achieved ..... % in the comprehensive exam,

Veszprém, ……
(Chairman of the Examination Committee)

As reviewer, I propose acceptance of the thesis:

Name of Reviewer: .... yes / no ……
(Reviewer)

Name of Reviewer: .... yes / no ……
(Reviewer)

The PhD-candidate has achieved .....% at the public discussion.

Veszprém, ……
(Chairman of the Committee)

The grade of the PhD Diploma ..... (..... %)

Veszprém, ……
(Chairman of UDHC)

Abstract

Fabrication and Characterization of Implantable Polymer Microinterfaces

Implantable neural prosthetics devices offer, nowadays, a promising tool in the therapy of neurodegenerative diseases and psychiatric disorders, which are non – responsive to drug treatments and it provides an effective opportunity for the restoration of lost motor functions.

The problem with state – of – the – art invasive intracortical probes is that they are fragile. Long – term reliability of these devices is questionable and still fail within months or even weeks. Lack of chronic reliability, mainly related to the foreign body reaction, is induced, at the beginning, by insertion trauma, and then exacerbated as a result of mechanical mismatch between the implanted device and the neural tissue. All these adverse inflammatory factors lead to the encapsulation of the implanted devices by astrocyte cells, and form a region depleted in neurons in the vicinity of the implant. In this PhD thesis, we have addressed this issue by showing a simple process to use a thiol – ene / acrylate softening polymer as a substrate material that changes its elastic modulus, under physiological conditions. The resulting structures are more compliant with the brain tissue thus mitigating the neuroinflammatory response during brain motions.

A well – known neural interface is the electroencephalography (EEG) that is a non – invasive technique, however high frequency signals are deteriorated due to the filtering property of the skull, and the scalp. In this PhD thesis, we have addressed this issue by demonstrating an invasive method to record electrical activity from the cortical surface of the brain by micro – electrocorticography (μECoG). The use of high density micrometer electrodes with a diameter ranging from 15 to 20 μm, provides more localized recordings, but as the recording sites' diameter decreases the impedance increases affecting quality of the recordings. In the present thesis a platinum black with high specific surface area was electrodeposited and has been used to improve the recording characteristics of small electrodes.

Multimodal recording schemes have been discovered to reveal the anatomical and functional connectivity of neuronal ensembles. In this PhD thesis two approaches were applied for the fabrication of flexible and transparent μECoG interfaces for multimodal purposes.

Összefoglaló

Idegszövetbe implantálható, polimer alapú mikroelektród-hálózatok kialakítása és vizsgálata

A neurális implantátumok részt vesznek számos neurodegeneratív betegségek és a pszichiátriai rendellenességek kezelésében, amelyek esetében gyógyszeres terápiával nem érik el a kívánt hatást. Agy – gép interfészek alkotóelemeként, gerincvelői idegi sérülések tüneti kezelését tudják biztosítani.

Az utóbbi évtizedekben, nem humán kísérletekre fejlesztett eszközök nagy része szilícium alapú, hátrányuk, hogy mechanikai tulajdonságaikban jelentősen eltérnek az agy szöveti állományától. Élettartamuk, az érintett agyszövet implantációt követő gyulladásos reakciója miatt, erősen korlátozott. Az idegentest reakció során, az implantátum körül hegszövet képződik, mely elektromos és térbeli szigetelőként viselkedik. Az eszközök élettartama szempontjából sokkal előnyösebb olyan anyagok választása, amelyek rugalmassági tulajdonságaiban jobban illeszkednek a szöveti környezethez. A doktori értekezésben tiolén/akrilát, hőre lágyuló polimerbőr készült implantátum kialakítását és a rajta végzett vizsgálatok eredményeit mutatom be. A polimer különlegessége, hogy fiziológiás körülmények között rugalmassági állandója egy nagyságrenddel csökken, így a heves immunreakció mértéke csökkenthető.

Az elektroencefalográfia (EEG) egy nem invazív, orvosi gyakorlatban alkalmazott módszer, jelentős hátrányai közé sorolhatjuk azonban, hogy a felvevő pontok igen nagy átmérővel rendelkeznek és azok is nagy távolságban helyezkednek el az idegsejtektől. A disszertációban olyan invazív, koponyacsont alá ültethető, polimer alapú implantátumok megvalósítását és tesztelését mutatom be, amelynél nem érvényesülnek az említett jelszűrő hatások. A dolgozat második felében kis geometriai átmérőjű (15-20 μm) elektródokat alkalmaztam szelektív és nagy térbeli felbontású jelelvezetésre. Az impedancia csökkentése és a jelminőség javulása érdekében, nagy fajlagos felületű platina réteget választottam le, majd hosszú távú stabilitás vizsgálatokat végeztem a rétegen *in vitro* és *in vivo* körülmények között.

Az idegrendszer anatómiai és funkcionális kapcsolatának mélyebb megértése elengedhetetlen a terápiás módszereinek kialakításához, ezért kívánatos a multimodális megközelítés, ahol az elektrofiziológia és az optikai képalkotás előnyei ötvözhetőek. A dolgozat harmadik részében flexibilis és átlátszó μECoG eszközök kialakítására és tesztelésére összpontosítottam. Poliimid és indium-ón-oxid vezető réteg segítségével kialakított eszközt alkalmaztam sikeresen intrinszik optikai jel képalkotásra. Parylene HT és ITO vezető réteg segítségével kialakított eszközt alkalmaztam sikeresen egyidejűleg elektromos jelelvezetésre és két-foton mikroszkópiás képalkotásra.

Résumé

Fabrication et caractérisation de microélectrodes polymère implantables dans le tissu neuronal

Les prothèses neurales implantables offrent un outil prometteur dans la thérapie des maladies neurodégénératives et des troubles psychiatriques, qui ne répondent pas aux traitements médicamenteux.

Le problème avec les implantables intracorticales invasives qu'elles sont fragiles. La fiabilité à long terme de ces appareils est discutable. Le manque de fiabilité chronique, principalement lié à la réaction du corps étranger, est induit, au début, par un traumatisme d'insertion, puis exacerbé par suite d'un décalage mécanique entre le dispositif implanté et le tissu neural. Dans cette thèse de doctorat, nous avons abordé cette question en montrant un processus simple pour utiliser un polymère adoucissant thiolène / acrylate comme matériau de substrat qui modifie son module élastique, dans des conditions physiologiques. Les structures résultantes sont plus conformes au tissu cérébral, atténuant ainsi la réponse neuroinflammatoire lors des mouvements cérébraux.

Une interface neuronale bien connue est l'électroencéphalographie (EEG) qui est une technique non invasive, mais les signaux haute fréquence sont détériorés en raison de la propriété de filtrage du crâne et du cuir chevelu. Dans cette thèse de doctorat, nous avons abordé cette question en démontrant une méthode invasive pour enregistrer l'activité électrique de la surface corticale du cerveau par micro-électrocorticographie (μECoG). L'utilisation d'électrodes micrométriques à haute densité avec un diamètre allant de 15 à 20 μm, fournit des enregistrements plus localisés, mais à mesure que le diamètre des sites d'enregistrement diminue, l'impédance augmente, affectant la qualité des enregistrements. Dans la présente thèse, un platine avec une surface spécifique élevée a été électrodéposé et a été utilisé pour améliorer les caractéristiques d'enregistrement de petites électrodes.

Des schémas d'enregistrement multimodaux ont été découverts pour révéler la connectivité anatomique et fonctionnelle des ensembles neuronaux. Dans cette thèse de doctorat, deux approches ont été appliquées pour la fabrication d'interfaces μECoG flexibles et transparentes à des fins multimodales. Du polyimide avec ITO a été utilisé en imagerie optique intrinsèque, et du Parylene HT avec ITO a été utilisé dans des expériences d' imagerie à deux photons. Une fois le processus de fabrication terminé, notre étude s'est concentrée sur les performances et la stabilité de l'appareil

Table of Contents

Preface

The microelectrodes act as an interface between the neural tissue and the artificial system. As microelectrodes have direct contact with biological tissue and are able to record extracellular biopotential signals or it can electrically stimulate neural tissue, they provide a powerful tool in the therapy of neurodegenerative diseases and psychiatric disorders (eg. Parkinson's disease, essential tremor). Substituting stiff, inorganic materials (eg. silicon) with soft, organic polymer materials (eg. polyimide) and combining their technology with standard microfabrication processes, allows the fabrication of considerably tiny and structurally diverse neurointerfaces.

The present thesis

The first *Chapter*, General Introduction, will present an overview of basic aspects related to the forthcoming chapters, starting from the understanding of the nervous system and the generation of neural electrical signals. As every neural interface presented in this thesis is for electrophysiological recording purposes, one part is dealing with the Requirements for Recording Electrodes and Materials for Implantable Devices. Substrate and conductive materials have been selected to best fulfill the requirements posed towards them, one part is giving an overview about Materials for Implantable Devices, pointing out the importance of the materials choice for the neuroimplantable devices.

The second *Chapter* is divided into three large groups (sub – *Chapter*), based on three different research objectives. At the beginning of each sub – *Chapter* there will be a short Introduction related strictly to the specific topic, and at the end of each sub – *Chapter* there will be a Discussion and a Conclusion about the main results achieved along the course of the related topic.

Main goals of the dissertation:

1) The sub – *Chapter* of Softening Polymer – based Implantable Microprobes, will focus on intracortical neural probes made of thiol – ene / acrylate softening polymer that change their elastic modulus under physiological conditions. These are promising candidates to mitigate neuroinflammatory response due to the reduced mechanical mismatch between the artificial interface and the brain tissue. Reliability of brand new packaging technology is presented. Electrochemical stability of the proposed material composition is demonstrated and its recording performance in the hippocampus of rats is investigated.

2) The sub – *Chapter* of Durability of Platinum Black Coatings on Neural Electrodes, will focus on the investigation of electrodeposited platinum black and its stability on flexible neural interfaces (intracranial EEG and softening polymer – based microprobes). The attainable impedance improvement due to specific surface area enhancement is demonstrated. As a consequence of lower impedance values, higher signal – to – noise ratio (SNR) and consequently better electrophysiological signal quality are achievable when recording neural activity. Microelectromechanical System (MEMS) processes and protocols in details are presented, in contribution to electroplated implants without crack formation of the platinum black surfaces.

3) The sub – *Chapter* of Flexible, Transparent μECoG Devices for Multimodal Neuroimaging, will focus on flexible and transparent intracranial EEG devices that can be used in combined optical – electrical measurements. The importance of material choice from the perspective of its application will be identified. Electrochemical and mechanical stability and optical characterization of the proposed material combinations will be evaluated.

CHAPTER 1

1 GENERAL INTRODUCTION

1.1 Brain signals and neural recording

1.1.1 Neurons and neural circuit

There are two main types of cells in the nervous system, neurons and glial cells. Neurons are cells that are specialized to transmit information through both electrical and chemical routes. Glial cells include oligodendrocytes, astrocytes and Schwann cells. Glial cells perform important functions in the brain, including providing structure and creating myelin sheath that speeds up action potential conduction velocity. Schwann cells provide the myelin in the periphery, while oligodendrocyte cells provide the myelin sheath in the central nervous system. Astrocytes help to set up the blood brain barrier. Glial cells can also regulate the response of synapses and neurotransmitters to injury, and likely perform many other vital functions. Our neural system is composed of nearly 100 billon cells, called neurons. Neurons come in many complex shapes, but generally they have a dendritic arbor, a cell body called soma and an axon. The soma is the metabolic center of the cell and the main site of protein synthesis. Dendrites receive information from other cells, inform the postsynaptic area for many incoming synapses. Dendrites often contain dendritic spines, which increase the surface area for synaptic connections. Each dendritic spine only receives information from one axon [1]. **Figure 1. (a)** shows a schematic of two connected neurons with their most relevant components. In the inset of **Figure 1. (a),** represents communication channel between two neurons, the so – called synapse. Electrical signals are translated into chemical signals first, then the 'information' can pass through the synaptic gap and reaches the other neuron, where the signal becomes electrical again.

1.1.2 Signal generation and propagation

A neuron is typically stimulated at dendrites and the signals spread through the soma. In resting state, there is a constant concentration difference of positively and negatively charged ions across the cell membrane. These concentration gradients are maintained by the sodium – potassium pump, which constantly brings potassium in and pumps sodium out of the cell. A permanent flow of ions is still maintained, but the net ionic transfer is zero, resulting in a constant transmembrane potential around

-70 mV (resting state potential). Excitatory signals at dendrites open ligand – gated sodium channels, and allow sodium to flow into the cell. This mechanism neutralizes some of the negative charges, and makes the membrane voltage less negative. It is known as depolarization, since the cell membrane becomes less polarized. The sodium diffuses inside the cell, and produces a current that travels toward the axon hillock. If the summation of all input signals is excitatory and is strong enough, when it reaches the axon hillock, an action potential is generated. The axon hillock is also known as the cell's "trigger zone", since action potentials usually start here after being produced by voltage – gated ion channels that are mostly concentrated at the axon hillock. Voltage – gated ion channels form paths for ions to flow in and out of the cell, and as their name suggests, are regulated by membrane voltage. At threshold, sodium – channels open quickly followed by the opening of potassium channels somewhat later. As sodium ions rush into the cell, the intracellular charge distribution becomes more positive and this further depolarizes the cell membrane. The increase in voltage in turn causes even more sodium channels to open. This positive feedback continues until all the sodium channels are open and corresponds to the rising phase of the action potential. Note that the polarity across the cell membrane is now reversed. As the action potential approaches its peak, sodium channels begin to close. By this time, the slow potassium channels are fully open. Potassium ions rush out of the cell, and the membrane voltage quickly returns to its original resting value. This corresponds to the falling phase of the action potential. Note that sodium and potassium have now switched places across the membrane. As the potassium gates are also slow to close, potassium continues to leave the cell a little longer resulting in a negative overshoot called hyperpolarization. The resting membrane potential is then slowly restored thanks to diffusion and the sodium – potassium pump [2]–[7]. Representation of action potential generation and propagation along axon can be seen in **Figure 1. (b & c)**. Action potential travels down the axon to the nerve terminal (pre – synaptic boutons). From pre – synaptic boutons, vesicles of neurotransmitters are released and the neurotransmitter can act on the post – synaptic cell.

For an action potential to be generated, the signal must be strong enough to raise the membrane potential above a threshold, typically about -55 mV. This voltage level is the minimum required to open voltage – gated ion channels, and triggers a chain reaction that causes an action potential to fire and a neuron to relay messages to its own downstream synapses. Action potentials produce an electric field that is spreading from the neuron, and can be detected by placing electrodes nearby, allowing recording information represented by a neuron.

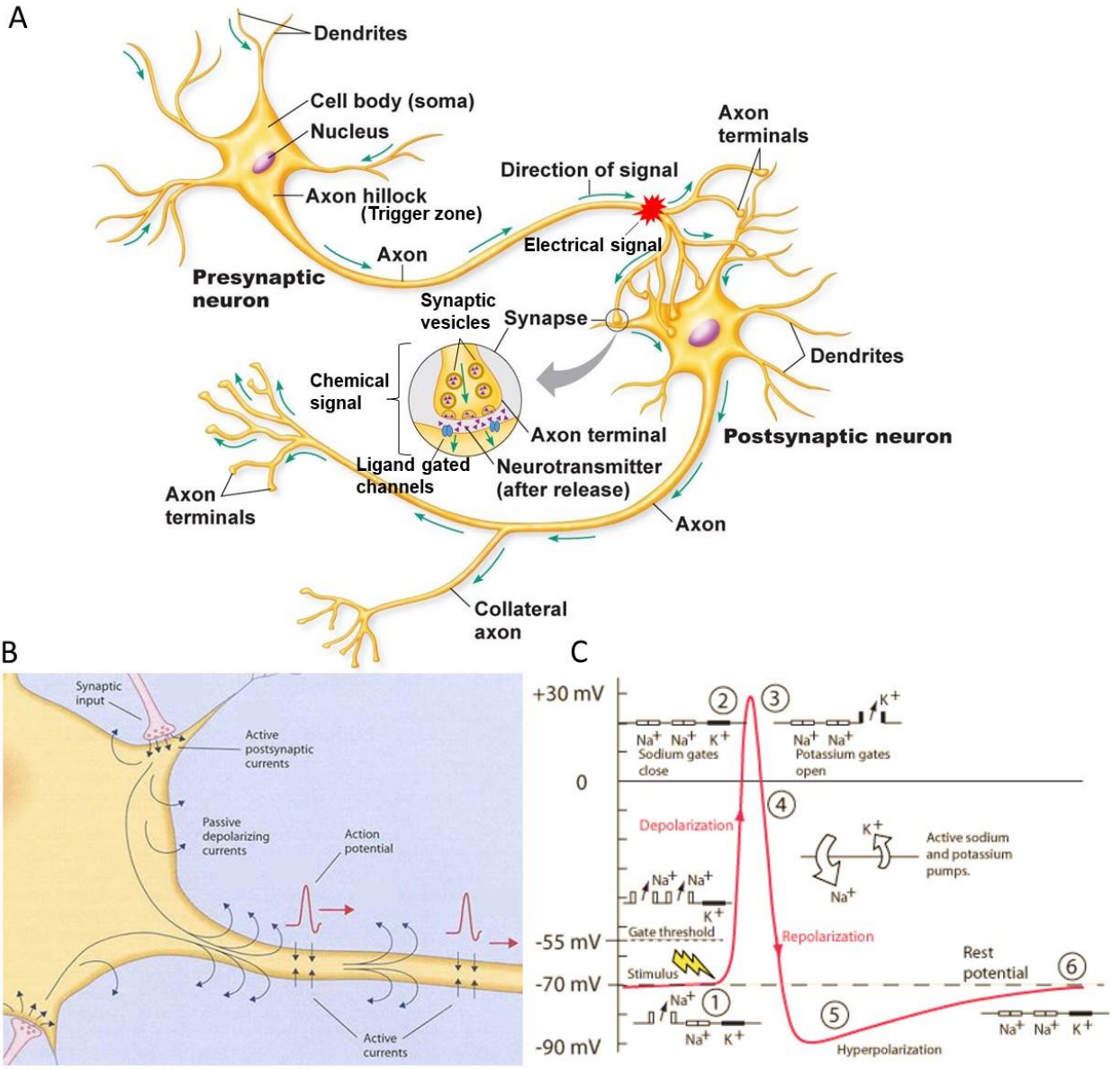

Figure 1. (a) Schematic drawing of two connected neurons, showing main structural components: axon, dendrites, synapses etc. Inset shows the communication at chemical synapses that requires the release of neurotransmitters [7]. (b) Mechanism of action potential generation and propagation along the axon [32]. (c) Time-dependent changes in membrane potential of an action potential: 1) stimulus applied, @ -55 mV the threshold reached and Na^+ channels start to open, 1) – 2) depolarization: Na^+ diffuses into the axon, the axon is more positive inside 2) - 3) @ peak Na^+ channels begin to close and K^+ channels are fully open, 4) repolarization: change from positive to negative inside, when K^+ diffuses out of the neuron, 5) refractory period or hyperpolarization, where the impulse cannot go back in the same direction, 6) slowly restore and return to resting state [6].

1.2 Fundamentals of extracellular recordings

Cerebrospinal fluid (CSF) can be approximated as an ohmic, homogenous, frequency – independent and isotropic conductor medium. With respect to the cell membrane, which has high impedance, it has a high conductivity of 1.79 S/m at body temperature (37 °C) [8]. Neural tissue can be described as an ohmic conductor medium with inhomogenity and anisotropy. Neurons generate electric field, which can be measured with a sensor placing in the vicinity of signal sources. The measurable potential of volume conduction is inversely proportional to tissue conductivity and the generated electric field degenerates quickly with distance from the neural origin [9]. The challenge of recording network activity lies in the fact that each neuron communicates hundreds or thousands of others, and interrogation of all input and output signals is physically impossible. Extracellular signals are composed of local field potentials (LFPs) with a range of frequency from a few Hz to hundreds of Hz (~1 – 300 Hz), and action potentials (APs), which are detected at higher frequencies (few kHz) and often referred to as multi – or single unit activity (SUA) or briefly "spikes". Amplitude of extracellular potential recorded from neurons is in the range of tens of microvolts [10].

1.2.1 Local field potential (LFP)

LFP is generated by synchronized low frequency summed inhibitory and excitatory postsynaptic potentials, and not only represents the superposition of action potentials, but holds information on slow glial potentials, calcium spikes after hyperpolarization phase following the action potentials [11], [12]. Recording LFP has the advantage that it characterizes population effects such as neural oscillations. Similarly to electroencephalography (EEG) recordings, electrocorticography (ECoG) mainly sample electrical activity from pyramidal cells of the cortical layers 3 and 5. ECoG recordings are composed of LFPs and in very rare cases APs as well [13].

1.2.2 Action potential (AP)

If the neural cell membrane depolarization reaches the threshold level at the axon hillock, the neuron fires and an AP is generated and propagated in its axon. Nerve cell APs have a much smaller potential field distribution than LFPs and their duration is in the range of 1 – 2 milliseconds, consequently their contribution to intracranial EEG or ECoG signals is not remarkable. Because of the electrical properties of the brain tissue, the action potentials of neurons do not spread to large distance in the extracellular space. The closer the active nerve cells are to the electrode sites, the greater the amplitude of the detected APs. Electrode sites with appropriately small recording area should be placed no greater than 50 – 60 μm far

from the neurons when the aim is to record single unit activity (or AP) and no greater than 100 – 150 μm far from electrical signal sources considering multi unit activity recordings. The amplitude and shape of the recorded spikes increases the information content of extracellular recordings by displaying the function of different active neuron types. The spiking activity of a representative fraction of the neuron population in a small volume can be monitored with a sufficiently large density of recording sites.

1.3 Requirements for recording electrodes

The role of neural recording electrodes is to measure biopotential signals, spreading in the extracellular medium in form of ionic current, and transduce them to electrical signals. This conversion involving capacitive coupling (charging and discharging of the double layer) and faradaic reactions, when molecules of the electrode material and ions in the physiologic environment exchange electrons in a redox reaction [14], [15].

The mature technology behind neuroimplantable devices makes them now promising candidates for chronic implantation even in the human brain. Several factors that are enclosed in standards, developed by international organizations as FDA (U.S. Food and Drug Administration), ISO (International Organization for Standardization), ASTM (American Society for Testing and Materials), ANSI (American National Standards Institute) have to be considered for materials characterization to reduce the potential for adverse biological effects. Among ISO ad ASTM standards, one group is predominantly relevant in the characterization of neural electrodes: ISO 10993 that is Biological evaluation of medical devices and ASTM F1980-16, which is Standard Guide for Accelerated Aging of Sterile Barrier Systems for Medical Devices. Based on international standards, neuroimplantable device materials are frequently tested in harsher – than – physiological conditions *in vitro* to assess preclinical data to demonstrate device reliability and effectiveness. Accelerated aging test method is an effective way to simulate the degradation mechanism of electrode material and determine degradation rate without longer time consumption. Our approach involves accelerated aging system, where elevated temperature was used and maintained during the whole period of experiment linked with daily impedance measurements to monitor changes in electrochemical and insulating performance of the proposed materials [16]. Rates of chemical reactions increase exponentially with increasing temperature. Based on a mathematical expression of the empirical observation, increasing the temperature by about 10 °C, roughly doubles the rate of many polymer reactions [17]. This empirical observation can be described as:

$$t_{sim} = t_{exp} \cdot Q_{10}^{\Delta T/10} \quad (1)$$

$$\Delta T = T_{exp} - T_{ref} \quad (2)$$

$t_{sim} = Simulated\ time\ (days)$

$t_{exp} = Experimental\ time\ (days)$

$Q_{10} = Aging\ factor\ for\ 10\ °C\ increase\ in\ T$

$T_{ref} = Body\ temperature = 37\ °C$

The aging factor (Q_{10}) equals two for polymer materials [18].

1.3.1 Methods of electrochemical characterization

Common techniques for electrochemical characterization of neural microelectrodes are electrochemical impedance spectroscopy (EIS) and cyclic voltammetry (CV). These techniques can be applied, when the recording of local field potentials or the acquisition of single and multiple unit activity are aimed. In spite of DC methods, EIS with its AC wave stimuli has the advantage of slightly moving the cell away from its steady state, therefore the expected ion and solvent transport from the electrolyte to the conductive film and consequently the morphological and electrochemical transformation of the film is not significant. In previous *Chapters* the phrase of *cell* refered to the microscopic living organism, from this *Chapter* the phrase of *cell* will refer to electrochemical cell the assembly where electrochemical measurement takes place, consists of electrodes, electrolyte and the potentiostat.

Electrochemical Impedance Spectroscopy (EIS)

When our system reaches the equilibrium and forms the open circuit potential, no net current flows and only thermodynamic information is available. The potentiostat allows to drive the cell away from the equilibrium potential, and thus electrochemical reaction occurs. In Electrochemical Impedance Spectroscopy (EIS) small (amplitudes < 500 μV), sinusoidal alternating current or potential of changing frequency is applied. An AC wave is defined by its frequency and amplitude. In EIS experiments, fixed amplitude and changing frequency is typically used. The frequency-dependence of different electrochemical processes allows to separate the contributions to the total response. Similarly to Ohm's law, which defines the ratio of voltage and current as the resistance, in AC methods resistance is replaced with a more generic term, impedance. Impedance can be resistance, capacitance, inductance and diffusion as well, but it still defines the relationship between voltage and current. For example, AC stimulus applied as the voltage, AC current measured as the response, and the ratio in amplitude of two waves determines

its impedance level or the magnitude of impedance. The other parameter used for the characterization of the system is the phase or phase angle, and it represents the offset between the two waves. The current either leads or lags the voltage, and the shift between them is referred as phase angle θ.

The measured impedance characterizes the interface at the working electrode and electrolyte or extracellular medium. Current flows between the working and counter electrode, while the potential difference between the working and the counter electrode is such that the working electrode potential is at a set value with respect to a reference point. Frequency range for EIS measurements is selected to cover the range of interest. In neuroscience, it scales from 1 Hz to 10 kHz, depending on the neurophysiological information of interest. For instance, local field potential signals, that are including information on slow synaptic potentials, range between 1 – 300 Hz, while single – and multiunit activity are typically resolved at higher frequencies from 300 Hz to 10 kHz [12]. Bode plots will be used for data representation and analysis, where the magnitude of impedance and phase angle are plotted as a function of frequency. Information from high-frequency electrode kinetics, and from low-frequency diffusion or mass transport region can be obtained by analyzing Bode plots. Schematic drawing of a typical three compartment electrochemical cell that was used in EIS measurements can be seen in **Figure 2**.

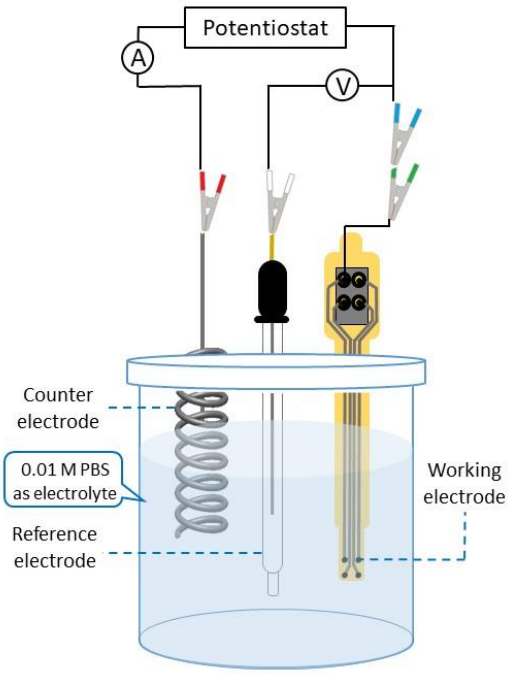

Figure 2. Schematic drawing of three compartment electrochemical cell used in EIS measurements, platinum wire as counter, Ag/AgCl as reference and one recording site of our cortical microarray as working electrode respectively.

Equivalent circuit parameters at the electrode - electrolyte interface

When an electrode is introduced to an electrolyte, it is initially electroneutral, however, chemical reactions immediately occur after. Due to these reactions, an electrical field develops that has an impact on the chemical reactions. When the competing reactions (oxidation – reduction) reach a steady-state, it is going to form an equilibrium, namely the open circuit potential. At this point currents still flow, electrochemical reactions still happen, but the net current is zero. According to the Gouy – Chapman model, the electric field also has an influence on the electrolyte, and an electrical double layer (DL) develops in the vicinity of the metal surface. The DL contains the Helmholtz planes (inner and outer) that contains ions adsorbed or electrostatically attracted to the surface and a diffuse layer. The charged metal surface attracts a layer of oriented water dipoles, which with the dehydrated (unsolved) ions adsorbed to the metal surface, defines the inner Helmholtz plane. Beyond this plane, a layer of hydrated ions is generated, closely attracted by the Coulomb force, known as outer Helmholtz plane (OHP). To sum it up, the electrochemical double layer exists, because the interface of a charged electrode in an ionic electrolyte forms a capacitor. The DL contains a less compact region that is the diffuse layer (or Gouy-Chapman layer) with mobile, solvated anions or cations distributed due to the contribution of the thermal forces and electrostatic interactions. Charge distribution of ions in a diffuse layer leads to an exponential drop of potential from the electrode surface to the bulk solution. The complete structure is electroneutral in a steady-state, since the net electric charge accumulated on the metal surfaces is balanced by the net electric charge in the diffuse layer. The theory that electrified electrode creates an interfacial charge distribution, developed by Helmholtz, resulted in the assumption that as an electrical circuit, the Helmholtz plane behaves like a parallel capacitor (linear potential drop across the Helmholtz plane), known as Helmholtz capacitance (C_H):

$$C_H = \frac{\varepsilon_0 \varepsilon_r A}{d_{OHP}} \tag{3}$$

$C_H = Helmholtz\ capacitance\ (pF)$

$\varepsilon_0 = Dielectric\ constant\ of\ vacuum$

$\varepsilon_r = Dielectric\ constant\ of\ the\ electrolyte$

$A = Surface\ area\ of\ the\ electrode\ (nm^2)$

$d_{OHP} = Distance\ from\ the\ OHP\ to\ the\ metal\ electrode\ (nm)$ = 0.2-0.5 nm (order of an ionic radius)

Considering the influence of thermal forces on the mobile ions in addition to the electric forces, a charge spread in an ionic cloud is formed near the interface. Distribution of diffused ions is taken into account with the Gouy – Chapman (diffusion) layer, where the potential drop is no longer linear, and with the Gouy – Chapman capacitance (C_G):

$$C_G = \frac{\varepsilon_0 \varepsilon_r}{L_D} cosh\left(\frac{zV_0}{2V_T}\right) \tag{4}$$

$C_G = Gouy - Chapman\ capacitance\ (pF)$

$L_D = Debye\ length\ (nm)$

$V_0 = Applied\ potential\ (V)$

$V_T = Thermal\ voltage\ (V)$

$z = Number\ of\ electrons\ exchanged\ in\ the\ redox\ reaction$

In the equation L_D was used to represent the spatial decay of the potential:

$$L_D = \sqrt{\frac{\varepsilon_0 \varepsilon_r V_T}{2 n_0 z^2 q}} \tag{5}$$

$n_0 = Concentration\ of\ ions\ in\ the\ bulk\ solution\ (^{ion}/_{m^3})$

$q = Charge\ of\ the\ ion$

The overall interface capacitance (C_I) is the combination of C_H in series with C_G:

$$\frac{1}{C_I} = \frac{1}{C_H} + \frac{1}{C_G} \tag{6}$$

This ideal model is proposed for perfectly smooth electrode surfaces, however, the experimental conditions are never ideal. In order to model the imperfect or leaky capacitors due to the frequency dispersion, a new circuit element was introduced to substitute the interfacial capacitance, known as Constant Phase Element (C_{CPE}). CPE is used as a replacement for the interfacial capacitance (C_I) will always give a better fit to data, simply because offers one extra degree of freedom [19], therefore there is a single element fit with two different parameters. Impedance of a capacitor scales inversely with frequency, and this impedance of a CPE is expressed as:

$$Z_{CPE}(\omega) = \frac{1}{Y(i\omega)^{\alpha}} \tag{7}$$

$\omega = Angular\ frequency\ \left({}^{rad}/_{sec}\right);\ \omega = 2\pi f\ (f = frequency\ in\ Hz)$

$Y = Coefficient\ of\ CPE\ (S * s^{\alpha})(frequency - independent\ parameter)$

$i = Imaginary\ unit$

$\alpha = Constant\ (frequency - dependent\ parameter)$

Constant α represents a ratio between capacitive and resistive behaviour of a non-ideal double layer formed on the surface of the conductive material, and it scales between $0 \leq \alpha \leq 1$. When $\alpha = 1$, the equation describes the impedance of a pure capacitor, the coefficient $Q^{\alpha} = C$ (the capacitance), and the measurable phase angle is -90°. For real surfaces with inhomogenities, the double-layer behaves like a CPE with $\alpha < 1$. For $\alpha = 0$ CPE defines a pure resistance and for $\alpha = 0.5$, it defines a Warburg element.

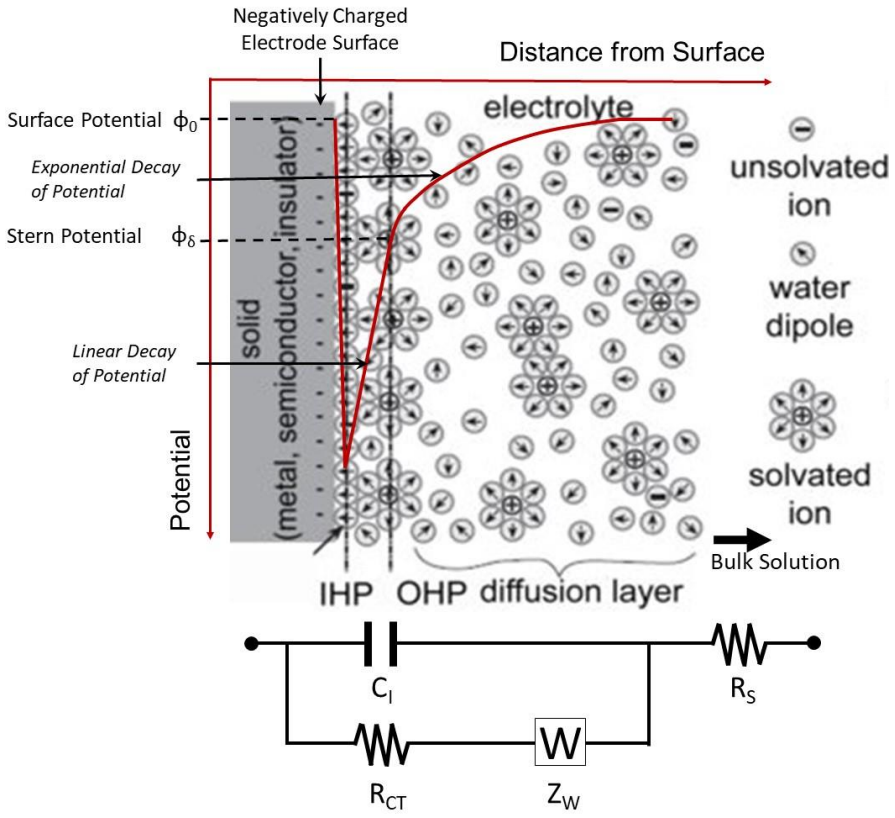

Figure 3. Schematic illustration of the electrode-electrolyte interface after the cell was driven away from its equilibrium (polarized). The inner Helmholtz or hydration layer contains ions adsorbed or electrostatically attracted to the surface, the outer Helmholtz layer contains hydrated (solvated) ions electrostatically attracted to the electrode's surface as well. This double layer is followed by the diffuse layer contains mobile (solvated) ions. At the bottom equivalent circuit can be found with parameters as electrical representation of different interfacial layers. Copied and modified from [285].

There are various theories that explain the physical correlation of α with surface roughness, charge uniformity, bulk properties of the coating or fluctuation of reaction rates along the electrode surface [20], [21]. The correlation between α and θ is given by

$$\alpha = \frac{2\theta}{\pi} \tag{8}$$

C_{CPE} is proportional to the electrode surface area and the impedance goes with $\frac{1}{A\frac{\omega}{2\pi}}$ because of **Equation 3**.

Impedance of a given capacitor is higher when observing the lower frequency regions, and lower when at higher frequencies, therefore the interfacial capacitance (or C_{CPE}) is the major contribution factor to the total response at lower frequencies. In order to describe the surface conditions in a more realistic way, another circuit parameter needs to be integrated in parallel to the capacitive elements, known as Charge-Transfer Resistance (R_{CT}). R_{CT} corresponds to faradaic reactions at the interface, lead to a net current flow across the electrode-electrolyte interface. Simplified equation of R_{CT} for small signals is the following:

$$R_{CT} = \frac{RT}{zFJ_0} = \frac{V_T}{zJ_0} \tag{9}$$

$R = Universal\ gas\ constant\ = 8.314\ {}^{J}/_{molK}$

$T = Absolute\ temperature\ (K)$

$z = Number\ of\ electrons\ exchanged\ in\ the\ redox\ reaction$

$F = Faraday's\ constant = 96{,}485\ \left({}^{C}/_{mol}\right)$

$V_T = Thermal\ voltage\ (V)$

$J_0 = Exchange\ current\ density\ \left({}^{A}/_{m^2}\right)$

Both C_{CPE} and R_{CT} are in the model to characterize the surface properties. I assume linear behaviour of the R_{CT} when measuring impedance *in vivo* or *in vitro*, where the applied potential is zero or the potential is a small constant (eg. 25 mV) value, respectively. Besides the above described circuit parameters, further element, resistance of the solution or physiological environment, has to be taken into account. Spreading resistance (R_S) is placed in series to the impedance of the interface. **Equation 10.** describes R_S for circular electrode, which scales with $\frac{1}{\sqrt{A_{geo}}}$:

$$R_S = \frac{\rho\sqrt{\pi}}{4\sqrt{A_{geo}}} \tag{10}$$

$\rho = Resistivity\ of\ the\ electrolyte\ (S)$

$A_{geo} = Geometric\ surface\ area\ of\ the\ electrode\ (nm^2)$

R_S generally describes the resistance of the bulk electrolyte combined with the internal, ohmic resistance of the metal contact sites and wiring of the working electrode. At high frequencies, ions are not able to follow the alternating electric field. Warburg element representing the frequency dependent impedance to ionic diffusion. Warburg impedance (Z_W) is defined as:

$$Z_W = (1 - i)\frac{\sigma}{\sqrt{\omega}} \tag{11}$$

$i = Imaginary\ unit$

$\sigma = Warburg\ constant\ \left(\Omega/\sqrt{sec}\right)$

$\omega = Angular\ frequency\ \left(rad/sec\right)$

Although the effects of electrode impedance to the amplitude of extracellular recording and background noise is not thoroughly understood [22], we cannot ignore the effects of noise on the recorded waveforms. Most theories and experiments indicate that decreased impedance results in improved recording and stimulation capabilities [13], [23]–[26]. Thermal noise is thought to be the dominant noise source when performing cortical recording due to the high impedance of recording sites. Thermal noise arises from the thermal fluctuations of charge carriers within a conductor, and its root – mean – square (RMS) is proportional to the square root of resistive component of the impedance (marked as *R* in the equation). Thermal noise (Johnson – Nyquist noise, Johnson noise, or Nyquist noise) can be defined as:

$$v_{RMS} = \sqrt{4k_B TR\Delta f} \tag{12}$$

$v_{RMS} = Root - mean - square\ noise\ voltage\ (V)$

$k_B = Boltzmann\ constant\ = 1.38 \cdot 10^{-23}\ J/K$

$T = Absolute\ temperature\ (K)$

$R = Resistive\ component\ of\ the\ impedance\ or\ Resistance\ (\Omega)$

$\Delta f = Bandwidth\ of\ frequency\ (Hz)$

Schematic illustration and the inferred equivalent circuit parameters of the polarized electrode – electrolyte interface can be seen in **Figure 3**.

Cyclic voltammetry (CV)

Cyclic voltammetry is used for the characterization of the reactions on the electrode surface and for the assessment of stability on the deposited electroactive surface. It is also a powerful tool for reliable, homogenous electrochemical deposition of porous conductive films from its solution. Similarly to EIS, cyclic voltammetry measurements are carried out in three compartment electrochemical cells. The applied potential is cycled at a constant rate between two defined potential limits, while the current flows between the working electrode (in which the potential is applied with respect to a noncurrent-carrying reference electrode) and the counter electrode. The applied potential at the working electrode gives rise to electrochemical reactions eg. transport of charges through the test electrode – electrolyte surface, resulted in a measurable current. The position of measured current peaks gives quantitative information, while the area under current peaks provides qualitative information on the amount of charges transferred during the anodic (oxidation) or cathodic (reduction) reactions [27], [28].

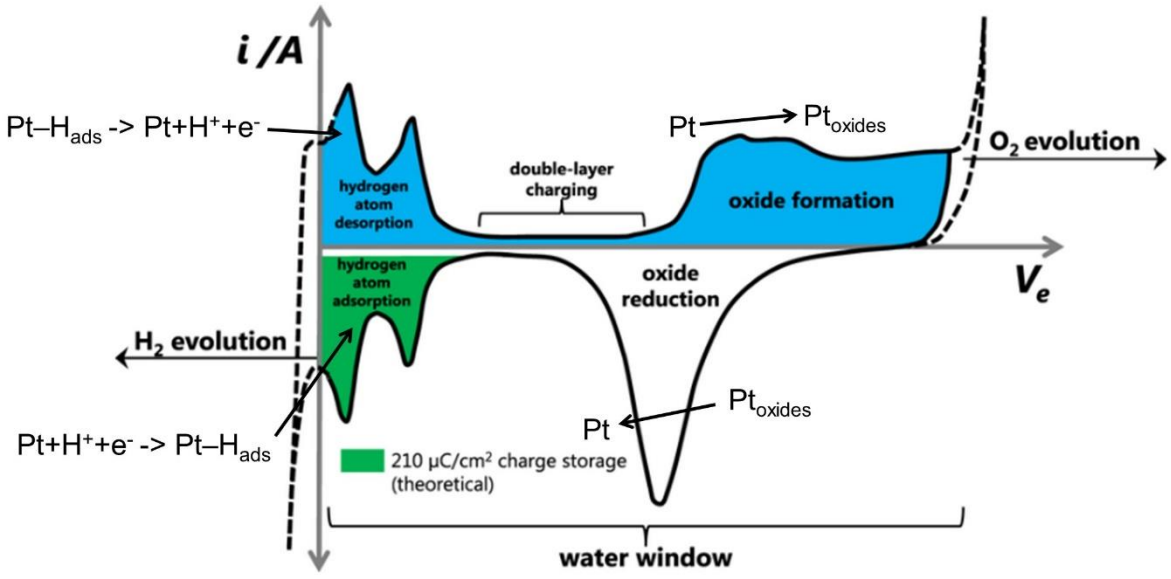

Figure 4. Typical cyclic voltammogram of a porous platinum electrode. This figure was copied and modified from [286].

1.3.2 Strategies for higher signal – to – noise ratio (SNR)

Increasing the geometric surface area of the recording sites to reduce the impedance, would result in poor spatial localization of recorded action potentials from a neuronal ensemble. Geometric area improvement is also limited by the dimensions of microdevices. With smaller recording sites, it is possible to obtain higher spatial resolution by reducing the amount of spatial averaging of the LFP signals. For single-unit recording the microelectrode geometric surface area for penetrating probes should be maximum 2000 – 4000 μm^2 (d = 50 – 70 μm) or much smaller [15]. As the site diameter decreases, the impedance increases. Higher impedance values contribute to lower signal – to – noise ratio (SNR), resulted in less sensitive recording where strong electrical noise components (eg. 50 Hz) suppress useful signals. In order to measure single-unit neural activity, the SNR should be above 5:1, and the impedance of recording electrodes should be between 50 kΩ to 1 MΩ at 1 kHz [15]. A trade-off has to be found between high spatial resolution (selectivity) and high SNR (sensitivity) of the recording. A feasibly strategy is the deposition of porous inorganic (eg. platinum black, [29]–[31]) or organic (eg. Poly(3,4-ethylenedioxythiophene) (PEDOT) [20], [32]–[37]) materials on sputtered, evaporated metal surfaces or on carbon nanotubes, nanowires. It is also an appropriate solution to nanostructure the conductive layer [38], [39]. This strategy enables small geometric surface area with increased electroactive area via the increased surface roughness of the electrode sites.

The electroactive surface area represents the surface area of an electroconductive material accessible for the electrolyte [40]. The deposited porous layer causes an extension in electroactive surface area. The improvement in effective surface area is characterized by the roughness factor. The roughness factor or the extent of inhomogenity, is determined by dividing the established effective surface area by the geometric surface area of an ideally flat, homogenous and polycrystalline metal electrode (standard value for platinum is 210 $\mu C/cm^2$ [41]). The amount of charges adsorbed on a rough surface, and consequently the electroactive surface area, is determined by analyzing the charge under the peaks of the hydrogen desorption area of cyclic voltammetric (CV) curves [42]. Both faradaic and non-faradaic currents scale linearly with the surface area, therefore improved effective surface area has an impact on equivalent circuit elements, namely the double-layer capacitance (non-faradaic) and charge-transfer resistance (faradaic). Electrical double-layer increases while resistance to charge-transfer decreases resulted in lower impedance values and consequently better SNR. A typical cyclic voltammogram of a porous platinum electrode can be seen in **Figure 4**.

To conclude this subsection, in order to obtain more localized sensing regions and better unit recording capabilities, small electrode sites of the lowest possible impedance values are needed. To lower the impedance, microscopic irregularities need to be introduced on the smooth surface of the microelectrodes for example with the electrodeposition of porous conductive materials.

1.3.3 Methods of mechanical characterization

The flexible micro – electrocorticography (μECoG) electrode arrays presented here are based on a polymer/(metal or metal – oxide)/polymer sandwich structure. Prior studies employed mostly tensile loads to evaluate the mechanical stability of the thin systems (all together few microns in thickness) [43]. To demonstrate the robustness of the proposed structures under bending loads and to identify unique failure mechanism if any occurs, an individual test procedure was developed, where integrity was measured by four wire resistance method. The repetitive deformation of these structures is simulated by cyclic bending loads. For these type of sandwiched structures, the bending stiffness is dominated by the conductive layer [44], which was placed at the neutral plane to enhance tolerance to bending loads [45]. The same strategy was applied with test structures and with ready – to – use devices.

1.4 Materials for implantable devices

In this *Chapter*, substrate and encapsulation materials for neural interfacing will be discussed. In many cases, these two layers are made of the same material composition. Substrate is the mechanical carrier for the electrical components. Substrate technology has a direct impact on achievable form factors, available assembly processes, and reliability and performance of the device. Rigid substrate technology are based on stiff materials eg. silicon (Si), glass, polyetheretherketone (PEEK) etc. Flexible substrate technology relies on flexible, mainly polymer films eg. polyimide (PI), liquid crystal polymer (LCP), poly(para – xylylene) (PPX), polydimethylsiloxane (PDMS), shape – memory polymers (SMP), nanocomposites (NCs) etc. Hybrid substrate technology offers the combination of rigid and flexible materials. In view of the rigorous clinical approval process, consideration of biological, mechanical, and material risk factors are challenging. Material for neural implants must fulfill general requirements:

- Biocompatibility
- Low toxic effect and attenuated long-term histological effects in the brain
- Flexibility (small Young's modulus and large elongation)
- Mechanical durability (high tensile strength)
- Good electrical insulation
- Low moisture absorption and permeability
- Compatible with microfabrication techniques

Besides materials choices, the U.S. Food and Drug Administration (FDA) considers other factors in their decision in order to allow devices participating in human clinical trials eg. form factor, functionality, and implantation procedure. More detailed description on each applied polymer material will be given in the introduction of the related chapters.

1.4.1 Neural recording interfaces

Neural electrodes are interfacing the biological system to record signals generated in the active region of nervous system. They provide compact readouts of potential changes caused by the electrical activity of neural ensembles. These technology provide an important tool to better understand brain functions and organization of neural structures. The recording interfaces have also shown promise in treatment of neurological disorders and mental disabilities (for patients with intractable epilepsy for presurgical brain mapping and seizure foci localization [46], in the rehabilitation of lost motor functions [47]). Combination of the biological relevance of recording interfaces with recent advances in semiconductor fabrication process or microfabrication technology results in reliably small, densely packed microelectrode system with higher spatial resolution in the horizontal plane at the surface of the cerebral cortex [48], [49]. For long-term, chronic applications, electrode materials need to be improved to fulfill several requirements demanded during the interaction with living cells and organs. These requirements are (1) material (flexibility/rigidity, biocompatibility, molecular properties of building block, easily tunable chemical composition and mechanical properties) and design (shape, physical parameters) conformity to the neural tissues, (2) facile and reliable production with conventional microfabrication technologies, that uncomplicated the manufacturing of implantable devices with, (3) reliable recording over long period of time (foreign body response depends on leachable components from electrode materials, endotoxins, size, mechanical feature etc.), (4) the ability to simultaneously record potentials from various populations of neurons. Six different types of recording electrodes can be classified in the field of neural prosthesis regarding the targeted tissue and the location of electrodes:

1. Penetrating intracortical electrodes (microwires, cortical microelectrodes or shallow probes, depth electrodes)
2. Penetrating peripheral nerve electrodes (microwires, intrafascicular electrodes, microelectrode arrays, regenerative interfaces)
3. Non-penetrating cortical electrodes (planar or ECoG electrode arrays)
4. Non-penetrating peripheral nerve electrodes (cuff electrodes)
5. Endovascular probes or stentrodes
6. Neural dust

Summary of neuroimplantable devices and their position relative to brain layers can be seen in **Figure 5**.

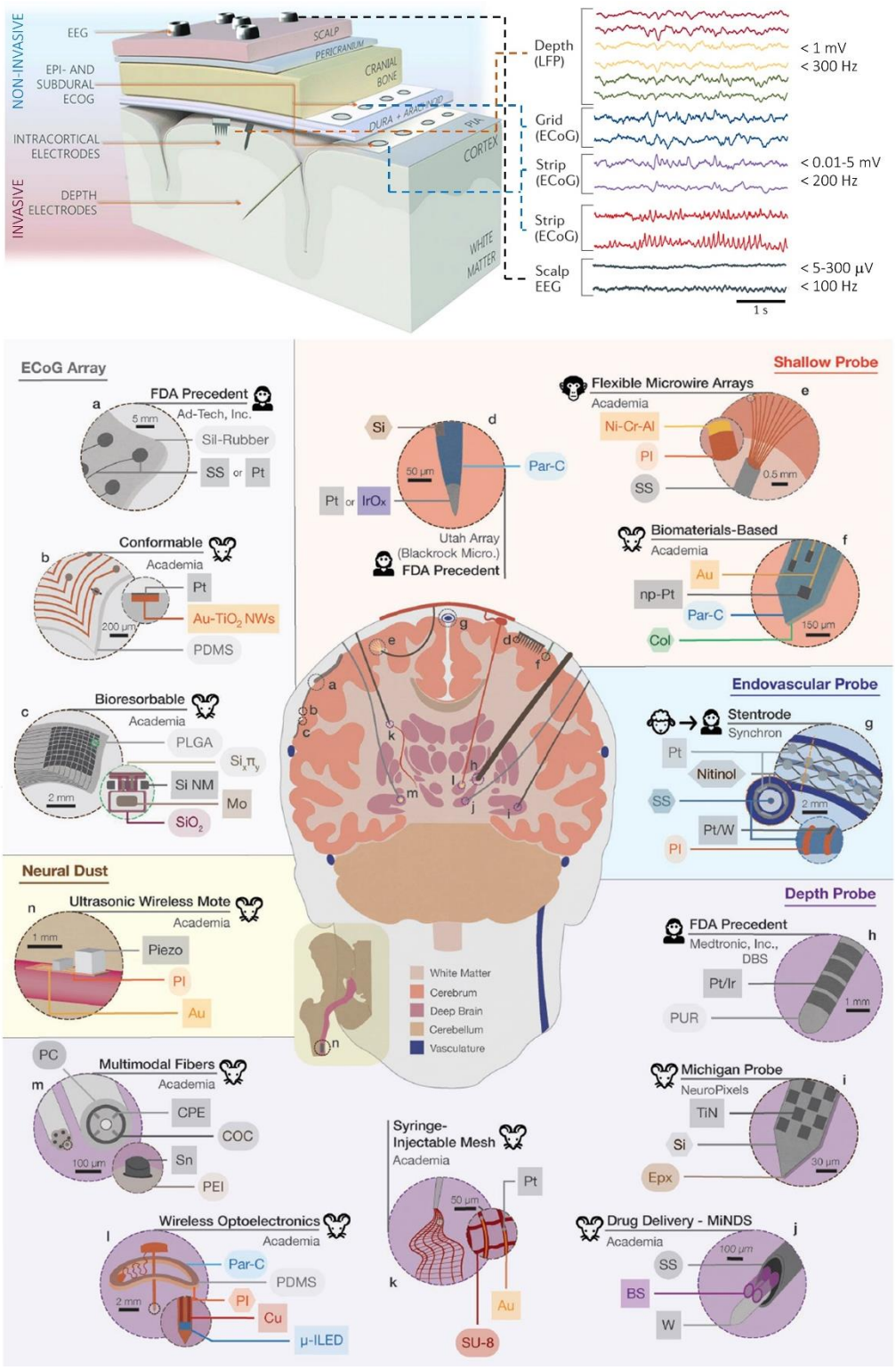

Figure 5. Invasive (purple area) & non-invasive (blue area) neural recording interfaces and their location in reference to the brain (upper-left image), copied from [287]. Waveforms measured with different electrophysiological methods and their range of amplitude & frequency, copied and modified from [11] (upper-right image). The measured signal amplitudes for ECoG electrodes are larger compared to scalp EEG electrodes, and lower compared to penetrating electrodes. Main picture: Overview of neuroimplantable devices including FDA-approved devices, recent progress in academic field, and commercially available probes for nonhuman research purposes. Copied from [52].

Penetrating microelectrodes can be divided into two main groups. First one with metal core and a glass or polymer insulating layer, where the non – insulated metal contacts define the recording sites. The second one consists of silicon core and polymer or inorganic insulation while the tip of the semiconductor needles are covered with thin film of metal layer (eg. platinum). These three – dimensional electrode arrays are embodied by the Utah arrays. The other well – known example for silicon – based multielectrode arrays are known as Michigan arrays, where several recording sites are patterned along the length on each silicon shank. By using microfabrication and semiconductor technology, the issue of imprecise location and differences in physical parameters (shape, size) of recording sites has disappeared. Michigan and Utah electrode arrays were successfully applied to record from the cortex of animal subjects [50]–[52] however, they are prone to break easily, since their core material is brittle silicon having a Young's modulus around 200 GPa. Moreover, because of the great mechanical mismatch at the interface of the array and the biological tissue, the implant causes strong immune response [53]–[57]. The localized tissue inflammation evolves as long as the array is present due to the continuous micromotion of the brain, resulted in a loss of signals at certain frequency ranges and degradation of neural recording reliability. Schematic representation of evolved foreign body immune response around stiff and compliant (flexible) probes can be seen in **Figure 6. (a & b**), from [57]. In order to address this issue and to maintain a stable recording over long period of time, more flexible materials were engineered as substrate and encapsulating layers, forming third major category among penetrating probes. These polymer materials have Young's modulus in the few MPa or GPa range (**Table 1**.).

Table 1. Summary of the most relevant physicochemical properties of common neuroimplant materials (polymers: PI – polyimide, Pary C – Parylene C, Pary HT – Parylene HT, LCP – liquid crystal polymer, PDMS – polydimethylsiloxane, SMP – shape memory polymer and Si - silicon as reference material).

		PI	Pary C	Pary HT	LCP	PDMS	SU-8	SMP	Si
Moisture absorption	**%**	0.5	< 0.1	< 0.01	0.04	0.5	0.55	n/a	-
Glass transition T (Tg)	**°C**	360	80-100	n/a	>280	n/a	200	variable	-
Thermal conductivity@RT	**W/(m*K)**	0.105	0.084	0.096	0.2	0.2	0.2	0.15-0.30	130
Linear coefficient of thermal expansion@25°C	**ppm**	3	35	36	3-50	310	52	n/a	2.6
Melting temperature (T_m)	**°C**	none	290	>500	275-330	226-232	n/a	variable	1414
Thermal stability (@ 5% wt.loss)	**°C**	620	100	450	320	200	300	<200, low pressure	-
Tensile strength	**MPa**	350	68.95	51.71	52.8 - 185 (230)	2.24-6.2	73	155-323	165-180
Young's modulus	**GPa**	8.50	2.76	2.55	8.5 - 17.2 (40.0)	$1.32\text{-}2.97*10^{-3}$	2.00	from 1.0 to 0.02-0.30	130.0-200
Elongation at break	**%**	100	200	200	1.2-7.0	600	4.80	Up to 800	-
Bulk/Volume resistivity	**Ω*cm**	$>10^6$	$8.8*10^{16}$	$2.0*10^{17}$	10^{19}-10^{20}	$6.0x10^{18}$	$7.8x10^{14}$	n/a	-

Although these values are far (several magnitudes larger) from that of the biological tissue (E_{Brain} = 3.15 – 10 kPa [57, 194], $E_{Peripheral\ Nerves}$ = 400 − 700 kPa [58], E_{Neuron} = 0.1 – 8 kPa (depending on their position in the brain) [59]). Polyimide, Parylene, PDMS, Liquid Crystal Polymers, SU-8 etc. are more compliant with the soft neural tissue than their rigid counterparts (eg. silicon), elastic modulus of different natural and artificial materials are compared in **Figure 6. (c).** Nevertheless, polymer – based neuroimplants are also biocompatible and compatible with standard microfabrication processes. Standard biocompatible metals like platinum (Pt), indium – tin – oxide (ITO), titanium (Ti), iridium (Ir) and gold (Au) that were used with silicon for neural interfaces, can be combined with polymers to form the conductive layer for recording sites, contact pads and connecting traces. Penetrating electrodes with sub – micron diameter are less invasive than traditional silicon microelectrodes. With their physical dimensions, the extent of cell damage around the probe track is less severe, which implies that the neuroinflammatory response is less intense.

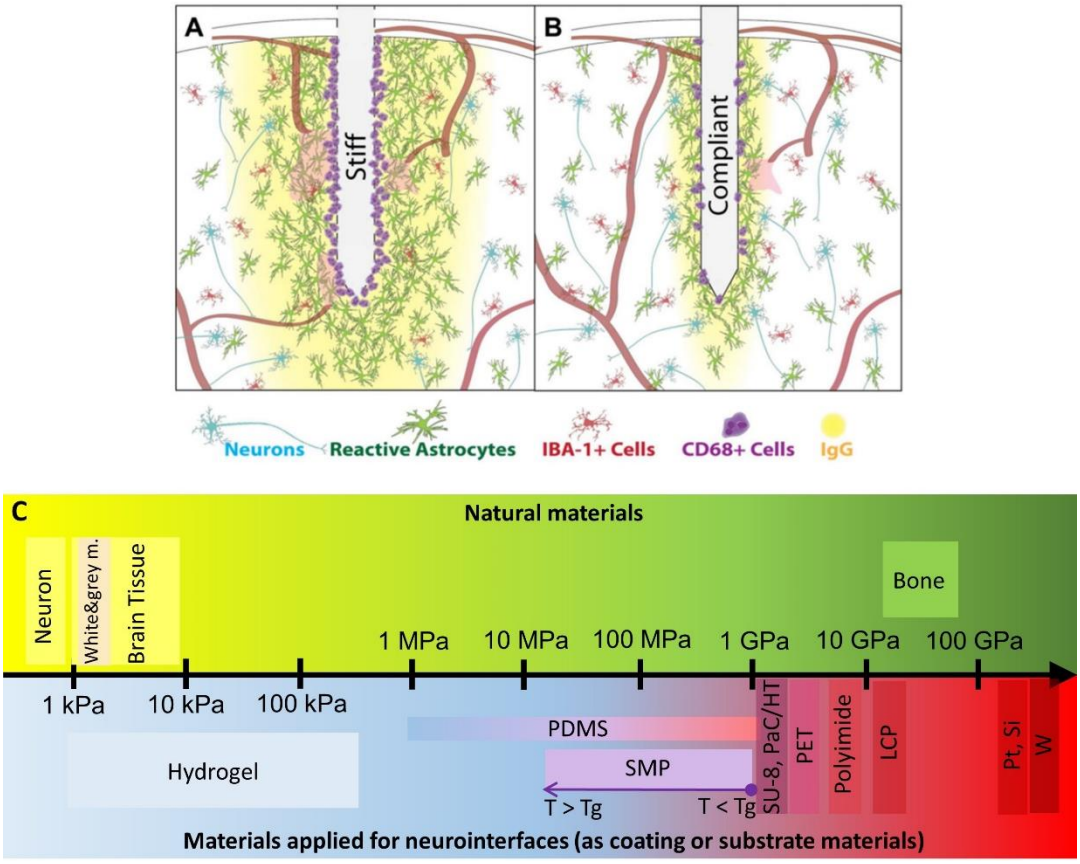

Figure 6. Schematic representation of neuroinflammatory response around stiff (a) and compliant (b) cortical implants, copied from [57]. (c) Mechanical scale representing the elastic (Young's) modulus of natural materials related to brain Cell/tissue ensembles and artificial materials applied as substrate or coating materials for neural interfaces (PDMS – Polydimethylsiloxane, SMP – Shape Memory Polymer (thiol-ene/acrylete-based), PaC/HT – Parylene C/HT, PET - Polyethylene terephthalate, LCP – Liquid Crystal Polymer, Pt – Platinum, Si – Silicon, W – Tungsten).

This feature eventually allows more reliable long – term neural recordings. On the other hand, they are tend to bend and buckle easily during the implantation procedure that is an avoidable risk factor.

The problem with state – of – the – art intracortical devices is that they are fragile and they are still penetrating the brain (invasive). Clinical neurosurgeons are very reluctant to implant such devices into the human brain, because they can easily break. The answer to this challenge was the invention of a less invasive electrocorticography (ECoG) arrays. Neural multielectrode interfaces that are able to record neural activity from the cerebral cortex can be divided into two categories: electroencephalography (EEG), and intracranial EEG (iEEG) or electrocorticography or micro – electrocorticography (ECoG or μECoG). Spatio – temporal resolution of different neural interfaces are illustrated on **Figure 7**., copied from [60].

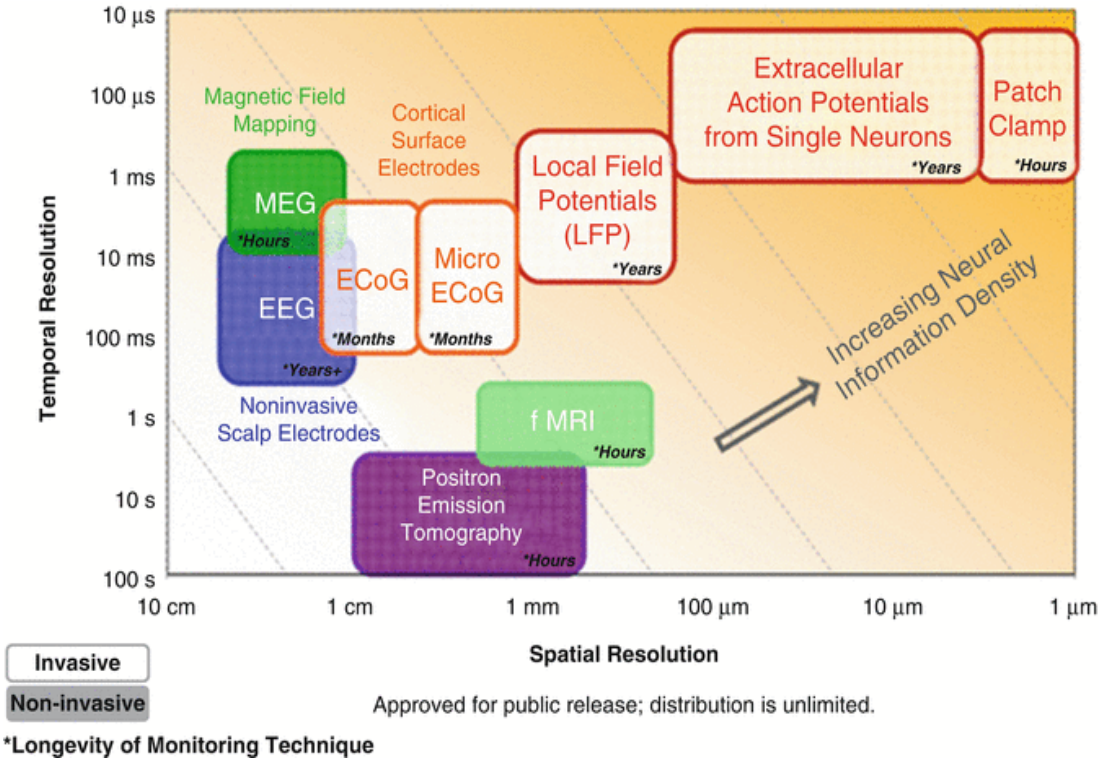

Figure 7. Demonstration of the spatio-temporal resolution of current brain monitoring technologies (including electrophysiological and brain imaging-based methods). Copied from [60] (MEG - Magnetoencephalography, EEG - Electroencephalography, ECoG - Electrocorticography, fMRI - Functional Magnetic Resonance Imaging).

EEG is a non – invasive technique, where multiple electrodes are placed on the external scalp of the experimental subject, and synchronized activity of large population of neurons is recorded. EEG electrodes are at remarkable distance from the neural cells. Due to the filtering property of skull, subcutaneous tissue

and the scalp, the signal is considerably smoothed. Information can only be acquired by applying electrodes with large contact area that means poor spatial resolution. High frequency signals are deteriorated by the skull and only low frequency components (below 60 – 80 Hz, depending on the thickness) can be captured [61]. It is notable that EEG has an excellent temporal resolution (millisecond range) among different non – invasive techniques.

Electrocorticography (ECoG) devices are placed directly onto the exposed surface of the brain, more precisely on the surface of the cerebral cortex, that is the thin, outer layer (1.5 – 5 mm) of the cerebrum [11]. ECoG can be implanted above or under the dura mater, mainly used for mapping of primary brain functions [52], discovering brain „connectome" and in human neurosurgery for the reliable localization of epileptogenic brain tissue during neurosurgery [62]–[67]. Implantation of these devices are less invasive in comparison to intracortical microelectrodes, as the brain tissue is not punctured and the evoked immune response to the artificial device is less intensive. Craniotomy is required to record signals that are composed of synchronized postsynaptic potentials [11]. By removing the skull, scalp and subcutaneous tissue, their filtering and signal attenuation effect is eliminated, creating a more information rich signals with higher spatial resolution than that of traditional EEG. When the aim is to fabricate epi– or subdural arrays that contain large number of electrodes with smaller electrode diameter, traditional techniques have proven to be very time consuming and the interelectrode spacing varied in space resulted in irregular recording patterns [68]. This irregularity complicates cortical mapping because of the spatially undefined electrode sites. With the evaluation of microfabrication processes, it has become possible to fabricate ECoG arrays assembled in a desired and predetermined way, that helps the data processing and in the localization of evoked potentials' sources [52]. Microfabrication technologies have the advantage of constructing extracellular electrode arrays (μECoG) with very high density and with a diameter below 500 μm (for human experiments) [68]. Due to the above mentioned precise location of densely packed, smaller recording sites with close proximity to neural cells, higher spatial resolution, better recording quality of high frequency activity and better SNR are available compared to EEG [69]. μECoGs are organic material – based, biocompatible devices with ultraconformable shaping possibilities (thickness of few micrometers is available), and hence the microtechnology, scalable design and fabrication is achievable with neuron – sized density (eg. 20 μm diameter, 30 μm interelectrode distance for rodents). However, the models used for data processing of EEG signals often fail when they applied for such small scales, ECoGs are still a promising candidates for the fabrication of brain – machine interfaces (BMIs) [70]–[72]. ECoG – based brain computer interfaces (BCIs) can participate in the treatment of neuromuscular disorders [73], [74] by

decoding arm trajectories and finger movements, also they can help in speech restoration [75]. To sum it up, µECoG provides an attractive tool to balance information acquisition and spatial resolution with a lower degree of invasiveness than intracortical probes [70].

1.4.2 Neural tissue and intracortical electrode interfaces

Chronic implantation of microprobes and their application in clinical practice is limited due to the immediate physiological inflammatory response of brain tissue, targeting the foreign body. This foreign body response is a major reason for device failure, since the encapsulation of the electrode by astrocyte cells forms a region depleted in neurons in the vicinity of the brain – electrode interface [76], [77], see in **Figure 6. (a & b)**. Considering the electrical properties of glial sheath, it behaves like a low – pass filter, which means the signal acquisition from single neural cells becomes challenging [78]. The adverse immune response depends on the magnitude of forces acting on the brain tissue – electrode interfaces, and its intensity scales directly with mechanical stresses. Various factors can lead to the intrinsic brain cellular immune response and consequently the loss of microprobes' functionality [79]–[81]. During implantation, low penetration forces are critical to maintain cellular density.

The magnitude of neural loss depends on mechanical properties, device geometry and surgical conditions [82], [83]. During persistent presence of microelectrodes, stresses from micromotions between the moving brain [84], [85] (eg. heart beating, breathing, circulation, gross head movement etc.) and the implanted device has been implicated as the main reason for adverse neuroinflammatory response, therefore it became one of the predominant obstacle to sustain a stable and chronic neural recording [86], [87]. Diverse strategies have been explored to alleviate neuroinflammatory response [77] and to assure extended performance of microelectrode arrays. These strategies can be divided in two major categories:

1. From biological perspective, two methods have been proposed to reduce foreign body response
    a) Application of bioactive tissue interfaces by injection or releasing of anti-inflammatory agents [88], neurotrophins (nerve growth factor [89], brain – derived neurotrophic factor [90]) into the extracellular space.
    b) Tuning the surface topography and chemistry. With this approach, the proliferation of glial cells responsible for the encapsulation could be mitigated (e.g. nanostructuring the surface of the implant [91]).

2. From material science perspective, two methods have been proposed to reduce foreign body response
    a) Application of soft, flexible materials as coating materials (eg. hydrogel) for rigid substrate-based probes or the application of polymer materials instead of stiff silicon material as structural component of intracortical probes. Both methods used to reduce elastic modulus of the proposed devices.
    b) Fabrication of ultrathin and narrow probes in order to alleviate the volume of the damaged neural tissue.

By choosing these approaches, temporal (eg. insertion shuttles or bioresorbable polymers as coatings or adhesives for shuttles) or permanent electrode support was needed to be integrated in the procedure to withstand insertion forces and not to fail during the penetration process.

Concerning geometry and design rules for neural interfaces, sharp edges should be avoided, and replaced with round edges to reduce irritation of the tissue. Typical rectangular-shaped polymer-based intracortical electrodes are 100 – 500 μm wide, 10 – 30 μm thick, and 1 – 6 mm long [53]. Sohal et al. have designed and fabricated a sinusoidal probe to minimize tethering force by reducing the movement of the recording tip relative to the surrounding tissue, therefore to improve electrode longevity [92].

A detailed explanation focusing on the second group will be given in the Introduction part of *Chapter 2*, because my work focuses on the characterization of a thiol – ene / acrylate, a mechanically adaptive polymer neural probes.

CHAPTER 2

2 SOFTENING POLYMER-BASED IMPLANTABLE MICROPROBES

2.1 Introduction

Considering the structural biocompatibility of the proposed material compositions, the mechanical properties (flexibility, elastic properties etc.) and the design principles can be adjusted to neurological purposes. The mechanical interaction between the device and the surrounding cells may be a key factor in provoking the formation of glial sheath and in hindering longevity of recording or stimulation functions of brain implants [93]. Neural tissue has a soft consistency with an elastic modulus in the range of 0.4 – 15 kPa, while non-compliant brain interfaces have elastic modulus in the MPa or GPa range [52], [57]. For instance silicon has elastic (or Young's) modulus approx. 172 GPa, different in different directions in the material relative to the crystal orientation [94]. This huge mismatch between the elastic properties of biological environment and artificial implants creates permanent mechanical stress in the surrounding tissue, therefore tissue scaring and motion-related damage (eg. delamination of encapsulation materials, degradation of the insulation layer etc.) [95]. Replacing these conventional substrates with more adaptive or responsive materials can significantly reduce strains and the inherent micromotion induced stresses [53], [96], [97]. Hydrogels as coating materials provide the possibility to reduce elastic modulus of stiff (eg. silicon) microprobes by diminishing the mechanical difference between neural tissue and the proposed devices [96]. There are natural (eg. protein like collagen, fibrin or disaccharide or polysaccharide like maltose, saccharose, alginate, chitosan etc.) and synthetic (eg. organic polymers like polyglycolic acid (PGA), polylactic acid (PLA), poly(lactic-co-glycolic acid) (PLGA), polyethylene glycol (PEG), polyvinyl alcohol (PVA)) variant of hydrogels [98]–[102]. It is feasible to add conductive polymers (eg. PEDOT:PSS, PPy) to the hydrogel matrix, resulted in a coating with advantageous electrical properties as lower impedance values and better charge transfer capabilities [103]–[105]. The reduction of elastic moduli (from approx. 200 GPa to few tens of GPa) is not as high as it should be to approximate brain parenchyma in the kPa range. Nevertheless, other factors than Young's modulus will reduce mechanical stresses at the microprobe-neural tissue interfaces, for instance cellular interaction to the artificial surface. Hydrogels provide better adhesion for proteins of neural system than stiff materials, which results in increased body acceptance [96]. The main drawback of this approach that hydrogels are prone to swelling. Due to swelling

neurons are getting farther away from recording sites. Because of the excessive water absorption and retention, there is an additional risk for the delamination of hydrogel coating [106].

Intense foreign body response around stiff intracortical implants could lead to loss of probe functionality during long term, chronic experiments. The hypothesis behind the application of softening polymer material is to take advantage of its Young's modulus, therefore we could attenuate strong neuroimmune reaction. Other approaches with flexible or ultrathin intracortical arrays is the application of insertion shuttle [119-125], temporarily presented and attached to probe material during implantation. Application of insertion support is sufficient to overcome insertion forces without the buckling of the needle-like probes, resulted in extended cross-sectional area that could be as harmful, considering neuroimmune response, as their stiffer or thicker counterparts. Besides of this, bioresorbable or biodegradable polymers are popular insertion shuttle materials and although they are nontoxic, biocompatible materials, experimental subjects express inherent immunity to their decomposition products [130]. In our strategy, probe thickness of 60 μm and the initial Young's modulus (2 GPa) were proved to be suitable stiff enough to tolerate insertion forces without buckling the only limitation was the 10 minutes time window, within which time period the implantation had to be done to avoid buckling because of probe softening to 300 MPa. Do *et al.* declared that the water uptake by volume of thiol-ene/acrylate – based samples, did not exceed 1.11 % [151], while the swelling rate of hydrogels varies on an extensive scale but usually exceed 5 – 10 % [152]. More detailed analyses of *in vivo* recordings will be given in *Chapter 3*.

Several polymers eg. polyimide [107]–[111], poly(para-xylylene) or Parylene [112]–[116], SU-8 [117], [118], Liquid Crystal Polymer [119] have been utilized as flexible structural materials for the fabrication of intracortical neural probes. Based on finite-element modeling Subbaroyan *et al.* indicated that a soft material with 6 MPa of elastic modulus significantly reduce the tangential mechanical stress between neuroimplants and the surrounding tissue, and could be a better candidate for chronic experiment [120]. However the above mentioned polymer materials have elastic modulus in the GPa range (eg. $E_{Polyimide}$ = 2 - 8.5 GPa, $E_{Parylene}$ = 2 - 4 GPa etc.). Moreover the application of soft and flexible material as electrode substrate presents a new challenge for insertion and decent prediction of recording sites' depth in the brain tissue. A reasonable approach to overcome this issue is the integration of temporal or permanent electrode support. Microprobes are implantable without insertion aid if the force required for the penetration is lower than the compression force the electrode can tolerate without buckling, breaking etc. Temporarily the probes can be stiffen with biodegradable (or bioresorbable) polymer coatings [121], [122].

Polymers (eg. PLGA, PEG [123], gelatin [124], maltose [125], fishbone [126] or gutter-shaped silk [127] etc.) act as insertion aid during implantation procedure by providing enough stiffness to overcome the buckling force. After the probe is implanted, the bioresorbable polymer starts to degrade at physiological environment. Hydrolytic degradation of bioresorbable polymers result in the formation of nontoxic species that are gradually removed by metabolic processes [128]. On the other hand, application of bioresorbable polymers are still questionable because of the following reasons. The first one is the small time window for probe placement. Their degradation rate scales from seconds (eg. maltose, silk) to months (eg. PLGA, silk) and it should be slow enough to maintain its stiffness during insertion procedure but fast enough to avoid chronic immune response. Silk is a common example as its degradation rate is tunable and depends on the β – sheet content as a result of different post-treatments after synthesis [53], [129]. Its rate is tunable and influenced by different parameters, eg. molecular weight etc. The second one is the cytotoxicity and long-term effect of the by-products that are still debated but it is commonly accepted that the decomposition products of natural polymers promote less inflammatory than synthesized polymers [128]. The third one is the inherent immunity of the experimental subjects to bioresorbable polymers and their decomposition products [130]. The fourth one is the extended mechanical footprint caused by the polymer coatings because of the increased cross-sectional area. Because of their low thermal stability, they are not compatible with commercial sterilization processes, therefore their application in clinical trials is impossible.

Temporal solution could be the application of removable aids, in order to ease probe insertion. These are rigid, removable insertion stiffeners or backbones, temporarily attached to the flexible microprobes by using bioresorbable adhesives [131], [132]. The rigid part is removed after insertion, leaving the flexible structures behind [133]. Fast degrading glues (eg. PEG) or electrostatic fixing [134] need to be integrated as temporal adhesive agent that dissolve or cease quickly with the addition of water. Disadvantage of these structures is the increased cross-section during implantation and the main advantage arises from the application of soft materials disappears when rigid part is involved in the surgical procedure. Silicon or other stiff materials can serve as permanent microprobe support for thin and/or polymer-based flexible microprobes. In this strategy, polymers are integrated vertically with rigid stiffeners, attached to the flexible probes during the whole lifetime of the devices. Reasonable approaches have been used by Lee *et al.* and Kim *et al.* to allow enhanced insertion in the brain tissue while maintaining proper flexibility. Lee *et al.* [135] attached SOI (silicon-on-insulator) to the desired regions of the polyimide probe shaft, while Kim *et al.* [136] locally inserted flexible region from Parylene C to the solid silicon backbone. The main

drawbacks of this technique are the extended cross-section and the impaired mechanical advantage gained when soft materials were selected for structural component.

Recently, several newly-engineered substrate materials have been proposed as mechanically adaptive components for soft neuroprostheses. These polymeric materials undergo chemical or temperature-based activation resulting in a lower Young's modulus after placed in the living tissue. They maintain a Young's modulus of several GPa and provide easy handling before and during implantation [137]–[140]. Cellulose nanofibers embedded in a PVA-matrix showed remarkable changes in elastic properties between dry (4-5 GPa) and wet state (12 MPa) [141], [142]. Thermoset shape memory polymers (SMP) that can be tuned to undergo glass transition upon implantation are presently being explored. A thermally reactive copolymer made of methyl acrylate (MA) and isobornyl-acrylate (IBoA) cross-linked with PEG diacrylate was reported as neural probe substrate capable of softening from a Young's modulus of 700 MPa to 300 kPa [143]. Thiol-click chemistries have been proposed with the advantage of a widely tunable network structure and response to physiological conditions (change in temperature and fluid uptake) [144]. In particular, thiol-ene/acrylate substrate compositions have been shown to soften from over 1 GPa to 18 MPa with less than 3% fluid uptake upon exposure to 37 °C PBS; and cortical activity recording in rat subjects was demonstrated with probes built on such substrate [145]. Later, intracortical probes of thiol-ene/acrylate substrate that soften to a predicted 50 MPa were demonstrated to have neural recording capability over two months *in vivo* [146].

Cytotoxicity tests using NCTC fibroblasts and primary cortical neurons, and neurotoxicity tests using Microelectrode Array (MEA) -based functional assays and *in vitro* glial scarring assays were presented in previous works by the Voit Lab [87], [146]–[148]. Biocompatibility of the thiol-ene and thiol-ene/acrylate softening polymer materials were proven acceptable for neural experiments, *in vivo* neuronal loss and astrocyte activation were turned out comparable to that earlier reported for silicon probes [87], [147].

Mechanically adaptive substrates (eg, thiol-ene/acrylate compositions) that undergo chemical or temperature-based activation resulting in a lower elasticity after placing them in the living tissue, can maintain a Young's modulus of several GPa and provide easy handling before and during implantation. Take advantage of their soft consistency in physiological conditions, micromotion induce stresses, therefore the chronic neuroinflammatory response can be reduced [57], [96], [97], [149]. Such reduction of strains around microprobes lowers the risk of device failure and enables long lifetime.

2.1.1 Synthesis and DMA characterization of thiol-ene/acrylate softening polymer

Neural microprobes were fabricated using thiol-ene/acrylate polymer composition described earlier by the Voit group [144]–[146]. Synthesis of the softening polymer material and Dynamic Mechanical Analyses (DMA) were conducted by our collaborator (Advanced Polymer Research Laboratory, University of Texas at Dallas) in this project. The monomer solution consisted of a bi-functional acrylate, Tricyclodecane dimethanol diacrylate (TCMDA) and a stoichiometric ratio of tri-functional alkene, 1,3,5-triallyl-1,3,5-triazine-2,4,6(1H,3H,5H)-trione (TATATO) and a tri-functional thiol Tris[2-mercaptopropionyloxy)ethyl]isocyanurate (TMICN), additionally dimethoxy-2-phenylacetophenone (DMPA) was added as photoinitiator. The monomer solution was spin-coated on silicon wafers, and UV polymerized with a short (30 seconds) illumination at 254 nm, followed by a long (60 minutes) illumination at 365 nm, then the layers were post-cured in a vacuum oven at 120 °C for 24 hours. With this polymerization process, cross-linking is maximized, resulted in 300 MPa elastic modulus (storage modulus) upon implantation, an order of magnitude higher than the reported value (23 MPa) by Ware *et al.* (2013) [145].

DMA analyses revealed that there is a 22.5 °C difference in glass transition temperature between dry and wet conditions (**Figure 8. (a)**). Softening polymer samples were immersed in PBS solution at 24 °C, then the temperature was ramped up to 37 °C. Simulated physiological temperature was reached in approximately 1300 seconds later, while the elastic modulus stabilized at 300 MPa approximately 500 seconds later (**Figure 8. (b)**). For a more detailed synthesis and DMA parameters, refer to Zátonyi *et al.* (2019) [150].

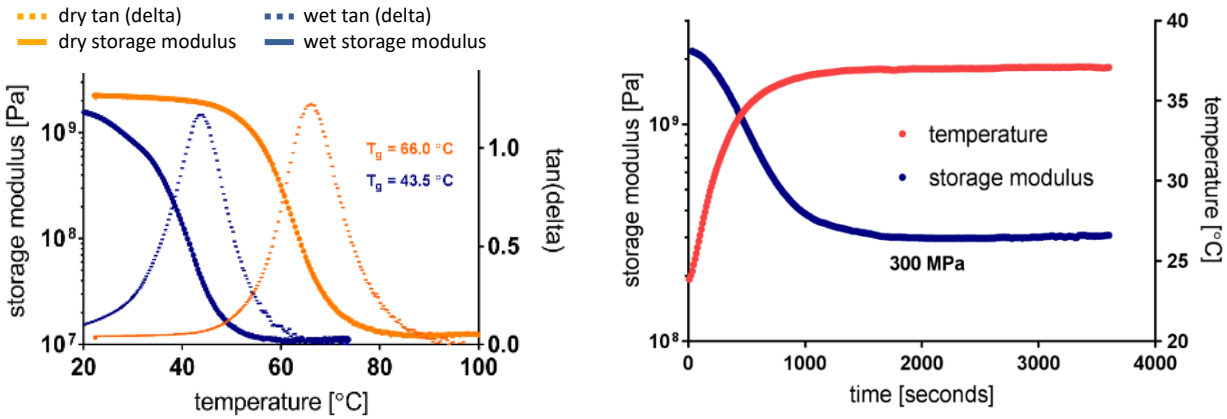

Figure 8. (a) Representative DMA curves of thin film polymer samples show the difference in glass transition temperature between dry and wet conditions (If tan(delta) > 1 (G" > G') (liquid or 'sol'), if tan(delta) = 1 (G" = G') (viscoelastic or 'gel point'), if tan(delta) < 1 (G" < G') (solid or 'gel')). (b) Softening of a polymer sample upon immersion into 24 °C in PBS solution and heated to 37 °C.

Based on the publications from several research groups, the relationship between the mechanical compliance of probe materials alone and the foreign body response that follows the traumatic injury is not well understood, and needs further investigations. My work to create a valuable tool to support this effort is described in the following chapters.

2.1.2 Cytotoxicity

In previous works, the Voit Lab has tested the biocompatibility of SMP material *in vitro* and *in vivo* using NCTC fibroblasts, primary cortical neurons and MEA-based functional assays [87], [146]–[148]. Based on cytotoxicity assays neither single channel or network activity was found to be significantly altered (tolerance compared to stainless steel microprobes). *In vivo* neuronal loss and astrocyte activation were found comparable to that previously stated for silicon probes.

2.2 Methods

Fabrication of the softening polymer microprobes in clean room environment relies on a joint work of The University of Texas at Dallas and that of the Hungarian Academy of Sciences. Our brain probes comprised of a sandwich structure of thiol-ene/acrylate, Parylene C polymers and titanium/gold conductive layers. Spin-coating was applied to precisely control the thickness of softening polymer (SMP) layers.

Fabrication and packaging processes, electrochemical testing of insulation properties of the proposed material composition and the invented packaging technology will be presented. Additionally, *in vivo* performance of the intracortical probes will be demonstrated.

2.2.1 Design, microfabrication and elaboration of packaging

Length, width and thickness of the softening microprobe are 5 mm, 200 μm and 60 μm, respectively. The device has eight recording sites with a diameter of 15 μm and interelectrode spacing of 188 μm. The first site was designed to be 150 μm far from the probe tip. The fabrication scheme is shown on **Figure 9. (b)**. The solution of softening polymer was spin-coated at the top of a silicon handle wafer to form a 53 μm thick film and cured as described earlier (step 1). This is followed by the deposition of a 500 nm thick Parylene C layer (step 2). Thereafter, the lift-off pattern was formed for gold metal traces (step 3), using plasma enhanced chemical vapor deposited (PECVD) silicon nitride and S1813 photoresist. Silicon nitride is removed in fluorine plasma (RIE), and the gold layer was evaporated. Lift-off process resulted in 400 nm

thick gold traces to form recording sites, wiring, and bonding pads of the probes. Another 500 nm thick Parylene C film was deposited (step 4) to provide structural stability as both the softening polymer and the gold have better adhesion to Parylene C. One micron thick Parylene C was etched (step 5), using oxygen plasma RIE to maintain its coverage in proximity to the gold traces. A second, encapsulation layer of 7 μm thick softening polymer was spin-coated at the top of this structure (step 6). To open the softening polymer above the recording sites and bonding pads, PECVD silicon nitride was deposited, patterned and used as a hard mask for oxygen plasma etching (step 7). On top of this structure, a new masking layer of PECVD silicon nitride was deposited to define the contour of the probes (step 8). The structures were released from the wafer by soaking in distilled water at 37 °C for 4-5 days (step 9).

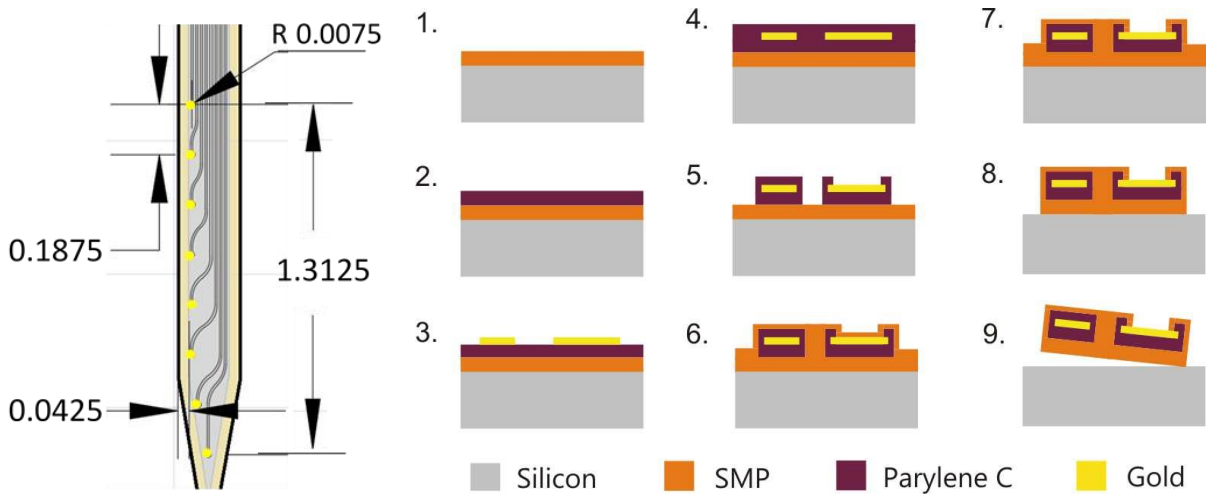

Figure 9. (a) Design parameters of the softening polymer probe (numbers are scaled in mm) (b) Schematic process flow of probe fabrication

Test of packaging

To make a firm connection between the bonding pads of the electrode and the external Omnetics (A79040-001, Omnetics Connector Corp., MI, USA) connector, a custom process flow was established. The evolution of packaging, until I get to the final solution, can be divided in two main stages. In the first stage, connector pins were pressed into a drop of two-component silver epoxy glue (CW2400, Chemtronics, US), then they were preserved by two-component epoxy paste (Araldite 1401, Huntsman Advanced Materials GmbH, Switzerland). The probes were submerged in distilled water up to the Omnetics connector, and sinusoidal voltage (AC) with amplitude of 25 mV and scanning frequencies from 1 Hz – 10 kHz was applied to obtain Bode plots and to evaluate the stability of the packaging. Bode plots were recorded on day 1,

day 2, day 3, day 7, day 9, day 10, day 15 at room temperature (24.5 °C), then on day 16 and day 18 at elevated temperature (50 °C) in order to accelerate the stability experiment. Based on Bode plot analyses, this approach resulted in shortcuts between bonding pads (**Figure 10 (a - d)**). This observation was attributed to fluid uptake due to the swelling of softening polymer material that resulted in leakage current between bonding pads. In the second stage after carefully reconsidered the original workflow, the process started with the same step, a drop of CW2400 conductive adhesive was dispensed onto the surface of the gold bonding pads such that the conductive drops are not in contact with the polymer. After that, the adhesive was left to dry at room temperature for 24 hours. Curing procedure after each packaging step was performed at room temperature that is below the glass transition temperature of softening polymer. In order to isolate the gold pads from the water-permeable softening polymer substrate, Elastosil® RT 607 (Wacker Chemie AG, Germany), a two-component silicone rubber was applied at the edges where the substrate covered the bonding pads. After another 24 hours of drying at room temperature, a second drop of CW2400 was allocated right above the first drop, surrounding the connector pins that were fixed in the silver epoxy glue. This whole structure around the connector pins was protected by Araldite 1401 adhesive. Detailed optical microscopic representation of the main steps can be seen in **Figure 10. (e & f)**. This strategy contributed to firm connection based on the soaking experiments (described in the following chapter). Final composition of packaging and ready – to – use probe are shown in **Figure 10**. **(g)**.

2.2.2 Electrochemical characterization

All electrochemical measurements (Electrochemical Impedance Spectroscopy (EIS) or Cyclic Voltammetry (CV)) were performed in a three compartment electrochemical cell using a Gamry Reference 600 (Gamry Instruments, *Warminster, PA, US*) potentiostat. A leakless miniature Ag/AgCl (3.4 mol/L KCl) electrode (ET072-1, eDAQ Pty Ltd., *Australia*) and a platinum wire (for EIS, CV) or platinum sheet (for deposition) with a relatively high surface area were used as reference and counter electrode, respectively. Fabricated recording sites were connected as working electrodes. All potential values in this thesis are given versus the Ag/AgCl reference electrode. EIS measurements were carried out by applying sinusoidal, 25 mV RMS across a range of frequencies tested from 1 Hz to 10 kHz in phosphate buffered saline (PBS) solution (P4417, tablet diluted in 200 mL distilled water yielding 0.01 M phosphate buffer, 0.0027 M potassium chloride and 0.137 M sodium chloride, pH 7.4, at 25 °C, Merck KGaA, Germany). All measurements were conducted in a Faraday-cage, in a cleanroom environment and in all cases at room temperature except for the accelerated aging tests. Gamry Framework 7.8 and Gamry Echem Analyst 7.8 software were used for experimental control, data acquisition and data evaluation. Recorded data points

of EIS spectra are presented on Bode Plots, in which the impedance magnitude and phase angle are plotted against frequency. The magnitude and phase angle are given by **Equation 13.** and **Equation 14.**, respectively.

$$|Z| = \sqrt{Z_{Re}^2 + Z_{Im}^2} \tag{13}$$

$$\theta = tan^{-1}\left(\frac{Z_{Im}}{Z_{Re}}\right) \tag{14}$$

Due to the large range of IZI and frequency values are plotted on log scales for easier examination of small values. The complex-impedance plane representation, or Nyquist Plot, consists of plotting the imaginary impedance component (Z″) against the real impedance component (Z′) at each excitation frequency. Although this type of plot is valuable for identifying directly and easily the ohmic resistance and charge transfer resistance, double layer capacitance can be calculated only with proper frequency information that is intrinsically lost.

In order to test the insulation stability of the proposed thiol-ene/acrylate-based devices with Parylene C inner encapsulation and adhesion promoter layer, electrodes were permanently soaked in 0.01 M PBS solution for 11 days at 37 °C (physiological temperature). Bode plots were recorded every day during the experimental period in the same PBS solution. These pre-liminary results are crucial not only for the determination of insulation performance of polymers, but also for the forthcoming experiments related to impedance improvement through electrochemical deposition of platinum black (more detailed description about the deposition will be seen in Chapter 3.).

2.2.3 In vivo experiment

In vivo validation of softening polymer – based microprobes was performed in the Institute of Cognitive Neuroscience and Psychology of the Research Centre for Natural Sciences, Hungarian Academy of Sciences, in the rat brain. Only acute electrophysiological data is presented in our study.

Wistar rats (270 – 400 gr, a total of 3) were anesthetized with ketamine-xylazine solution and mounted in a stereotactic frame. Craniotomy was performed -2.0 mm - -6.0 mm anteroposterior (AP), 2.0 mm - 6.0 mm mediolateral (ML) in reference to the Bregma. The implantation of the multielectrode probes was targeted at the stereotaxic location of -4 mm AP, 4 mm ML, perpendicularly to the brain surface. Afterwards the dura mater was incised to achieve a smooth implantation by avoiding possible buckling of

the probe. Implantation was performed above the somatosensory cortex and depth coordinates were gradually increased until the hippocampus at maximum depth was reached. Electrophysiological activity was recorded at different depths. At room temperature the polymer probe has proven to be rigid enough and suitable for inserting it into the neural tissue, without using any implantation supporting device or coating. Stainless steel needle was used as reference electrode and was implanted beneath the skin. The animals were transferred into a closed Faraday cage, then electrophysiological signals were recorded using Intan RDH-2000 amplifier system (Intan Technologies LLC., Los Angeles, CA, USA) connected to a computer via USB 2.0, sampling with a frequency of 20 kHz.

Matlab 2014b (Mathworks Inc., Natick, MA, USA) software was used for off – line data processing and filtering. Raw data was band – pass filtered between 500 and 5000 Hz, suing second – order Infinite Impulse Response (IIR) filter and 50 μV was defined as threshold amplitude for single unit activities. Principal Component Analysis (PCA) was selected for spike sorting and helped to decide how many neurons were present and assigned each spike uniquely to one neuron or to noise, if unsortable based on 50 μV threshold. The clusters (group of spikes assigned to one neuron) were manually accepted or rejected based on spike waveforms, and they were justified by making autocorrelograms. Noise is defined as the distance between the waveforms of two spikes. Single unit signal-to-noise amplitude ratio (SU SNAR) for single unit clusters was calculated as:

$$SU\ SNAR_i = \frac{PP_i}{2\sigma_n} \tag{15}$$

$PP_i = mean\ peak - to - peak\ amplitude\ of\ the\ spikes\ in\ cluster\ i$

$i = index\ of\ the\ cluster$

$n = index\ of\ recording\ channel\ containing\ the\ spike\ waveform\ of\ cluster\ i$

$\sigma_n = standard\ deviation\ of\ the\ filtered\ signal\ of\ the\ n^{th}\ recording\ channel$

Edit 4.5 software of Neuroscan (Charlotte, NC, USA) was used for analyzing the recorded low-frequency potential signals. Calculating the power of low gamma (30 - 50 Hz) band of each channel, helps to interpret the location of the corresponding recording site within the hippocampus [177].

2.3 Results and discussion

2.3.1 Evolution of packaging

The probes were immersed in distilled water up to the Omnetics connector and EIS was used to monitor the stability of the packaging. EIS spectrums were recorded between the period of day 1 – day 15 at room temperature then from day 16 – day 18 the temperature was raised up to 50 °C to accelerate the soaking experiment. Based on Bode plot analyses, the first approach, where the application of Elastosil for separation purposes was omitted, resulted in shortcuts between the adjacent bonding pads. The impedance spectrums revealed the effect of absorbed humidity clearly shown in **Figure 10. (a & b)** for a representative recording site. Magnitude of impedance decreased while phase angle increased similarly at each frequencies. It can be concluded from phase angle values that CPE (Constant Phase Element) started to act more like a resistor and not like a pure capacitor, where $\alpha = 1$ and $\phi = -90°$. After the 18th day of stability experiment, the characteristics of impedance and phase curves were changed significantly, and this phenomenon was more dominant at higher frequencies, as electrochemical behaviour is dominated by capacitance at frequencies above 10^3 Hz. Impedance magnitude at 1 kHz was plotted against soaking days and recording sites in **Figure 10. (c)** on a 2D color map, where the "coldest" color (dark blue) represents the highest (initial, in this case) impedance values, while the "warmest" color (dark red) represents the lowest Z value, which is the direct sign of shortcut. Based on the 2D color map, shortcuts were started to evolve from the two terminal of bonding pads until the 18th day when all bonding pads formed one conducting element. Decrease in impedance related to the immersion was proved with CPE analyses. The coefficient of CPE (Y) or the real part of the capacitance extracted as a function of soaking time are shown in **Figure 10. (d)** for a representative channel. Initial increase in the value of Y can be observed, which can be attributed to immediate swelling of softening polymer. This was followed by slow increase in Y during the period of more than 14 days. The moderate variations can be related to changes in the composition of PBS solution, which was refilled frequently due to unavoidable evaporation. Strong increase in Y was observed for 18 days (at 50 °C) because of the evolved and uniform shortcuts between bonding pads. These results show that this type of packaging did not provide sufficiently stable connection between conductive traces of the microprobe and connector pins. The main steps of the second packaging strategy is shown in **Figure 10. (e & f)**. The advantage of this packaging technique is that it provides less chance for leakage by avoiding shortcuts formed by fluid channel between bonding pads. **Figure 10. (g)** shows a photo of a ready-to-use neural probe for hippocampus recording. With the help of this unique and robust packaging technology a leak-free connection was established.

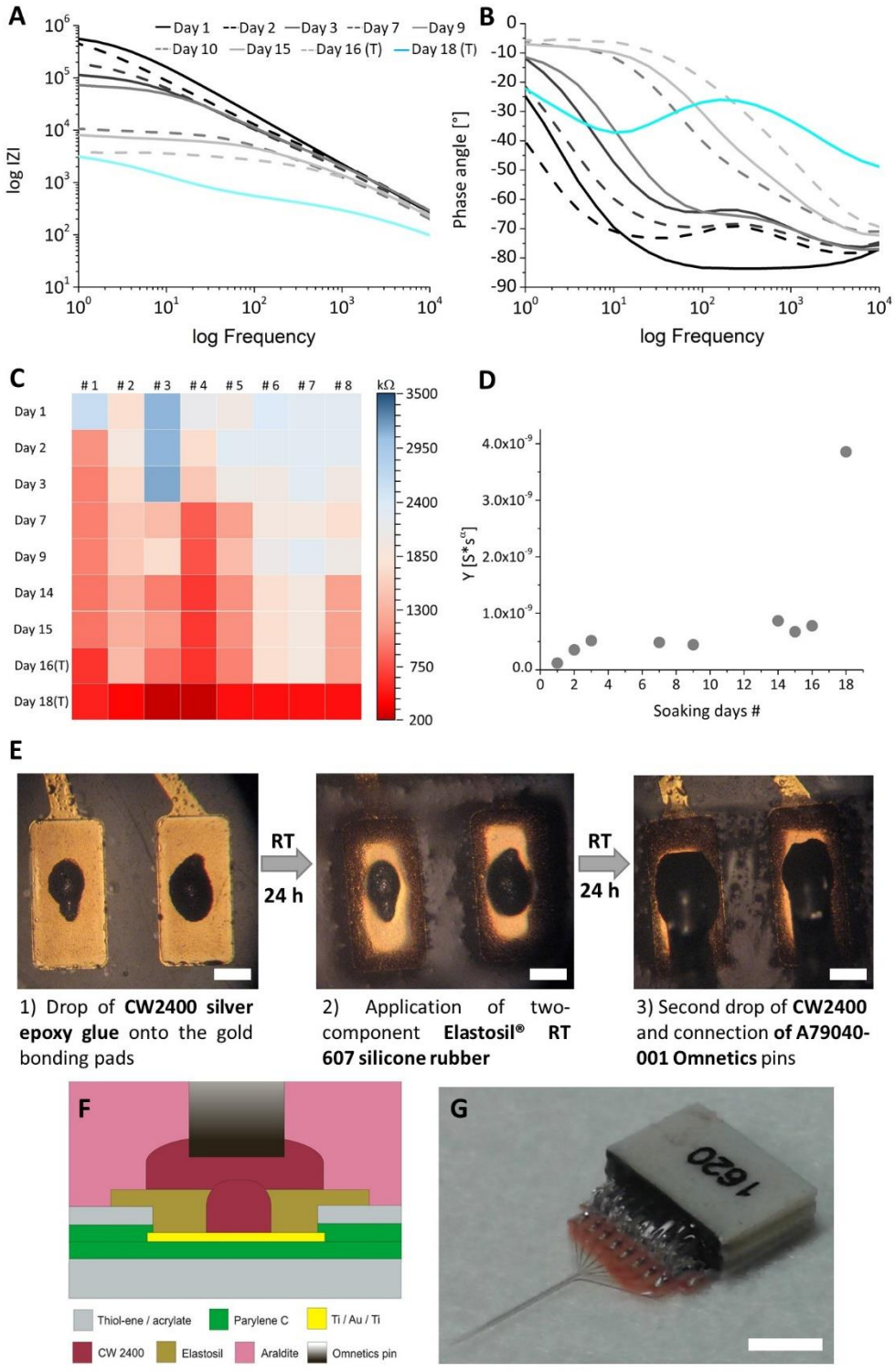

Figure 10. (a & b) Bode plots of a selected channel for the whole soaking period of packaging stability assessment. (c) Variations in impedance at 1 kHz for each channel of a selected microprobe versus soaking time on a 2D color map, where the "coldest" color (dark blue) represents the highest Z value, while the "warmest" color (dark red) represents the lowest Z values. (d) Evolution of coefficient of CPE for a selected channel during experimental period. (e) Optical microscopic images representing main steps resulted in leak-free packaging. Scale bars are 250 μm. (f) Schematic cross-sectional view of the layer structure used to connect bonding pads to pins of Omnetics connectors. Figure is not to scale. (g) Ready-to-use neural probe. Scale bar is 3 mm.

Electrochemical stability assessment of the second packaging method will be described in details in the next subsection (*2.3.2 Electrochemical performance*).

2.3.2 Electrochemical performance

Thiol-ene/acrylate polymer-based intracortical probes were soaked at 37°C in 0.01 M PBS solution for 11 days, and EIS was recorded every day at room temperature in the same solution. Bode plots representing the impedance magnitude and phase angles of the recording sites were acquired and analyzed with Gamry Echem Analyst software (Gamry Instruments, Warminster, PA, US). Besides the typical measures at 1 kHz, we provide a more detailed analysis of both magnitude and phase plot throughout a broad frequency interval (10 kHz, 1 kHz, 100 Hz, 10 Hz and 1 Hz). EIS showed a slight decrease in the first 5-8 days of soaking in impedance magnitude between 1 Hz to 10 kHz with greater dispersion at lower frequencies (from 0.32 ± 0.09 MΩ to 0.26 ± 0.07 MΩ at 10 kHz, from 2.61 ± 0.71 MΩ to 1.36 ± 0.40 MΩ at 1 kHz, from 19.45 ± 6.10 MΩ to 5.04 ± 2.29 MΩ at 100 Hz, from 112.07 ± 43.15 MΩ to 14.74 ± 5.68 MΩ at 10 Hz, from 248.07 ± 135.98 MΩ to 40.05 ± 4.68 MΩ at 1 Hz averaged for 16 recording sites on two electrode arrays) for arrays exposed to PBS at 37 °C (**Figure 11. (a & c)**). Summary of impedance at five different frequencies can be seen in **Table 2**. After 8 days of soaking, the initial impedance values stabilized and remained stable during 11 days of stability test. The phase angle increased at all frequencies except for 1 Hz, where the greatest standard deviation (lowest precision) was observed. The greatest change in the phase angle occurred at frequencies between 100 Hz and 1 kHz (**Figure 11. (b)**). The Nyquist plots are fitted according to the Randles model, and the as-fitted Nyquist plots on the 1st, 5th and the 9th day are shown in **Figure 11. (d).**

Table 2. *Magnitude of impedance at five different frequencies (1 Hz, 10 Hz, 100 Hz, 1 kHz, 10 kHz) at the first (Day 1) and last (Day 11) days of packaging evaluation test*

Z (MΩ),	1 Hz		10 Hz		100 Hz		1 kHz		10 kHz	
(n=8)	Mean	S.D.	Mean	S.D.	Mean	S.D.	Mean	S.D.	Mean	S.D.
Day 1	248.07	135.98	112.07	43.15	19.45	6.10	2.61	0.71	0.32	0.09
Day 11	40.05	4.68	14.74	5.68	5.04	2.29	1.36	0.40	0.26	0.07

Results of EIS during 11 days of soaking period, revealed a uniform decrease in impedance and an almost uniform increase in phase angle that are likely due to diffusion of water and possible penetration of moisture through the polymer layers, resulting in a switch from capacitive to resistive state. Nyquist plots are indicating that eyuivalent circuit parameters of R_{CT} and C_{CPE} were changed significantly from Day 1 to Day 11. R_{CT} decreased while C_{CPE} increased and this phenomenon can be attributed to the increased contact area due to swelling resulted in more achievable active sites at the electrode – electrolyte interface.

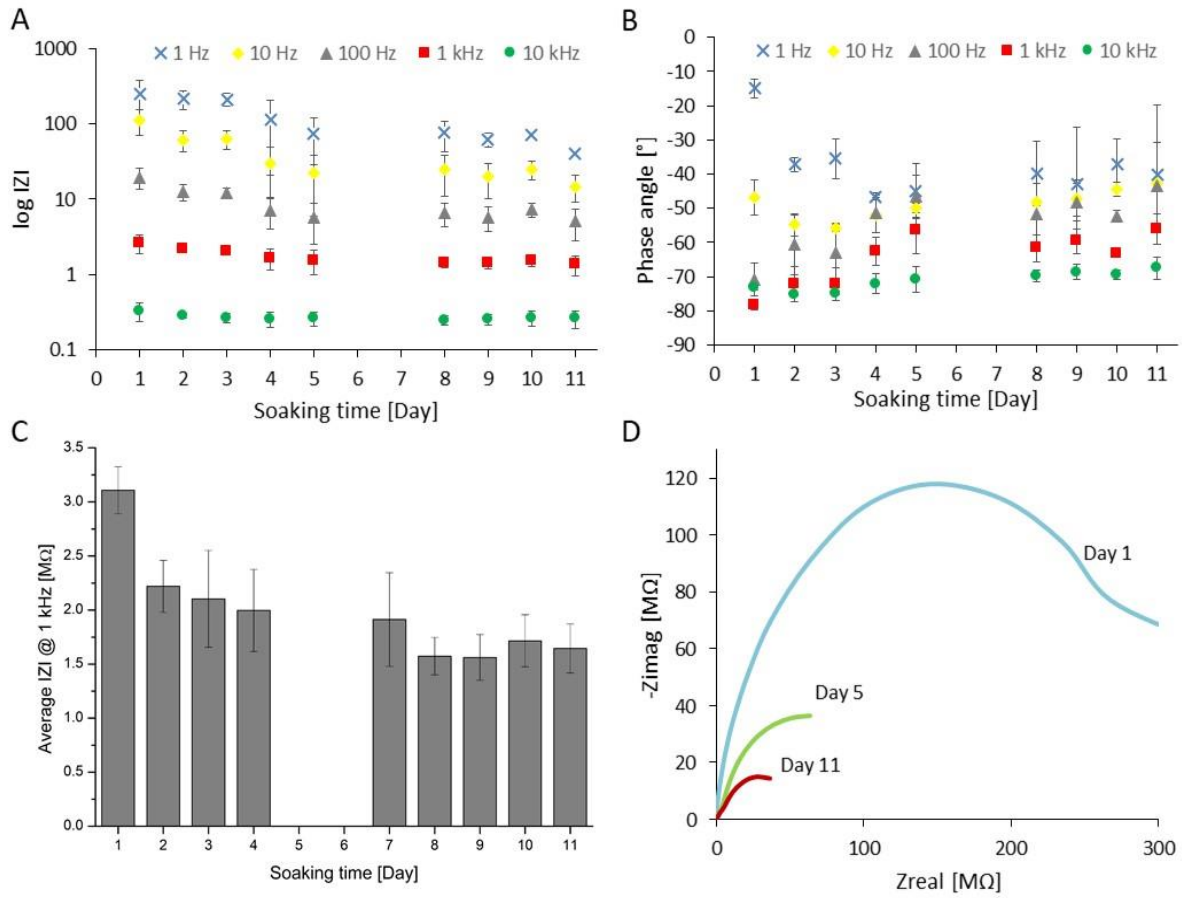

Figure 11. (a & b) Average 10 kHz (green circle), 1 kHz (red square), 100 Hz (grey triangle), 10 Hz (yellow rhombus) and 1 Hz (blue cross) impedances and phase angles recorded from two unique microprobes with 8-8 recording sites on each. Data present mean values ± standard deviation (n=16). (c) Impedance magnitude measured in the soaking test at 1 kHz is plotted against time. (d) Nyquist plot is presented to show complex impedance of a representative recording site at the 1st (blue line), 5th (green), 11th (red) day of the soaking experiment.

2.3.3. In vivo of probe's functionality

The 60 μm thick softening polymer based neural probes proved to be suitable for precise insertion into the neural tissue up to 4.5 mm in depth without buckling or bending and without the aid of an insertion shuttle. Probes with platinum black coatings, were capable of recording neural activity and detecting spikes from the hippocampus. More detailed description about porous platinum deposition and evaluation will be given in the next chapters (*Chapter 3.2.2* and *Chapter 3.3.1 – 3.3.4*). A representative sample of the recorded LFP signals is shown in **Figure 12. (a)**, while in **Figure 12. (b)**, associated power in the gamma band per channel is illustrated. This power correlates with the proximity of each electrode with the hippocampus, in this example, left part shows channel #2 and #3 that were located in this region. As inserted deeper in the brain tissue, channel #5 shows the highest amplitude gamma waves, as expected regarding vertical spacing of recording sites.

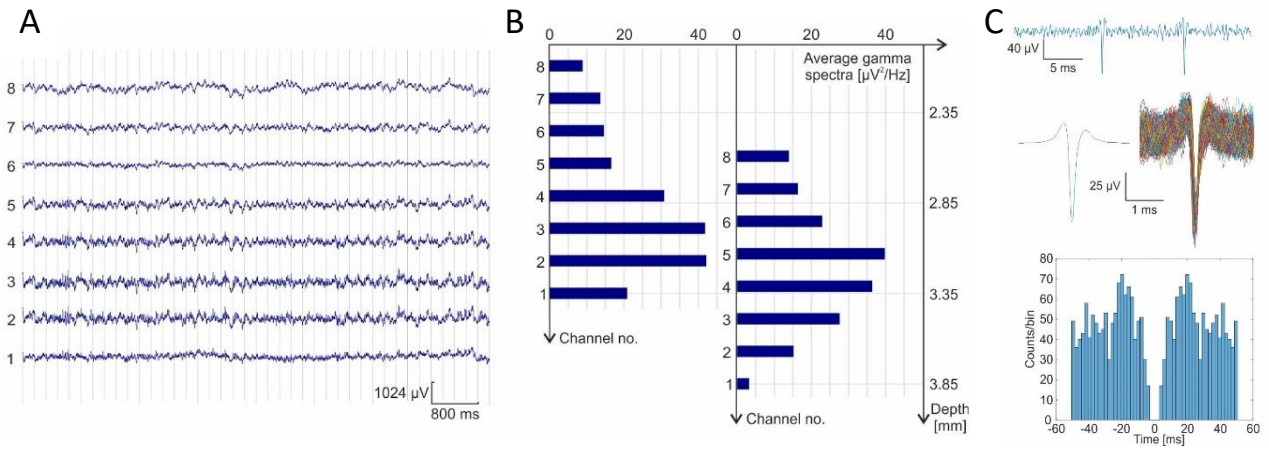

Figure 12. (a) Representative sample of recorded LFP signals. (b) Gamma power of channels according to their depth in the brain. (c) Representative, 500 – 5000 Hz band-pass filtered waveform (at the top), average of one clustered spike from each waveform (middle on the left), and all their occurences (middle on the right) and autocorrelogram (at the bottom).

The result of the spike sorting are presented in **Figure 12**. **(c)**. Matlab function applies the second-order section digital Infinite Impulse Response (IIR) bandpass filtering was used, between 500 – 5000 Hz. - 50 μV was defined as the detection threshold for action potentials. The autocorrelogram specifies the probability of encountering the same spike as a function of time after a given spike. Refractory periods are observable in the middle of the autocorrelograms and indicate correctly identified clusters. Average observed peak – to – peak amplitude was 84 μV with SNR of 6.24 in acute experiments.

Our study demonstrates that softening neural probes may be used to investigate deep layers of the rat brain, detection of spikes from the hippocampus was feasible, whereas the maximum number of units identified from the analysis was 4 per probe.

2.4 Conclusion and future concept

5 mm long (needle length), 200 μm wide (needle width) and 60 μm thick, single-shank, softening polymer-based intracortical probe was designed and fabricated using standard semiconductor manufacturing processes. Each probe has 8 recording sites with a site diameter of 15 μm, interelectrode spacing of 188 μm. Most of the published SMP brain probes comprised of a simple, three-layer structure (custom thiol-ene/acrylate thermoset polymer substrate and conductive material), except for one single study proposed a material configuration similar to ours [87]. Based on DMA analyses (**Figure 8.**) the softening polymer material changes its elastic modulus from 2 GPa to 300 MPa when exposed to physiological conditions (when $T > T_g$) in a 10 minute timescale.

New packaging technology was developed to avoid leakage between adjacent bonding pads due to swelling of softening polymer material. Electrochemical impedance spectroscopy revealed that our fabrication and packaging technology provides a stable softening neural interface with very small device footprint.

Higher water uptake (swelling) of polymer substrate could be unfavorable as this phenomenon leads to polymer expansion, therefore the probe could lose its functionality due to delamination or breakage of conductive traces. In order to test the electrochemical stability of ready-to-use devices, the probes were constantly soaked in PBS solution while their impedance characteristics were measured daily with EIS. After 8 days of soaking, the initial impedance values stabilized between 5 and 8 days, and the magnitude of impedance dropped by 47.9 % at 1 kHz possibly due to the swelling. Uniform decrease in impedance values and uniform increase in phase angle at each experimental frequencies (1 Hz – 10 kHz) imply that the conduction mechanism at electrode-electrolyte interfaces, not significantly but comparatively switched towards a more resistive manner. Achieved results indicated for future experiments that the probes had to be soaked before platinum deposition in order to overcome platinum black delamination as a consequence internal stresses due to polymer expansion. Our probes remained functional during the whole soaking period (11 days at room temperature) and because our design contains a Parylene C encapsulation layers within softening polymer layers, swelling did not deteriorate device performance and reliable recording could be achieved after an equilibrium of impedance magnitude have been attained.

Reaching the hippocampus, not only provides access to the center of memory and spatial navigation with shape-memory polymer based probes, but opens up new opportunities to conduct experiments in even deeper areas of high interests for the field of neurodegenerative research. In our study, the softening probes were easy to handle and all probes maintained their shape without fracturing or bending. Our experiments imply that smart implants made of mechanically adaptive polymers are promising candidates to replace rigid laminar microelectrodes used for monitoring and stimulation of the deep neural tissue.

Thesis statement related to this chapter

I designed and developed the microfabrication and packaging process flow of a 5 mm long thiol – ene / acrylate based neural probe. I elaborated a novel and reliable packaging scheme, which helped to minimize leakage currents during device operation in wet environment. Long term stability, functionality and reliability was investigated with electrochemical impedance spectroscopy and equivalent circuit analyses. These results revealed that the initial impedance of 15 μm diameter gold recording sites stabilized between 5 and 8 days. I contributed to the validation of device functionality under *in vivo* experimental conditions, where single unit activity was recorded from the rat hippocampus, achieving average peak – to – peak amplitude of 84 μV with 6.24 signal – to – noise ratio.

Scientific paper related to this thesis statement

A Zátonyi *et al.*, A softening laminar electrode for recording single unit activity from the rat hippocampus, ***Scientific Reports***, Vol. 9, 37237, **2019**

3 DURABILITY OF PLATINUM BLACK COATINGS ON NEURAL ELECTRODES

3.1 Introduction

In general, the dimensions of neural microsensors should be close to the neuronal structure (in the cortical region it is around 15-20 μm [15]) either to limit cellular damage or to monitor extracellular signals at high precision. The small geometric area of the recording sites, however, deteriorate the signal – to – noise ratio of the recordings caused by the inherently large impedance values. In view of recording electrodes designed to catch neuronal signals, the major internal noise source is the thermal noise, which is proportional to the square root of the real part of the electrode impedance [153], [154]. In order to reduce the magnitude of thermal noise, and consequently to achieve higher SNR, lower electrode impedance is desired in the frequency band of interest (1 Hz – 10 kHz) [155]. Recording of individual neurons (single-units), the geometric area of the recording sites should not exceed 2000-4000 μm^2 [15], however, detection of isolated spikes from the superficial cortical layer using ECoG devices is also possible with electrodes having far less geometric areas, e.g. 100 μm^2 [13]. The question is how can we improve SNR while reducing the size of the recording sites? Increasing the effective surface area of the sites is the optimal solution. To form high surface area conductive layers, electrochemical methods are widely used. Porous materials such as platinum black [29]–[31], [156]–[159] and conductive polymers [32], [160]–[162] with larger effective surface area and huge roughness factor are the most popular materials that have been developed to overcome this challenge. Conductive polymers are under intensive research regarding *in vivo* use, however, mechanical and electrical stability as well as compatibility with microfabrication techniques are still to be investigated [20], [163]–[171]. With the deposition of porous layers on top of the sputtered or evaporated layers, surface roughness will significantly increase, consequently the electrode impedance can be reduced to the desired level (IZI < 1 MΩ @ 1 kHz [172]).

My objective was to study the mechanical and electrical stability of platinized recording sites on flexible and soft neural interfaces, which has been barely addressed during *in vivo* experiments compared to the rigid implantable electrodes (e.g. tungsten or silicon) [29]. The surface morphology, impedance characteristics, *in vivo* recording capability and the stability of the electroplated coating after implantations were measured and evaluated in details.

3.2 Methods

During the related research projects, flexible, polyimide – based μECoG devices (in this *Chapter* the term of "μECoG" will be used) and soft, shape memory polymer (SMP) – based probes (in this *Chapter* the term of "microprobe" will be used) were applied as platforms to study the stability of platinum black on recording sites. Since the technology of the softening microprobe has been presented earlier in *Chapter 2.1* and *Chapter 2.2*, in this section only the fabrication process of the μECoG array will be described.

3.2.1 Design, microfabrication and packaging

μECoG arrays holding 16 recording sites were arranged as 4 tetrodes (four closely spaced recording sites, located at the apex of a rhombus). Since tetrodes provide a 4D "image" of signals, its technology is applied in single-unit recording to spatially localize the neuronal sources, therefore facilitate clustering of the electrophysiological data [173]–[176]. Diameter of the recording sites was 20 μm with different inter-electrode distances (center-to-center), like 25 μm and 100 μm. To avoid the influence of under-etching during the reactive ion etching process, photolithography masks were designed with hole diameters of 18 μm. Polyimide was selected as flexible, insulating substrate material of the μECoG devices. Flexible interconnection, made of polyimide and platinum as conductive traces with a length of 30 mm, was designed to joint recording sites to the connector pins and was fabricated concurrently with the sites and connection pins.

The fabrication technology of the μECoG is based on three mask, semiconductor cleanroom process. Schematic cross – sectional view of the step – by – step μECoG fabrication process is shown in **Figure 13**. Cross – sectional view is defined to contain one electrode and the contour of the μECoG.

First, a 4" silicon wafer was dipped into 1:20 HF (hydrofluoric acid (48%):distilled water) for 30 seconds to remove native oxide from the surface. 4 μm thick polyimide (PI2611, BPDA/PPD (3,3',4,4'-biphenyltetracarboxylic dianhydride / p-phenylenediamine) precursor and NMP (n-methyl-2-pyrrolidone) carrier solvent) was spin-coated at 4000 rpm for 30 seconds to form bottom insulating or substrate layer (step 1). Final curing of the layer was performed at 300 °C for 1 hour on a hotplate after a soft-bake process, where the temperature was ramped up at 5 °C/min from 130 °C. During the curing process, the polyamic acid precursor is converted into a fully aromatic, insoluble polymer and the carrier solvent is completely evaporated. Fully polymerized film shows the optimal electrical and mechanical properties of the polymer (based on the datasheet of PI2611). 300 nm aluminum sacrificial layer and

Microposit 1818 positive photoresist was used to form the lift-off pattern for platinum (step 2). The aluminum was selectively etched in a five-component solution, consisted of H_2O, CH_3COOH, H_2SO_4, H_3PO_4, and HNO_3 in a ratio of 70:20:30:32:20 (step 4). 15 nm TiO_x and 270 nm Pt was deposited in a DC sputtering equipment (step 5).

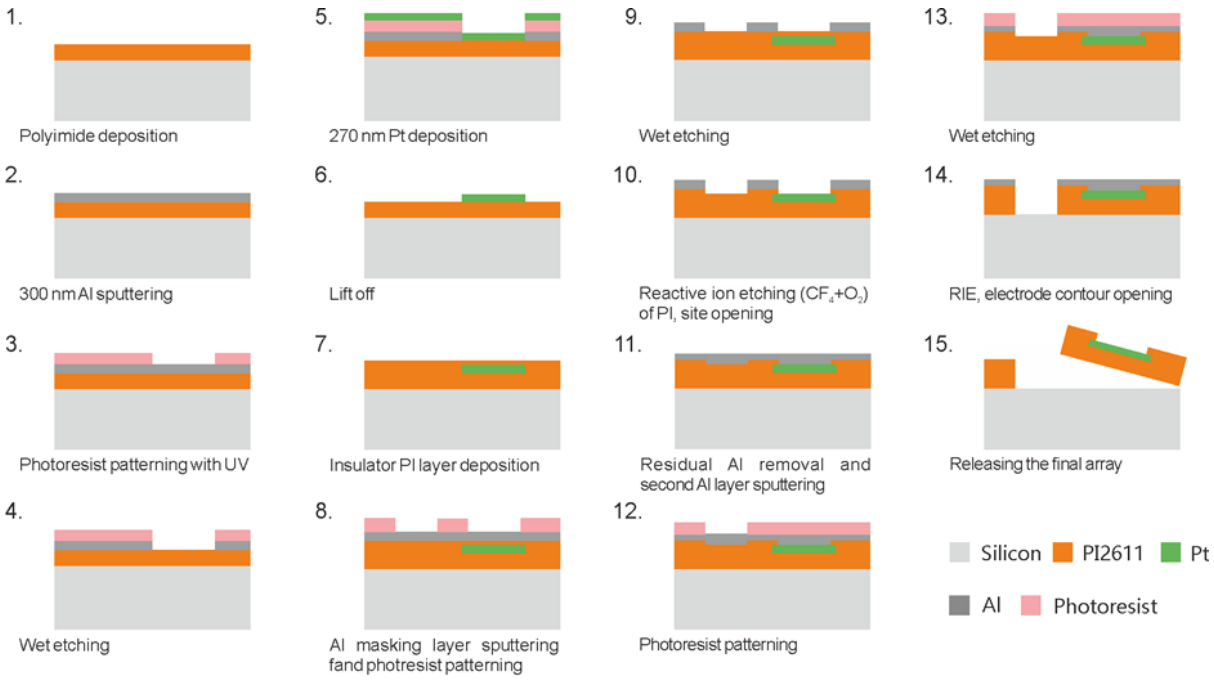

Figure 13. Schematic cross-sectional view of μECoG's microfabrication process.

Lift-off process was finished by soaking the wafers in acetone and aluminum etchant (step 6). 80 W oxygen plasma was applied for 30 sec to remove remaining organic contaminations and to promote adhesion of the second polyimide film. The upper passivation layer of 4 μm thick polyimide was spin-coated and cured as described above (step 7). 100 nm aluminum thin film as a hard mask for reactive ion etching was deposited and selectively opened above the recording sites, connector pins and the contour of the device (step 8-9). The exposed polyimide surfaces were removed in CF_4/O_2 plasma (gas ratio was 1:4, 200 W, 0.5 mbar, step 10). Due to the great variation of structural parameters (eg. diameter of recording sites and connector pins are 20 μm and 800 μm, respectively) a third mask was required to entirely remove polyimide above connector pins and to define the contour (step 11 – 14). After the final RIE step, the aluminum masking layer was removed completely in aluminum etchant (step 15), then the devices was released from the silicon wafer with a tweezer. Pads in the backbone of the electrode were

soldered on a 16-channel through-hole Preci-Dip electrical connector. The ready-to-use packaged μECoG device, schematic drawing with functional part arrangement, and optical microscopic view of smooth platinum and platinum black-coated tetrodes can be seen in **Figure 14.**

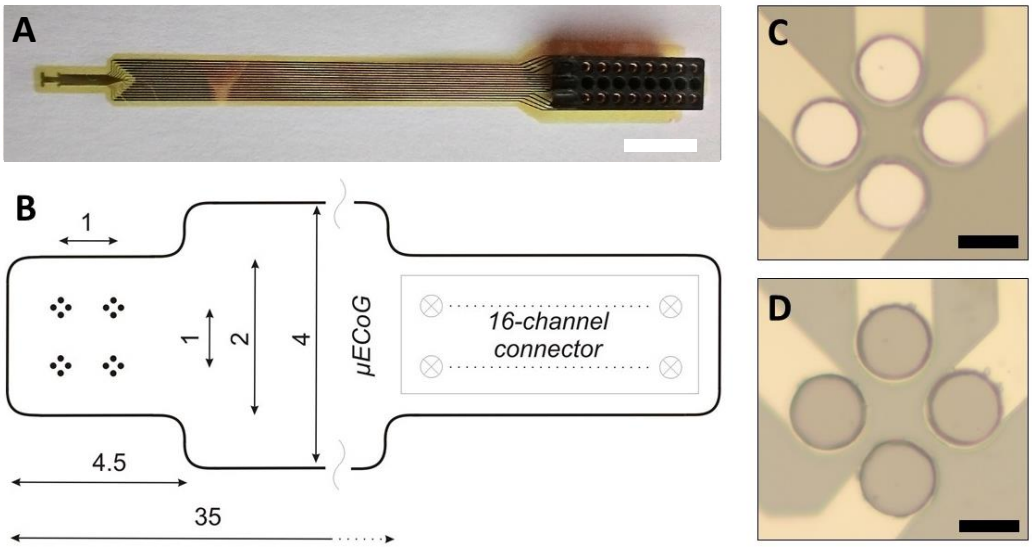

Figure 14. (a) The ready-to-use packaged μECoG device. Scale bar is 3 mm. (b) Schematic drawing with functional part arrangement. Optical microscopic view of smooth platinum (c) and platinum black-coated tetrodes (d). Scale bars are 20 μm for (c) and (d).

3.2.2 Electrochemical deposition and characterization

In order to improve the active surface area, platinization of the recording sites was performed. Two different types of devices were subjected to effective surface area improvement by porous platinum layer: polyimide – based μECoG with 16 platinum recording sites and thiol-ene/acrylate (Shape-memory-polymer or SMP)-based intracortical microprobes with eight gold recording sites. Considering that the deposition parameters (concentration and composition of the electrolyte, electrochemical method, temperature) are the same in both cases, and parameters (the substrate is a flexible polymer and diameter of the recording sites differs by 5 μm) that are important for layer classification are equal, results of material characterization will be discussed in parallel.

In case of μECoG devices, before the platinization process, the sputtered platinum surfaces were cleaned by soaking them in distilled water for 10 min and then by using cyclic voltammetry (CV). In the cleaning step, the voltage was swept between 1.0 V to -0.65 V vs E(ref) at 100 mV/sec in unstirred 0.5 M

H_2SO_4 solution (diluted from 339741 Aldrich, Sulfuric acid, 99.999% solution, Merck KGaA, Germany) for 10 cycles. After every CV cycle, the electrodes were rinsed with distilled water abundantly.

In case of gold electrodes on microprobes, in the pre – cleaning step, CV was used, the voltage was swept between -1.0 – 1.0 V vs E(ref) at 100 mV/sec scanning speed, in unstirred 0.1 M H_2SO_4 solution for 10 cycles. As thiol-ene/acrylate copolymers tend to slightly swell due to the water uptake (approximately 2.5 wt %), the probes were soaked in distilled water before platinum deposition. We used preliminary results from stability test to determine the time required for soaking before platinization. These results were presented previously in *Chapter 2.3.2.*

The platinization was carried out by galvanostatic method from solution of lead free 1 wt % chloroplatinic acid (diluted from 8 wt % H_2PtCl_6 solution in H_2O, Merck KGaA, Germany). Polyvinylpyrrolidone (PVP) was also added to the solution to improve the wettability of the sputtered platinum surfaces. The deposition processes were carried out in a three compartment electrochemical cell, where Ag/AgCl electrode and a platinum sheet were used as reference and counter electrode, respectively. Recording sites have been electroplated by maintaining current density of 10 mA/cm^2. Constant current around 3.14E-05 mA was applied for 150 seconds (d=20 μm) and for 60 seconds (d=15 μm). Current density needed to be kept below 10 mA/cm^2, otherwise desorption of the deposited layer from the surface into the electrolyte occurred [31], [41]. Electrochemical deposition was made individually to each and single recording sites. This individual deposition approach have been made to reduce the variability of site impedances as low as possible. After the deposition, the devices were rinsed with distilled water to remove the free electrolyte from the porous layer.

Durability of platinum black was electrochemically evaluated using EIS (described in sub – chapter of *2.2.2 Electrochemical Characterization).* In case of SMP – based microprobes, same EIS parameters and environment were used for the assessment of uncoated (gold) electrodes, therefore changes in equivalent circuit parameters arise from water uptake of the polymer structural material can be distinguished from changes caused by the degradation of platinum.

Characterization of the recording sites with Electrochemical Impedance Spectroscopy (EIS) was performed before and after the platinum plating process and after *in vivo* use. After *in vivo* experiments the recording sites were subjected to 24 hours of soaking in Terg-a-zyme (Terg-a-zyme® enzyme detergent, Alconox Inc., Merck KGaA, Germany) solution (diluted as 1:100 in distilled water, pH 9.5) in order to remove the physically adsorbed organic particles (marked as “Soaked” on **Figure 16. (a & b)**). Long-term

(three weeks) stability of the electroplated platinum layers was studied by soaking the arrays permanently in distilled water at room temperature. During the soaking experiment, impedance values were measured in every week in 0.01 M PBS solution. First point was measured at the day of the deposition. Average impedance values of 16 channels at 1 kHz are presented in conjunction with standard deviation on **Figure 16. (d)**. For this experiment, a separate device was used and was not implanted later on. EIS measurements were performed as described in *Chapter 2.2.2*.

3.2.3 Cyclic Voltammetry measurements

Cyclic Voltammetry was used to determine the electroactive surface area and to test the electrochemical stability of the platinum black layer. For the characterization of improvement in the active surface area, sealed electrochemical cell and continuous bubbling of oxygen-free, inert N_2 gas flow were used for 40 minutes before the CV measurements to obtain an oxygen free atmosphere. The N_2 gas flow was maintained above the electrolyte during the course of the measurements. After the cleaning procedure (1.0 V to -0.65 V vs E(ref), 100 mV/sec, #10, 0.5 M H_2SO_4) CV curves were measured by sweeping the voltage between -0.22 to 1.0 V vs E(ref) at a scan rate of 200 mV/sec, 10 times in unstirred 0.5 M H_2SO_4 solution.

For electrochemical stability experiments, two methods were used. In the first run, electroplated microprobes (two separate probes) were permanently soaked in 0.01 M PBS for 9 days without the simulated oxidative atmosphere (without daily CV). In the second run, four recording sites on each probes were subjected to daily cyclic voltammetry (CV), while the other four recording sites on the same probes were used as references without daily CV. The daily CV helps to mimic the oxidative physiological *in vivo* environment [184]. Stability test was carried out for nine days while permanently soaking them in 0.01 M PBS solution at 25 °C. CV curves were recorded by sweeping the voltage between -0.22 to 1.0 V vs E_{ref} with a scan rate of 1000 mV/sec, 20 times in the same PBS solution where the arrays were soaked. To evaluate the effect of the mimicked oxidative environment to coating integrity, every site was subjected to daily EIS.

3.2.4 Morphological investigations

The sputtered Pt (labeled later as smooth platinum) and Pt/b-Pt (sputtered platinum/electrodeposited platinum black) structures were analyzed with scanning electron microscopy (SEM) in a LEO 1540XB (Carl Zeiss Microscopy GmbH, Germany) system. Focused ion beam (FIB) method

with Ga ions accelerated to 30 keV was used to cut the Pt/Pt deposits in order to have cross-sectional view of them.

3.2.5 *In vivo* experiments

During *in vivo* studies microelectrode performance has been investigated, when recording sites were electroplated with platinum black or when they left intact made of sputtered platinum (μECoG) or gold (microprobe). To calculate SNR for each recording sites, ratio of the summed squared magnitude of the smoothed signal to that of the noise is identified and calculated. The noise is considered as the variation between the raw signal and the smoothed signal.

Polyimide – based μECoG

The *in vivo* performance of μECoG devices was tested on Wistar rats at Eötvös Loránd University, at the Department of Biochemistry. Wistar rats (300 – 350 gr, a total of 4) were anesthetized and mounted in a stereotactic frame to fix their heads. After cleaning the surgical area, cranial window was opened (approximately 1.2 x 0.7 cm), the dura mater was left intact. After microelectrode and two screw (reference and ground) electrode placement (exact position of microelectrode array can be seen in **Figure 15**.), the bone was folded back and fixed by UV – solidifying cement (Tetric EvoFlow, Ivoclar Vivadent; Liechtenstein), and finally the area was covered with dental cement (GC America Inc.,USA) in case of sub – chronic experiments. In case of acute experiments weight was put on the top of the thinned bone instead of the cement.

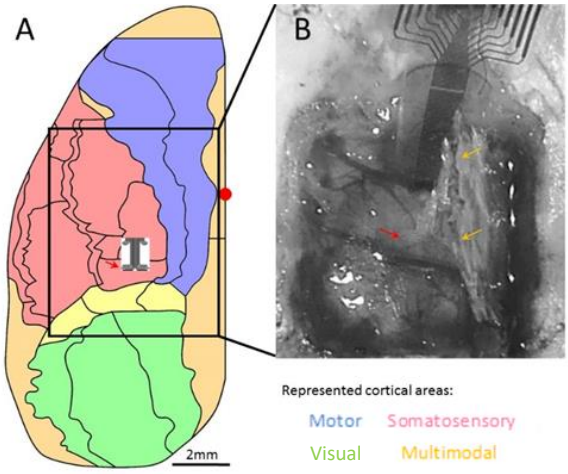

Figure 15. The position of the 4 x 4 channel μECoG device on the brain. (a) The drawing shows the dorsal view of a rat brain) – courtesy of Eszter Ágnes Papp. Different colors labels different functional areas of the cortex and the Bregma is indicated by a red dot. A grayscale image (b) shows an actual surgery and the position of the μECoG device on the brain surface. The red arrow points at the actual recording sites and orange arrows shows the thin bone window. Scale bar is 5 mm.

In both cases, the animals were transferred into a closed Faraday cage, then electrophysiological signals were recorded for at least 30 minutes, using an Amplipex KJE-1001 (Amplipex Ltd., *Hungary*) amplifier system on 16 channels at 20 kHz sampling rate. Matlab (Mathworks Inc., *Natick, MA, USA*) and Spike2 (Cambridge Electronic Design Ltd. *Cambridge, UK*) software were used for off-line data processing and low pass filtering using a 4th order Butterworth filter with a cut – off frequency of 200 Hz.

3.3 Results and discussion

3.3.1 Electrochemical characterization

Polyimide - based μECoG

Representative impedance and phase angle graphs of a selected recording site from a 16-channel electrode array are presented in different experimental periods on **Figure 16. (a & b)**. The characteristic features of impedance and phase curves have changed, especially in the case of phase angle. It is obvious that the magnitude of impedance improved from approximately 2 MΩ to 80 kΩ @ 1 kHz due to platinum deposition. After *in vivo* experiment this improvement was maintained with a slight increase to approximately 300 kΩ @ 1 kHz. Terg-a-zyme treatment had a moderate effect on impedance and phase. A more comprehensive analysis can be achieved by using curve fitting and equivalent circuit analyses of the measured data employing a common method based on the Randles circuit [1], [11], [142]. Related results are shown in **Figure 16**. **(c)**. The equivalent electrical circuit model consists of constant phase element (C_{CPE}) replacing the double layer capacity (C_{DL}) in parallel with charge transfer resistance (C_{RT}) and both in series with electrolyte resistance (R_S) of bulk PBS environment. In order to verify the modeled parameters, numerical calculations were made based on **Equation 3. – 11.**, and their results are demonstrated on **Figure 16. (c)**. Parameters used for the estimation are summarized in **Table 3**.

Table 3. *Calculated and fitted equivalent circuit parameters for smooth platinum and platinum black surfaces*

	Symbol	Calculated		Fitted		Unit
		S-Pt	Pt/Pt	S-Pt	Pt/Pt	
Radius of the recording site	r(s-Pt)/ $r_{est.}$(Pt/Pt)	1.00E-05	6.77E-05	-	-	m
pi	π	3.14		-		
Resistivity of the bulk electrolyte	ρ	0.72		-		Ω*m
Geometric surface area of recording site	A_{geo}(s-Pt) / A_{active}(Pt/Pt)*	3.14E-10	1.44E-08	-	-	m^2

Spreading resistance	**R_S**	**1.80E+04**		**2.32E+04**	**3.92E+04**	**Ω**
Dielectric constant of the free space	ε_0	8.85E-12		-		F/m
Dielectric constant of the electrolyte**	ε_r	78		-		F/m
Distance from the outer Helmholtz plane	d_{OHP}	5.00E-10		-		m
Helmholtz capacitance	**C_H**	**4.34E-10**	**1.99E-08**	**-**	**-**	**F**
Elementary charge	q_e (-e)	1.60E-19		-		C
Boltzmann constant	k	1.38064E-23		-		J/K
Temperature	T	298.15		-		K
Valence	z	1		-		
Avogadro number	N_0	6.02E+23		-		1/ mol
Molar concentration	c	1.00E-02		-		mol/ dm^3
Concentration of ions in the bulk solution	n_i	6.02E+24		-		ions/ m^3
Thermal voltage	V_T	2.57E-02		-		V
Debye length	L_D	3.032E-09		-		m
Applied voltage	V_0	0.025		-		V
Gouy-Chapman capacitance	**C_G**	**2.55E-01**		**-**	**-**	**F**
Constant phase element	**C_{CPE}**	**4.34E-10**	**1.99E-08**	**2.99E-10**	**3.90E-08**	**F**

* Calculated from cyclic voltammetry curve ** 0.01 M PBS [180]

Our analysis revealed that changes in the value of C_{CPE} caused the improvement in site impedance. It was modified from $2.99 \cdot 10^{-10}$ F to $3.90 \cdot 10^{-8}$ F based on average fitted parameters for n = 16. Since, $Z_{CPE}(\omega) = \frac{1}{Q(i\omega)^{\alpha}}$, impedance scales inversely with C_{CPE}, which is proportional to the electrode electroactive surface area, where the impedance goes with $\frac{1}{A\frac{\omega}{2\pi}}$. The fitted spreading resistance (R_S), which is independent from the active surface area, was $R_S = 2.32 \cdot 10^4$ Ω for smooth platinum not changing significantly with respect to $R_S = 3.92 \cdot 10^4$ Ω for platinized platinum. Calculated values obtained for C_{CPE} and R_S are of the same order as fitted parameters, indicating the rightness of the applied Randles model.

During the three weeks long soaking of the μECoG device in distilled water at room temperature, the impedance values increased from 37.0 ± 4.3 kΩ to 102.3 ± 35.4 kΩ that is still in the same order of magnitude (**Figure 16. (d)**) and no sign of degradation or delamination was observed based on optical

microscopic investigations. Conductive particles are assumed to physically adsorbed on the freshly deposited surfaces, which was desorbed from the surface by time.

Variation of impedance were also evaluated both in acute and chronic implantations. The obtained average impedance values were IZI = 1835 ± 503 kΩ for smooth platinum surfaces, IZI = 79 ± 21 kΩ for electroplated platinum surfaces, IZI = 317 ± 186 kΩ after *in vivo* experiments and IZI = 255 ± 126 kΩ after post-implantation soaking in Terg-a-zyme solution. This behaviour is in accordance with literature findings on Pt / b - Pt surfaces [29], [181]. Variation in the average of impedance values in the case of acute and long - term implantation were evaluated, where ΔIZI = IZI (after *in vivo*) – IZI (before *in vivo*). After implantation, the impedance values increased (**Figure 16. (a & f)**), but the average values remained relatively low (an order of magnitude lower than the original). Impedance increase after the *in vivo* experiment is due to the reduction of surface capacitance by an order of magnitude, which is likely caused by organic residuals covering the porous layer even after the enzymatic cleaning treatment. The C_{CPE} decreased from $C_{CPE} = 3.90 \cdot 10^{-8}$ F to $C_{CPE} = 1.14 \cdot 10^{-9}$ F in the case of acute implantation and to $C_{CPE} = 1.60 \cdot 10^{-9}$ F in the case of chronic implantation for platinum black surfaces. Platinum black coatings are considered as stiff materials that is not recommended in chronic experiments [182], because of the assumed weak mechanical stability [183].

The performance of electrodeposited platinum layers on μECoG arrays have never been characterized after *in vivo* implantations. Variation of impedance on three different but functionally identical ECoG electrode arrays (denoted as ECoG electrode „A", ECoG electrode „B", ECoG electrode „C") were measured and analyzed individually before and after black-platinum deposition prior to the acute and chronic operations and thereafter. Average impedance values of 16 channels at 1 kHz on each electrode array are presented in conjunction with standard deviation on **Figure 16. (e)**.

In spite of these preliminary results, our EIS measurements and equivalent circuit analysis showed inconsiderable difference between the impedance and the interfacial capacitance values after each type of surgical procedure (**Figure 16. (f)**).

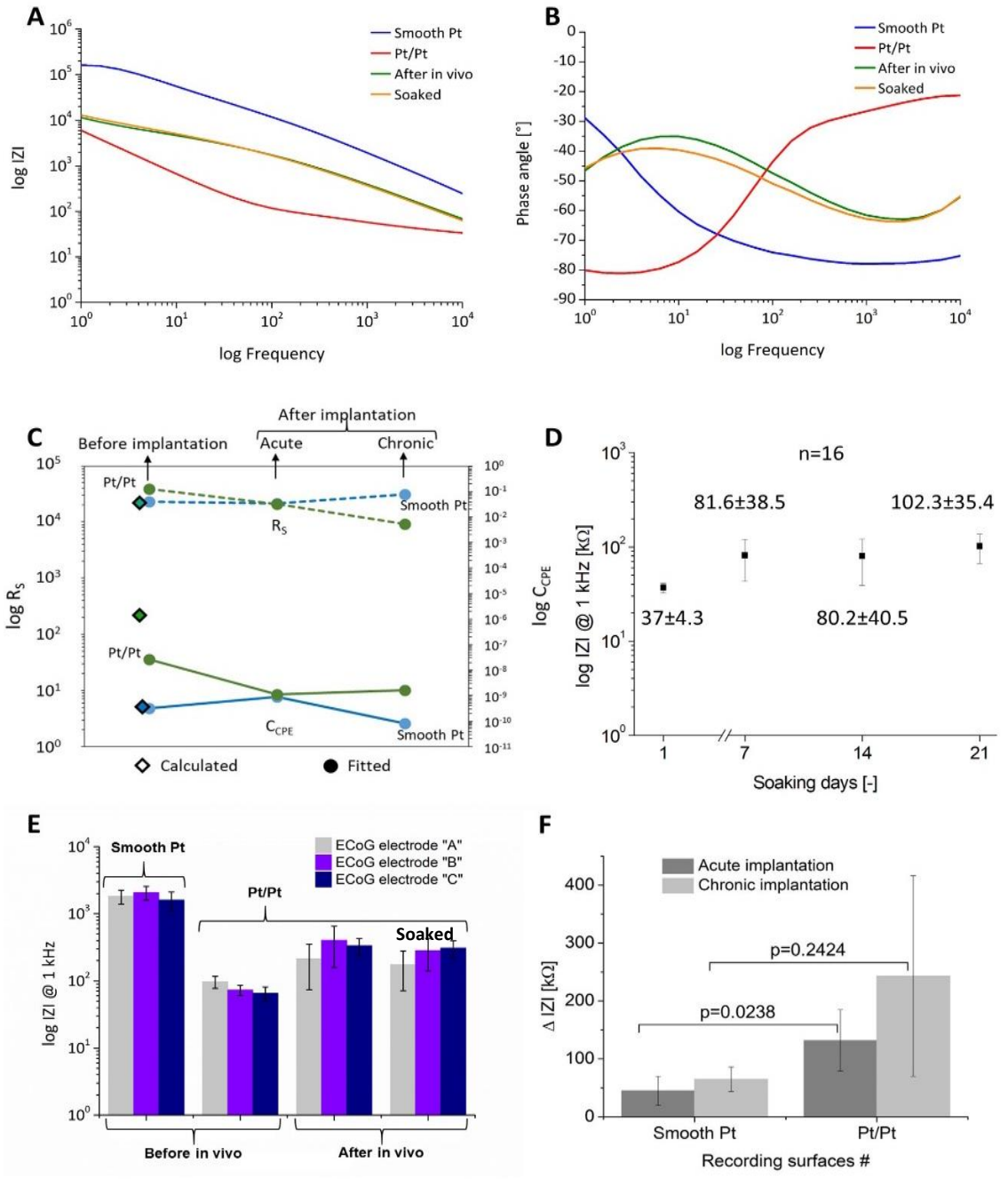

Figure 16. Representative Magnitude of impedance (a) and Phase angle graphs (b) of a selected recording site, measured with EIS on different experimental periods (blue lines representing the smooth platinum; red (after platinization), green (after implantation) and orange (after 24 hours of soaking in Terg-a-zyme) lines representing the platinum black surfaces). (c) Change of fitted (●) R_S (dashed lines) and C_{CPE} (solid lines) parameters derived from equivalent circuit model throughout the lifecycle of smooth (blue) and electroplated (green) platinum sites, involving calculated (◊) values as well. (d) Long-term stability assessment of Pt/Pt surfaces, soaked in DW for 3 weeks @ RT with weekly EIS measurements in PBS. Numerical values for average IZI ± S.D (n=16). (e) Average impedance values at 1 kHz on three different, but functionally identical electrode array (16 recording sites on each device). Z(n=48, Smooth-Pt) = 1835 ± 503 kOhm, Z(n=48, Pt/Pt) = 79 ± 21, Z(n=48, After in vivo) = 317 ± 186, Z(n=48, Soaked) = 255 ± 126. The data are presented as mean ± standard deviation. (f) Variation of average impedance values (ΔIZI = IZI (after in vivo) – IZI (before in vivo)) at 1 kHz recorded after acute and chronic implantation.

In order to support the idea that electroplated platinum has a statistically significant effect on the impedance, analysis of variances (ANOVA) was carried out. The standard deviation of the measurement increases with increasing impedance, therefore the impedance values are transformed. Logaritmization was found to be the adequate transformation. The main effects and the interaction as well were found to be statistically significant. The significance of the interaction means that on each of the arrays, or at least on 1 compared to the other 2, the difference between the smooth Pt (or sputtered Pt) and Pt/Pt are different. Data is visualized on **Figure 17**.

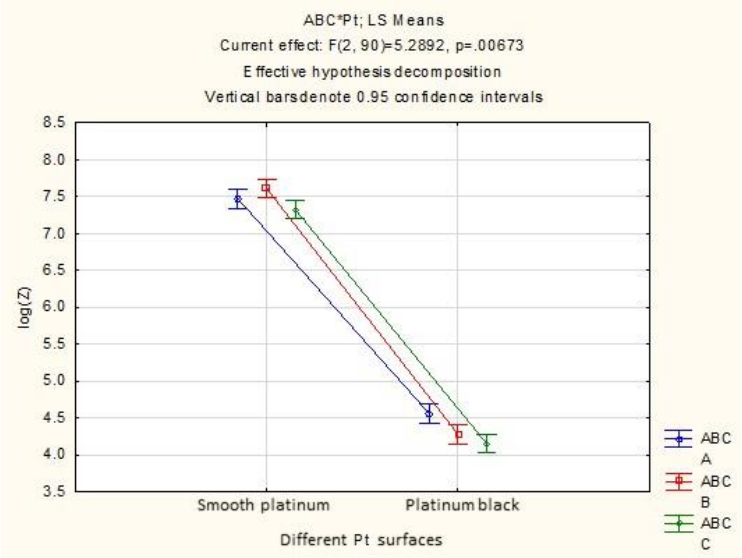

Figure 17. Statistical analysis of electrodeposited platinum to the magnitude of impedance at 1 kHz.

SMP - based microprobe

Durability of platinum black and the effect of in vivo experiments

More extensive study was made on the platinum black surfaces that were deposited on 15 μm diameter gold electrodes insulated with softening polymer (shape-memory polymer - SMP) microprobes used for intracortical recording purposes. Since thiol-ene/acrylate polymers tend to slightly swell due to the water uptake (approximately 2.5 wt %), we performed the electroplating when the ultimate volume was reached, usually after being soaked for 11 days at 37 °C in distilled water. Current density of 10 mA/cm^2 was maintained during the deposition in galvanostatic mode. Each site was deposited individually by adjusting the current density in order to minimize the variability of site impedances.

Impedance magnitude and phase angle of a representative softening microprobe are shown in **Figure 18**. **(a & b)**. Pale grey lines represent single recording sites from an 8 - electrode probe and the

colored, wider lines represent the average values of all recording sites in different experimental periods (1st and 11th day of soaking, after platinum deposition and after explantation). Due to the electrodeposition, the impedance values of the recording sites were improved significantly from 1644 ± 160 kΩ (n=8) down to 60 ± 11 kΩ (n=8) (see black and blue curves is **Figure 18. (a & b)**, and remained relatively low (130 ± 14 kΩ) (n=8) after the explantation. Post-hoc LSD-test confirmed that improvement in impedance due to the platinum deposition and impedance change during the soaking tests were statistically significant ($p < 0.001$). These findings are indicating the same conclusion drawn in the case of flexible μECoG arrays. The deposited platinum significantly reduced the impedance values, and this improvement was maintained after explantation. The main reason behind electrodeposition of porous platinum with its improved electroactive surface area is to keep the real part of the impedance low as this is the major contribution to thermal noise, and therefore the main cause of low SNR. The root mean square voltage due to noise extracted at a frequency of 1 kHz are listed in Table 4., averaged for eight, 15 μm diameter recording sites, in different experimental periods (**Figure 18. (c)**). Nyquist plots revealed (**Figure 18. (d)**) that the impedance decrease after plating is due to the improvement of surface capacitance, which is likely caused by the porous structure of the coating.

Table 4. Magnitude IZI and real part Re(Z) of the impedance and root mean square voltage due to noise $v_{rms}/\Delta f$ at 1 kHz for gold and electroplated gold electrodes, before and after in vivo experiment.

	Au		Au/Pt	After *in vivo* (acute)
	Day 1	Day 11		
IZI @ 1 kHz (kΩ)	2106	1318	55.2	83.2
Re(Z) @ 1 kHz (kΩ)	448	677	52.8	63.3
v(rms)/Δf^(1/2) (nV/√Hz)	84	103	29.2	32.0

Besides the typical measures at 1 kHz, a more detailed analysis is provided on a broader frequency interval (10 kHz, 1 kHz, 100 Hz, 10 Hz and 1 Hz). EIS showed a slight increase by the second day of long-term stability in impedance magnitude over the range from 1 Hz to 10 kHz (from 44.11 ± 2.02 kΩ to 79.32 ± 51.03 kΩ at 10 kHz, from 74.31 ± 6.01 kΩ to 142.22 ± 77.11 kΩ at 1 kHz, from 180.01 ± 10.01 kΩ to 341.13 ± 110.02 kΩ at 100 Hz, from 900.04 ± 79.42 kΩ to 1.33 ± 0.15 MΩ at 10 Hz, from 7.13 ± 0.71 kΩ to 9.93 ± 1.15 MΩ at 1 Hz averaged for 16 recording sites on two electrode arrays) for arrays exposed to PBS at 25°C

(**Figure 18**. **(e)**). Changes in magnitude of impedance at five different frequencies at the first and second day of stability experiment can be seen in **Table 5**.

Table 5*. Changes in magnitude of impedance at five different frequencies (1 Hz, 10 Hz, 100 Hz, 1 kHz, 10 kHz) at the first (Day 1) and second (Day 2) days (in between the main differencies were observed) of electrochemical stability test*

Z (kΩ)	1 Hz		10 Hz		100 Hz		1 kHz		10 kHz	
(n=16)	Mean	S.D.	Mean	S.D.	Mean	S.D.	Mean	S.D.	Mean	S.D.
Day 1	7130.11	710.12	900.04	79.42	180.01	10.01	74.31	6.01	44.11	2.02
Day 2	9932.23	1152.44	1330.21	150.11	341.13	110.02	142.22	77.11	79.32	51.03

Long term stability assessment of platinum black without mimicked in vivo conditions

Slight increase of impedance magnitude was followed by a decrease between the third and fourth day and stabilized between the fourth and fifth day over the range from 1 Hz to 10 kHz ended in a steady state after nine days of soaking (~ -1.45 % at 10 kHz, ~ -1.96 % at 1 kHz, ~ 3.07 % at 100 Hz, ~33.07 % at 10 Hz, ~ 58.70 % at 1 Hz averaged for 16 recording sites on two electrode arrays) for arrays exposed to PBS. Increase in phase angle at lower frequencies (between 1 and 100 Hz) was observed, while a slight increase was measured at 1 and 10 kHz (**Figure 18. (f)**). After five days of soaking, impedance values stabilized around 75.11 ± 3.12 kΩ at 1 kHz for coated sites (averaged for 16 recording sites on two electrode arrays).

Regarding the electrical characteristics, a significant drop in impedance magnitude and increase in phase angle were observed at lower frequencies and an overall decrease in impedance and increase in phase angle were realized during 9 days of soaking period. Uniform decrease in the impedance and almost uniform increase in phase angle suggest a possible penetration of moisture through the polymer layers, resulting in a switch from capacitive to a slightly more resistive state [185], [186]. Similar behaviour of Bode plots is identified in the case of uncoated recording sites, which confirms the hypothesis that this phenomenon is likely due to diffusion of water and solutes into the polymer layers [184].

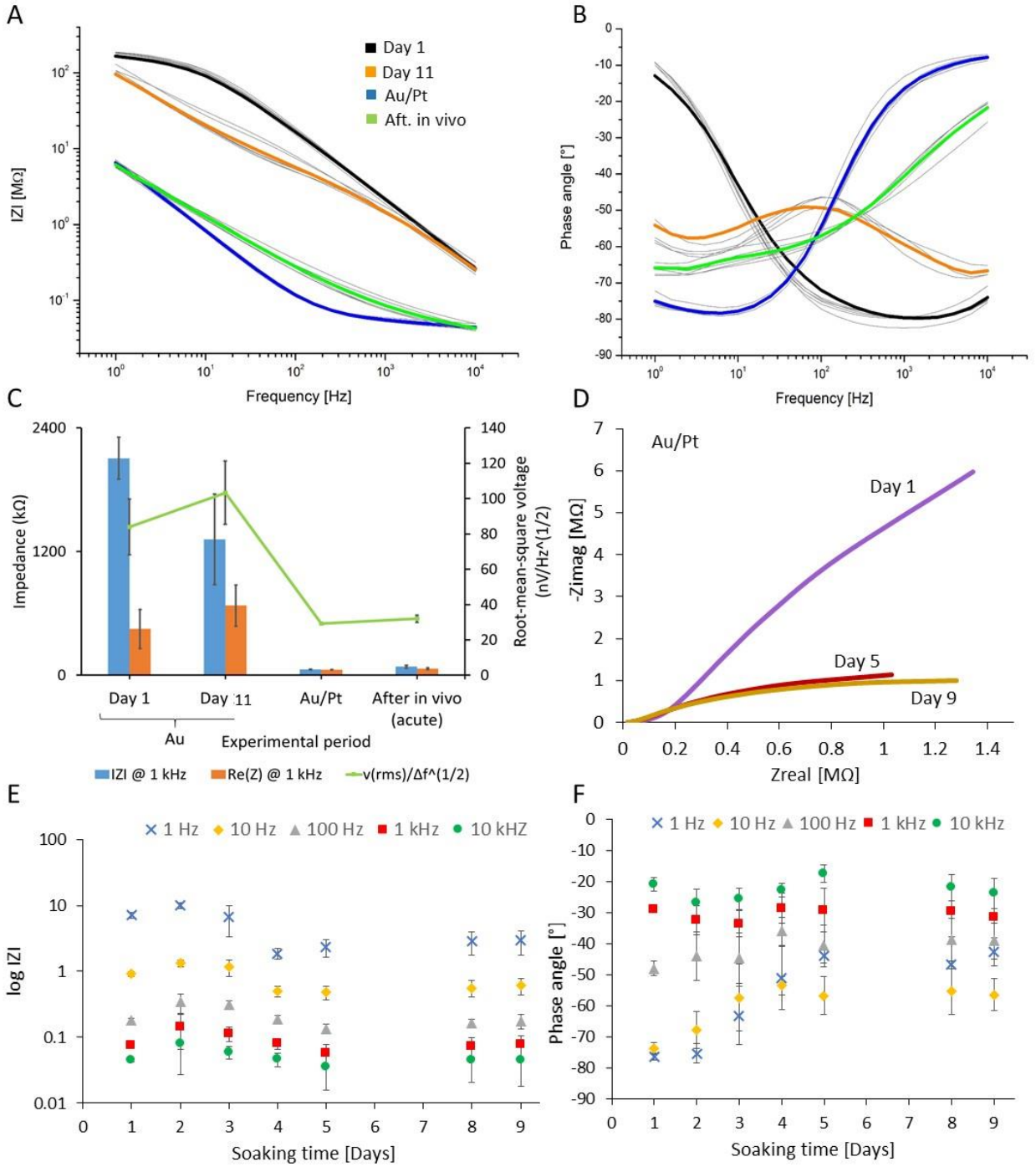

Figure 18. Impedance magnitude (a) and phase angle (b) of all 8 recording sites of a selected probe. Grey lines represent single recording sites; the black, orange, blue and green lines are the average values of all sites, on the first day, the 11th day of soaking before platinization, with platinum back and after the *in vivo* implantation respectively. (c) Average values ± standard deviation for magnitude of Z (blue column) and real part (Re(Z) of the impedance (orange column) and root mean square voltage (green line) due to noise vrms/Δf @ 1 kHz for gold and Au/Pt recording sites during the soaking, after the platinization, and after *in vivo* experiment (n=8, d=15 μm). (d) Nyquist plots of platinized recording site at the 1st (purple line), 5th (red), 9th (brown) day of the long-term stability experiment by constantly soaking them in PBS. (e & f) Average 10 kHz (green circle), 1 kHz (red square), 100 Hz (grey triangle), 10 Hz (yellow rhombus) and 1 Hz (blue cross) impedance and phase angle values of coated electrodes (Au/Pt) during long-term stability experiment. Data is presented mean values ± standard deviation (n=16, 4-4 on two separate probes).

3.3.2 Stability assessment with mimicked *in vivo* conditions

For electrochemical stability experiments, two methods were used. In the second run, four recording sites on each probes were subjected to daily cyclic voltammetry (CV), while the other four recording sites on the same probes were used as references without daily CV. Exact CV parameters were defined in *3.2.3 Cyclic Voltammetry measurement*.

Curve fitting and equivalent circuit analysis were applied to the measured data employing modified Randles model presented in **Figure 19. (a)**. The model consists of a serial resistance (R_S), which describes the resistance of the bulk electrolyte combined with the internal resistance of the electrode, constant phase element (CPE_{DL}) featuring the interface between solid and ionic solution due to charge separation, and can be modeled by Y and α. Y is the coefficient of CPE capacitance per unit length and α is a parameter defined by the phase angle of the CPE, and has values between 0 and 1, where α = 1 represents an ideal capacitor with phase angle 90. Charge-transfer resistance (R_{CT}) characterizes the rate of redox reactions at the electrode-electrolyte interface, Warburg element (W_D) representing the diffusion of ions into the porous electrode, leakage resistance (R_L), the resistance associated with the pseudocapacitance in a low-frequency region [189], and CPE_L related to the pseudocapacitance resulting from Faradaic processes. The fitted data for relevant circuit elements is shown in the inset table of **Figure 19. (b)**. As the resistance of electrolyte is constant, the decreased R_S after 180 cycles may correspond to electrochemical activation of active materials during cycling [190]. After 180 cycles, charge transfer resistance (R_{CT}) slightly decreased probably due to an enhanced ion transport at the electrode-electrolyte interface caused by the increased contact area. However Nyquist plots revealed the dominant reactions are still occurring without charge transition at the surface, consequently in its electrochemical performance non-Faradaic processes are superior to Faradaic processes. Based on our fitted parameters, α slightly changed in both cases (CV and non CV stimulated sites). Since the diffusion path length of the ions in the electrolyte in our test conditions is short, value of Warburg impedance (W_D) remained in the same order of magnitude during the experiment. Leakage resistance (R_L) is usually very high and can be ignored in the circuit. No significant change in pseudocapacitance (CPE_L) is observed. The Nyquist plots are fitted according to the model, and the as-fitted Nyquist plots on the 1st and the 9th day are shown in **Figure 19. (c)**.

It is notable that R_S values also reduced when recording sites were not subjected to daily CV, consequently the change of this parameter may refer to the diffusion of ions through the polymer during soaking in PBS. To conclude the results of CV cycling, this test had only a slight effect on the performance, while soaking conditions had a more dominant influence on the variation of fitted parameters, however

electrochemical properties of the probe were stable under soak testing *in vitro*, and were retained after the implantation process (see more detailed on **Figure 18.**).

A

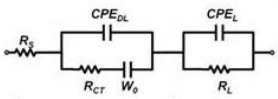

B

	R_S	R_{CT}	CPE_{DL}	α
Right after plating (ref.)	65.11 ± 31.18 MΩ	0.17 ± 0.15 MΩ	21.88 ± 2.22 nF	0.95 ± 0.02
CV cycled (day 9)	3.05 ± 0.62 MΩ	0.01 ± 0.003 MΩ	45.57 ± 11.28 nF	0.90 ± 0.04
Not CV cycled (day 9)	3.23 ± 0.90 MΩ	0.06 ± 0.04 MΩ	52.51 ± 16.97 nF	0.89 ± 0.04

C

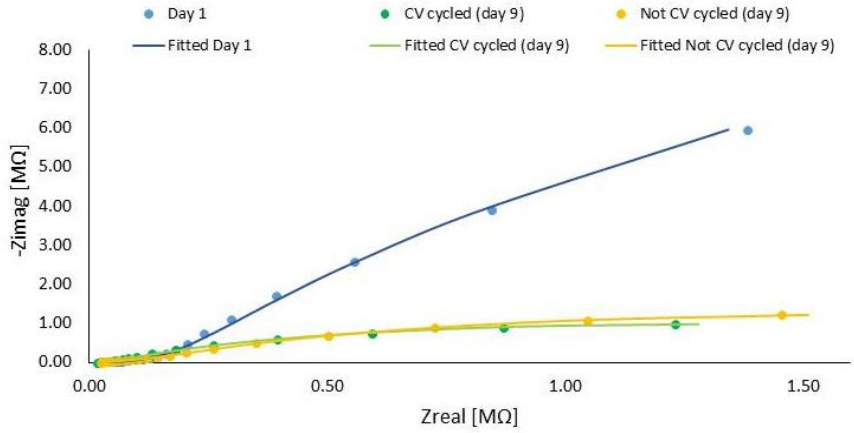

Figure 19. (a) The equivalent circuit of Randle's model for coated electrodes. Copied from [157] (b) Average (4-4 recording sites on 2 individual arrays) fitted model parameters right after plating, after the 1st and 180th cycles are shown in the inset table. (c) Nyquist plot is presented to show complex impedance right after plating (blue circles and line) and after 9 days of soaking with (green circles and line) and without (yellow circles and line) daily CV.

3.3.3 Evaluation of electroactive surface area improvement with CV

The real surface area and the electroactive surface area of the recording sites were computed from the CV curves. During the reduction of the platinum, protons from the acid are adsorbed at the surface of the electrolyte, while during the oxidation, these atoms of hydrogen are desorbed from the surface, represented by a peak at low potentials. This peak corresponds to the amount of charges (charge of a proton is $1.6 \cdot 10^{-19}$ C) released during the oxidation of platinum and also gives the number of adsorption sites present on the electrode's surface. The total charge under the peak was determined by the integration of the anodic peak between -0.18 – 0.12 V vs E_{ref}. This is the so called underpotential deposition of hydrogen (UPD-H) that means hydrogen adsorption takes place at the potentials more positive than the equilibrium potential of hydrogen evolution and specific only to the platinum-group metals. The presence of two adsorption and desorption voltammetric peaks indicate complex distribution of adsorption energies

[187]. The first peak corresponds to weakly bonded, the second to strongly bonded hydrogen atoms [188]. The amount of total charge can be defined as:

$$Q = \int_{t_1}^{t_2} I \cdot d\tau = \frac{1}{v_b} \int_{E_1}^{E_2} I \cdot dE \tag{16}$$

$Q = Total\ charge\ (C)$

$I = Current\ (A)$

$t = Time\ (sec)$

$v_b = Scan\ rate\ \left(^{V}/_{sec}\right)$

$E = Potential\ (V)$

This integral can be also calculated with Gamry Echem Analyst's Integral graph tool. To get the charge value per surface area, Q needs to be divided by 210 μC/cm^2 [188], the electrical charge per unit area associated with monolayer adsorption of hydrogen on ideally flat and polycrystalline platinum surfaces.

The roughness factor (RF) is a common parameter to determine the quality of the deposited porous layer. It is calculated as the ratio of the electrochemically active surface area derived from cyclic voltammetric curves divided by the projected geometric area of the recording site.

$$Roughness\ factor\ (RF) = \frac{Electroactive\ surface\ area\ (\mu m^2)}{Geometric\ area\ (\mu m^2)} \tag{17}$$

Typical roughness factors of electrodeposited platinum are in the range of 20 – 500 [183] without using lead component in the solution of the electrolyte. In our case, total charge calculated from the hydrogen desorption period was 30 nC, the estimated active surface area observed was $1.44 \cdot 10^{-4}$ cm^2, and the roughness factor corresponding to this increased surface area was 23 ± 1.2. Visualization of the electroactive surface are improvement can be seen in **Figure 20**., where blue curve represents the smooth platinum surface and green curve represents the porous platinum surface using scan rate of 200 mV/sec.

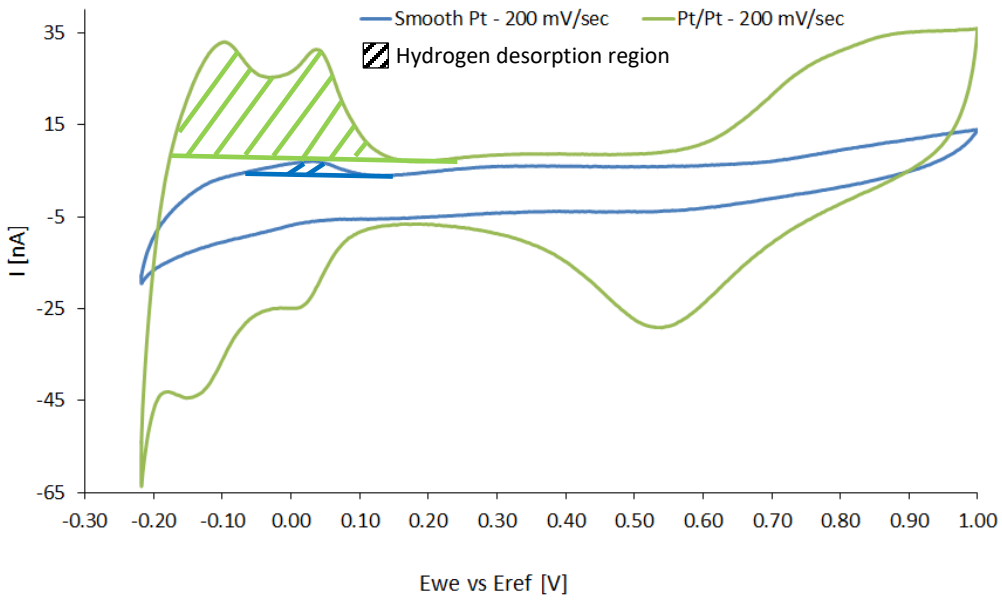

Figure 20. Cyclic Voltammetry curves of sputtered platinum (blue) and platinum black (green) surfaces.

3.3.4 Morphological investigations

Based on the post-implantation SEM images on our electrodes **Figure 21**., crack formation of the platinized platinum layer on several recording sites have been observed at the first time, after specific implantation processes. As we identified this phenomenon, new Pt/Pt structures were studied 1-2 days after the deposition. Based on SEM images, once the platinum black layer has been removed from aqueous environment and the layer has been dried, improvement in site impedance was deteriorated. This dysfunction can be attributed to the dehydration of the porous layer, which appeared as cracks in SEM images. Dehydrated layers caused an increase in the magnitude of impedance at 1 kHz and characteristic features of the Bode plot was also changed. To avoid dehydration, we exposed the recording sites to a permanent bath of distilled water right after electroplating procedure until the surgery was performed. Employing this strategy, we managed to maintain homogenous platinum surfaces without crack formation. Resultant surface morphology of electroplated platinum recording sites shown by Scanning Electron Microscopy and Focused Ion Beam technique provided the cross-sectional insight into the stability of the interface between sputtered and porous platinum layers **Figure 21. (b)**.

These images reveal that the thickness of the electrodeposited platinum layer is in the same range as that of the sputtered thin film (270 nm). Nevertheless, the electroplated layer was found to be

homogenous in thickness throughout the whole surface of the recording sites before *in vivo* experiments. SEM images revealed that platinum black with its morphology, increased the surface area of recording sites, therefore should have a positive effect on the electrode impedance.

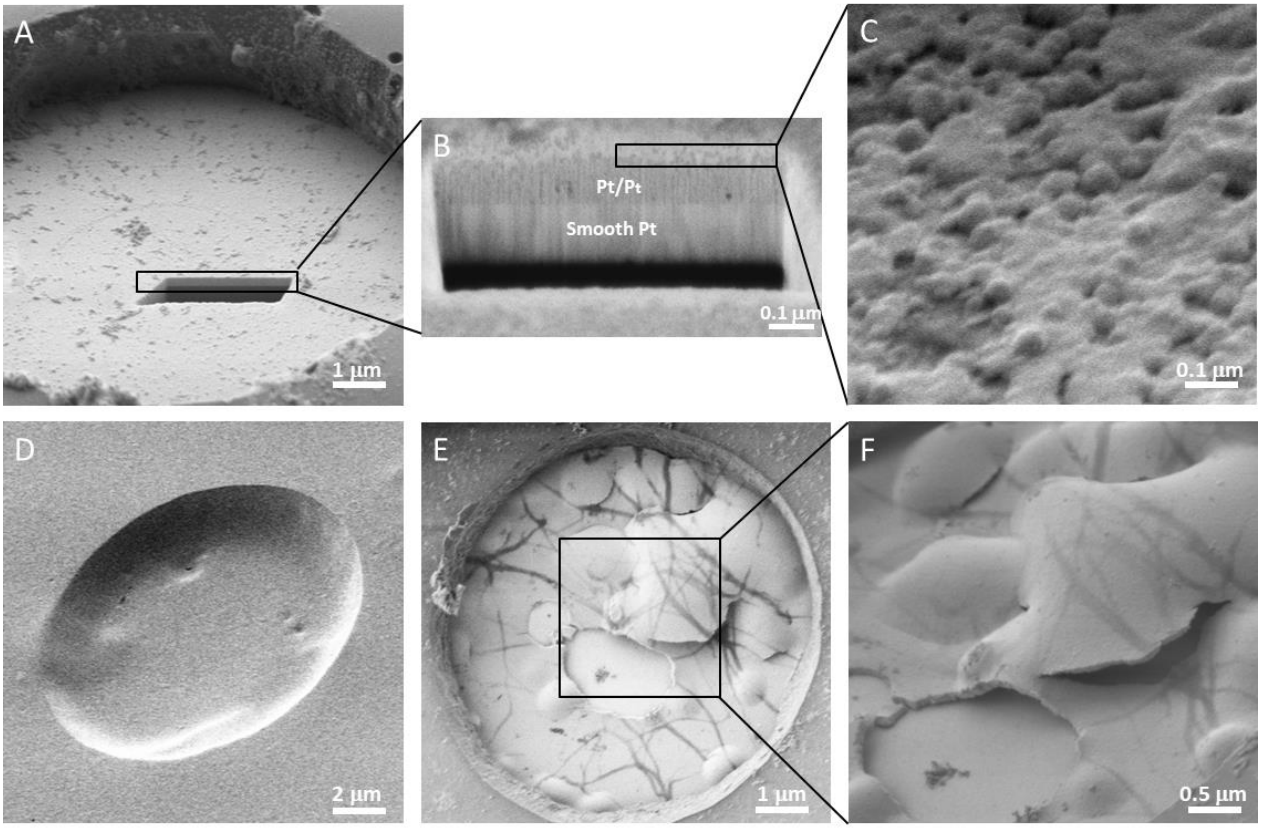

Figure 21. (a) Electron micrograph of a selected electroplated recording site. (b) Cross-section view of the porous platinum / sputtered platinum multi - layer revealed by focused ion beam analysis. FIB revealed that their thickness is in the same order of magnitude (~ 270 nm). (c) Representative surface quality of the porous platinum using higher magnification. (d) Electroplated recording site after explantation. (The site was covered with gold to enhance SEM performance). (e) Crack formation after electroplating, caused by dehydration. (f) Closer view of delaminated platinum black layer.

3.3.5 *In vivo* SNR improvement

Polyimide-based µECoG

In general, the recorded electrophysiological signals are affected by several biological and non-biological noise sources. One of the most relevant noise source is thermal or Johnson – Nyquist noise that has biological (due to the presence of biological tissue) and non – biological origin as well. Thermal noise is coming from the thermally activated fluctuation of charge carriers, and it is directly proportional to the impedance of the recording sites [25]. It is believed that it can be reduced by lowering the electrode impedance, therefore the SNR of neural recordings, and the recording quality can also be improved [191].

The geometric surface area of recording site affects electrophysiological signal amplitude (large contact means low amplitude), therefore the impedance cannot be simply changed by increasing site diameter [25]. Deposition of platinum black has been proposed as an alternative material for noise reduction through the enhancement of electroactive surface area, in case of intracortical microprobes [29], however, possible applications of this porous material in the emerging field of thin and flexible, high-resolution intracranial EEG have not been reported.

Results of related in vivo data are summarized in **Figure 22**. In acute experiments, significant amount of noise superimposed the filtered electrophysiological signals on intact recording sites (**Figure 22**. **(a)**). With respect to **Figure 22**. **(a)**, the sensitivity of electroplated recording sites is remarkably less to main noise sources, resulting in a five-fold decrease in noise power on the fundamental (50 Hz) frequency from 0.53 ± 2.18 mV^2/Hz to 0.11 ± 0.081 mV^2/Hz (**Figure 22**. **(b)**). In chronic experiments (**Figure 22. (c & d**)), thermal noise was determined as a dominant component, strongly impact signal quality. MATLAB functions were used to calculate SNR for each recording sites. Briefly, raw data was low pass filtered with 4^{th} order Butterworth filter with a cut – off frequency of 200 Hz, signals below 200 Hz are considered as useful signals and called as smoothed signal. Afterwards the noise is defined as the difference between raw data and the smoothed signal. SNR was computed as summed squared magnitude of the smoothed signal, divided by as defined noise. SNR is characterized in sleep states only. As shown in **Figure 22**. (**e & f**), SNR significantly improved in chronic cases due to the effective surface area improvement as a result of electroplated platinum, providing a 3.5 times increase from 8.9 to 31.6. This change was, however, only moderate in the case of acute recordings, showing an increase from 30.3 to 39.8. It is supposed that chronic μECoG implants with micron scale electrodes particularly benefit from being electroplated [192].

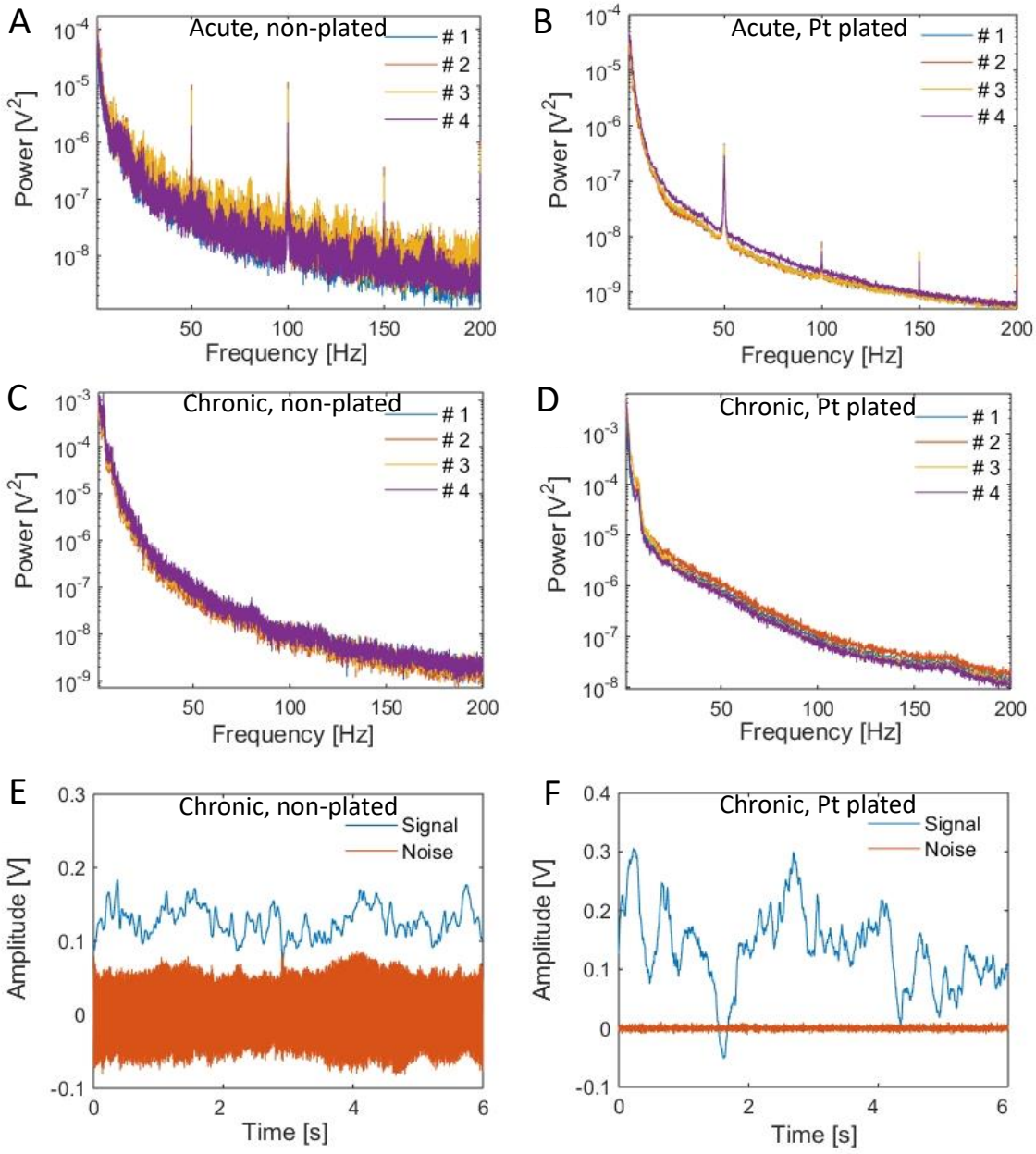

Figure 22. Power spectral density of acute (a & b) and chronic recording (c & d). Data on non-plated electrodes are shown on (a) and (c), while (b) and (d) represent the spectrum derived from the recording of plated recording sites. The curves of four sites of one tetrode are plotted. Figures (e) and (f) shows representative data comparing EEG signals and thermal noise of a non-plated (e) and plated (f) recording site during slow wave sleep after three days in chronically implanted conditions.

3.4 Conclusion and future concept

Polyimide - based μECoG

Polyimide based, flexible μECoG device was designed with 4 x 4 (16) recording sites, each has diameter of 20 μm. Stability assessment (*in vitro* and *in vivo*) of the electrodeposited layer on flexible polyimide substrate have never been shown. *In vitro* (three weeks of soaking in distilled water after electroplating) and *in vivo* validation was performed using Electrochemical Impedance Spectroscopy (EIS). Based on EIS observation, constant soaking of electroplated sites in aqueous medium is crucial to maintain mechanical stability of the porous platinum layer until the surgical procedure. Thanks to the significant decrease in impedance from cc. 1800 kΩ to cc. 80 kΩ at 1 kHz as a result of electroplated platinum, making it possible to measure electrophysiological signals with superior SNR, providing a 3.5 times increase from 8.9 to 31.6. Roughness factor corresponding to this increased surface area was calculated, and with its 23 ± 1.2, it is in agreement with results from other publications (20 – 500 [183]). A slight increase in the electrical impedance and phase angle of the recording sites was induced by the implantation, however, each remained functional during *in vivo* and *in vitro* tests. SEM images confirmed the observation that properly prepared microelectrodes survived both acute and long – term recording sessions from the rat brain tissue. Our results indicate that platinum black deposited on the recording sites of flexible microelectrodes provides a stable interface between tissue and device.

SMP – based microprobes

In the previous chapter (*Chapter 2*), fabrication processes and results on the *in vitro* and *in vivo* validation of a softening polymer microprobe have been shown. Single shank, multi – channel probes are composed of a custom thiol-ene/acrylate thermoset polymer substrate and eight, gold recording sites with diameter of 15 μm. Electroplating of platinum black lowers their impedance from approximately 1600 kΩ to approximately 60 kΩ. Increased electroactive surface area resulted in lower impedance because of higher double layer capacitance and lower charge transfer resistance. In order to mimic, the harsh oxidative *in vivo* environment in experimental conditions, four recording sites on each probes were subjected to daily cyclic voltammetry (CV), while the other four recording sites on the same probes were used as references without daily CV. To conclude the results of CV cycling, this test had only a slight effect on the performance, while soaking conditions had a more dominant influence on the variation of fitted parameters. EIS data was investigated at five different frequencies in order to more accurately predict the failure mechanism of insulation layers. Electrochemical performance of the probes implies that the

electroplated layer remained stable and was not damaged at various experimental stages eg. soaking tests, handling, implantation, and explantation. Optical microscopic investigation did not show any visible change in appearance due to possible delamination or degradation. Neuronal spiking activity was detected during our *in vivo* study with a maximum SNR of 6.24. This SNR is somewhat above the value reported by Ware *et al.* [145] using a softening microprobe of electroplated recording sites. We hypothesized that higher SNR ratio can be partially attributed to lower impedance values. In the future, chronic *in vivo* experiments are planned to test the long term reliability and stability of the recordings with electroplated platinum on softening polymer implants. We are also planning to compare chronic *in vivo* performance with that of silicon probes of the same dimensions. Benefit from changing the rigid substrate material (eg. Si) to a softening polymer and the influence of the as-reduced mechanical mismatch between our device and the brain tissue on the neuroinflammatory response needs to be evaluated.

Thesis statement related to this chapter

I designed and developed the microfabrication process flow of a flexible polyimide – based microelectrode array, and characterized the stability of platinum black layers that was electrodeposited on μECoG and SMP – based microprobe. In case of μECoG, the designed neural interface, with electrode diameter of 20 μm is able to record electrocorticography signals. 20 μm site diameter inherently indicates higher impedance and consequently lower signal – to – noise ratio. I increased the electroactive surface area with galvanostatic deposition of porous platinum. Hence, the electrodeposition the electrode impedance decreased from 2 MΩ to 80 kΩ, additionally, thermal noise varied from 130 nV/√Hz to 29 nV/√Hz, resulted in higher SNR from 8.9 to 31.6 in sub – chronic *in vivo* experiments. Analyses of Bode-plots indicate that platinum black deposited on the recording sites of flexible microelectrodes remains stable during implantation and provides a reliable recording interface between tissue and device. Observations based on equivalent circuit analyses proves that impedance improved due to higher double – layer capacitance and lower charge transfer resistance. In case of intracortical microprobes, I lowered the initial impedance to approximately 60 kΩ due to galvanostatic deposition of porous platinum.

Scientific paper related to this thesis statement

A Zátonyi *et al.*, A softening laminar electrode for recording single unit activity from the rat hippocampus, *Scientific Reports*, Vol. 9, 37237, **2019**

A. Zátonyi *et al.*, *In vitro* and *in vivo* stability of black-platinum coatings on flexible, polymer microECoG arrays, *Journal of Neural Engineering*, 15, 054003, **2018**

4 FLEXIBLE, TRANSPARENT μECoG DEVICES FOR MULTIMODAL NEUROIMAGING

4.1 Introduction

Multimodal recording schemes are taking advantage of neuroimaging technique's spatial resolution and electrophysiology recording's temporal resolution (submilliseconds range) holds great potential to reveal the anatomical and functional connectivity of neuronal ensembles [193], [194]. One approach is the application of flexible sub- or epidural μECoG arrays that are transparent considering both the substrate and the conductive layers as well. Several methods have been made to fabricate transparent devices, and the next subsection will give examples to represent the evaluation of those strategies.

Materials for transparent neural interfaces

Common conductive materials as metal films (platinum [195], [196] gold [197], [198], gold/platinum [199]–[201], iridium [196]) are inappropriate for imaging purposes as they block the field of view, and they have obvious contribution to light-induced artefacts as a consequence of their small energy bandgap. Candidate materials for imaging purposes are ultrathin nanowires [202], nanomesh structures [38], [39], graphene [203]–[205], carbon nanotubes [206], conducting polymers (eg. PPy, PEDOT) [163], [170], [207] and indium – tin – oxide (ITO) [154], [208]. Frequently, ITO thin film is considered as brittle material [208]–[210], therefore it was not recommended for flexible electronics [211]. Besides mechanical properties, optical, photovoltaic characteristics and biocompatibility are also features which also need to be taken into consideration. ITO is not entirely transparent [204], [208], [212]–[214] (T_{ITO} > 80% at VIS-NIR wavelengths) and it is getting worse with thickness. Electronic band structure of ITO, conduction is mediated by oxygen vacancies that feature large bandgap (2.6-3.65 eV), therefore low sensitivity to photovoltaic artefact is predicted as photons in the visible (VIS) and infrared (IR) spectral range have less energy [215], [216]. Graphene has similar characteristics with higher UV transmittance than ITO, however, its integration to microfabrication processes is more complicated. Each graphene monolayer deteriorates the transmittance by ~2.3% [217], and has a small energy bandgap as such exhibits a pronounced photovoltaic artefact [214], [218]. Additionally, with the application of graphene, other metal (like gold) interconnections are needed to stabilize the connection between recording sites and the connector [204], [217], [219]–[221]. Photovoltaic artefacts can be restricted during neuroimaging by the use of large energy bandgap semiconductors (eg. ITO) or bypassing the illumination of the recording sites and traces made of non-transparent materials [38], [222], which limits the freedom to arbitrarily select the scanning areas.

Biocompatibility was also mentioned as a key criteria for materials in neural applications. Fortunately, there are several validations with regard to the biocompatibility of ITO [223], [224].

Polymers are the most widespread choice of substrate materials, eg. polyimide [195], [225]–[229], combination of SU-8 and polyimide [100], Polydimethylsiloxane (PDMS) [231], [232] and Parylene C [13], [33], [217], [233]–[235] are used. Besides this selection of materials, the Parylene family, classified as a poly(para-xylene), is an outstanding candidate for neuroimaging applications. Because of Parylene HT has distinct chemical composition (alpha hydrogen atom of the N dimer is replaced with fluorine, while the dimer of Parylene C is modified by the substitution of a chlorine atom), its optical, thermal and electrical properties differ from those of Parylene C. Parylenes are deposited by chemical vapor deposition (CVD), which enables conformal, pinhole-free coating. Parylene HT has a continuous service temperature up to 350 °C, while other polymer from the Parylene's family and even beyond definitely tolerate lower process temperatures. Besides outstanding thermal characteristics, Parylene HT defines superior dielectric properties by exhibiting the lowest dielectric constant among Parylene variants (SCS, Data Sheet [236]). Parylene HT exhibits low initial auto-fluorescence and its transmittance is also superior to other polymer materials [237]. A more detailed comparison of polymer materials for neural applications is shown in **Table 1.** Considering biological requirements, poly(para-xylylene) is classified as USP class VI implantable material, furthermore several studies have certified its biocompatibility [127], [207], [238]–[241]. Currently, Parylene coatings are applied as part of pacemakers, and are also used as 3D conformal coatings in retinal implant.

Regarding the technology of device fabrication, Parylene HT has further advantages, since this material has the lowest moisture absorption among polymer-based implant materials, which guarantees the low risk of delamination due to swelling. Besides the fact that Parylene HT has the lowest sensitivity to water absorption, it is also defined as a possible candidate to encapsulation material of medical devices in human field of research.

4.1.1 Targeted *In vivo* applications

Before moving on to the design, fabrication and testing of the transparent microdevices, I briefly introduce the background of two neuroimaging technique used later on for *in vivo* validation of the implantable microdevices.

Intrinsic Optical Signal Imaging (IOSI)

Intrinsic optical signal imaging (IOSI) records tiny optical changes associated with metabolic activity of neural tissue. Local neuronal activity dependent changes in the oxygen saturation of hemoglobin causes changes in physical properties of the tissue itself, which affect light reflectance from the exposed cortical surface [242]–[245]. Activity-related scattering has been associated as a consequence of changes in three main component. The first component is the increase of deoxyhemoglobin concentration due to exalted oxygen consumption of the active neurons. The second component is the activity-related increase in blood flow (vascular supply) in order to decrease deoxyhemoglobin and increase the oxyhemoglobin concentration in the related active areas. The third one may attributed to expansion and contraction of extracellular space and neurotransmitter release [246]. The intrinsic signals arise from the variation in reflectance change between active and inactive regions in response to the external stimulus. Each above listed components has its own contribution to the intrinsic signals since they have typical time-course response and their relative contribution (amplitude) depends on the wavelength of the illumination [247]. During IOSI experiments, wavelength between 605 – 630 nm are used to illuminate the surface of the brain as deoxyhemoglobin has a higher absorption coefficient in this range, therefore active cortical regions can be distinguished as it reflects less red light [248]–[250]. The advantage of IOSI is that functional architecture of neuronal populations of active cortical regions can be visualized with spatial resolution greater than 4 μm [251], it provides visual information on the functional cortical architecture in a minimally invasive way. Images, deriving from the reflection of light in relation with neuronal activity, are recorded by a CCD camera.

Simultaneously measured hemodynamic changes and electrophysiology recordings from the same cortical area may reveal the correlation between intrinsic signals and neuronal firing, consequently may provide additional insight into the connectivity network of functional domains. In order to investigate the simultaneous use of IOSI and μECoG (micro-electrocorticography) techniques, polyimide/ITO based subdural microelectrode array was introduced into the cranial chamber used for *in vivo* functional mapping of the primary visual cortex in anaesthetized cats. Our collaborators in the completion of *in vivo* experiments was Neuroscience Research Group, University of Debrecen, Debrecen, Hungary.

Ca^{2+} signal imaging with two-photon (2P) microscopy

Two-photon microscopy is a laser-scanning, multifocal technique, typically collects fluorescence light from single location, while the focused beam of a laser is scanning over the neural tissue and the reflected

fluorescence intensity is displayed as a function of position [243]. Two-photon imaging uses near-infrared wavelengths (700-1000 nm), where light has its maximum depth of penetration in biological tissues [252], [253]. As a consequence of the localized excitation (clearer background and less phototoxicity), the submicron (< 1 μm) spatial resolution and the extraordinary brightness of emitted fluorescent light (contributing to high SNR) [254], two-photon microscopy is ideal for the study of dynamic cellular and subcellular processes [255], [256].

Calcium imaging with two-photon microscopy has been extensively studied and widely used to image neural activity *in vivo* in upper cortical layers of the brain [255], [257]. Ca^{2+} ions are important for cellular signaling and signal transduction. In neurons, it takes part in depolarizing signal transmission, therefore it is partly responsible for the evolution of synaptic activity [258]. In two-photon imaging, they use chemical or genetically encoded calcium indicators (eg. GCaMP: GFP-Calmodulin-M13-Protein). The later ones are fluorescent molecules that can respond to the binding of Ca^{2+} ions by changing their conformation that induces higher fluorescence intensity due to deprotonation of the chromophore [259].

Unlike high spatial resolution (high enough to resolve synaptic structures) of two-photon microscopy, the achievable temporal resolution is limited by slow (> 100 ms) intracellular calcium-binding kinetics [193]. Additionally, the area of interest that can be covered is relatively small (with a high NA objective ~ 1 x 1 mm) [255]. Combining two-photon microscopy with electrophysiology recording has several advantages eg. provides more information about the role of different neurons in the neural network, and finds correlation between electrophysiological changes and calcium signals. One approach to record electrophysiology is based on flexible μECoG arrays, where both the substrate and the conductive material are transparent. Material selection have been discussed in the *Introduction 4.1, Materials for transparent neural interfaces.* The next subsection will describe in details the design and microfabrication of μECoG with the selected composition of materials (Parylene HT/ITO/Parylene HT).

4.2 Methods

4.2.1 Design, microfabrication and packaging

Polyimide – based μECoG

The polymer μECoG arrays consists of 32 recording sites with diameter of 300 μm and 500 μm inter-electrode distance (center-to-center). The fabrication of polyimide-based cortical neural interfaces follows the same process steps as described in *Chapter 3.2.1*, except for the use of transparent conductive

material, ITO for multimodal imaging purposes. Briefly, the microfabrication process started with the spin-coating and curing of 4 μm thick polyimide onto the silicon wafer that was previously treated with 1:20 HF. Lift-off pattern for ITO was formed with spin-coating and pre-baking (100 °C, 2 min) of Ti35 Image Reversal Photoresist (Microchemicals GmbH, Germany). UV dose of 200 mJ/cm^2 was applied, followed by a relaxation time of 10 minutes, and a reversal bake at 130°C for 2 minutes on a hotplate. Second exposure with a UV dose of 500 mJ/cm^2 was used. For adhesion improvement between polyimide and ITO, oxygen plasma strip at 80 W for 30 seconds was used. 90 nm/min deposition rate and 300 W RF power were used to form ITO conductive layer in a Leybold-Heraeus Z550 RF sputtering equipment in argon atmosphere. Lift-off process was completed by soaking the wafers in acetone bath. A second layer of polyimide was deposited and cured, thereafter 100 nm aluminum as hard mask for Reactive Ion Etching was e-beam evaporated and patterned by photolithography using Microposit 1818 positive photoresist and applied as described previously in *Chapter 3.2.1.* The aluminum was wet-etched in a solution of H_2O:H_3PO_4:CH_3COOH:HNO_3 = 2:16:1:1, then the polyimide was selectively etched above the recording sites and electrode contour in CF_4/O_2 plasma (gas ratio was 1:4). The aluminum was then completely removed in the same aluminum etchant. The released μECoG structures were gently peeled off the wafer by tweezers. Connector pads in the backbone of the arrays were mounted on a 2 x 16 channel Preci-DiP electrical connector (Preci-dip SA, Switzerland) using CW2400 silver epoxy glue. Device layout, similar to final microelectrode design can be found in Figure 24. (e).

Parylene HT-based μECoG

In this case, each cortical neural interface has 32 recording sites with 150 μm site diameter, and composed of 2 x 8 μm thick Parylene HT (SCS, UK) and 100 nm thick ITO conductive layer. The center – to - center interelectrode distance was 500 μm. Its microfabrication relies on the same MEMS technologies including photolithography, bulk micromachining etc. as described before in *Chapter 3.2.1*. The main difference between the previous processes is the application of Parylene HT as substrate material instead of polyimide. The whole deposition process of Parylene HT have been made by Specialty Coating Systems Inc. (SCS, *UK*). For the formation of bottom insulating layer a DSP (Double Side Polish) silicon wafer was immersed to 1:20 HF solution for 30 seconds, then releasing agent was used to facilitate the releasing of the final arrays from the wafer. After the vaporization process (at 150 °C in vacuum) of the powder-like material made up of dimers, dimeric gas was formed. After vaporization the gas was sent to a pyrolysis chamber, where the dimer was cleaved to its monomeric form at 690 °C, 0.5 torr. Afterwards, the gas composed of monomers was pumped into a room temperature deposition chamber where the

transparent polymer film was formed on the surface of the Si wafers. Ti35 Image reversal photoresist was used for the lift-off process of ITO with the same parameters as described before in this chapter. Oxygen plasma strip was used before the sputtering. Adhesion promoter was applied prior to encapsulating with 8 μm thick Parylene HT. The exposed Parylene HT surfaces were removed in high-density O_2 plasma in a Deep RIE System at 1000 W power (0.7 μm/min etching speed) through 100 nm thick aluminum masking layer. Since aluminum etchant is a mixture of strong acid, chemical reaction with thin film aluminum is intensive (accompanied by H_2 gas formation), therefore another aluminum etchant had to be introduced to reduce the etching speed. Standard aluminum etchant was replaced with 0.025 M NaOH solution and the temperature was lowered from 50 °C to room temperature. Wafers were soaked in distilled water for cc. 2 weeks, when the arrays were finally released from the silicon surface. Electrode structures were mounted on a 32 channel Preci-DiP connector with a two-component silver epoxy glue. Back of the connector pins were covered by Araldite 2014-1.

4.2.2 Optical characterization

For IOSI purposes, where polyimide – based μECoG was used for multimodal imaging, illumination at 609 nm was selected as deoxyhemoglobin has a higher absorption coefficient in the wavelength range between 605 - 630 nm. The images were acquired with CCD camera in a wavelength between 540 - 900 nm. The intensity of the collected signals were substantially influenced by the substrate material. To quantify the optical intensity loss through the 8 μm thick polyimide – based μECoG, optical transmission was determined with a custom-designed spectrophotometer.

To perform simultaneous two-photon Ca^{2+} imaging and ECoG recording *in vivo*, neural cells were labelled with green fluorescent protein-based calcium sensors. In our study GCaMP6f (GFP-Calmodulin-M13-Protein) sensors were chosen. The expressed GCaMP6f in the cell membrane can be excited around 454 nm and their emitted fluorescence light can be detected around 510 nm. During two-photon imaging, two photon combines their energy at the focal point, therefore the excitation light arises from near-infrared wavelength range that is less scattered in biological tissue, hence 910 nm was used to excite GCaMP6f sensors. Relatively low auto-fluorescence of the polymer substrate is desired to avoid the disturbing background noise, when collecting fluorescence signals in real-time from fluorescent proteins which interacts with a Ca^{2+}-binding proteins. To achieve the highest excitation depth and spatial resolution of GCaMP6f signals, transmission and auto-fluorescence behaviour of the proposed material composition had to be evaluated. In contrast to Parylene HT, Parylene C is a popular substrate of transparent neural implants, so we used it as reference material in our measurements.

In order to show that the application of our transparent devices in the optical pathway is reasonable, we determined transmission spectra, considering the above mentioned wavelength ranges. 400 – 980 nm was selected for optical characterization of different polymer substrate materials and polymer/ITO structures. For the optical characterization, Cary 17, a custom-designed spectrophotometer was used. Visual and near-infrared spectral range was selected for optical measurements, as VIS-NIR lights cover wavelength of the electromagnetic spectrum from approx. 350 – 2000 nm. The light source was a Xe flash lamp, the beam passed through a monochromator, then the reflected light alternately reached the sample (polymer materials) and the reference. The contact area was 8 mm in diameter. The transmitted light from the two passways alternately reached the photomultiplier detector.

Auto-fluorescence characteristics was analyzed with a Fluorolog 3 spectrometer (Horiba Ltd*., Japan*) at room temperature, equipped with 450 W Xe arc lamp, double-grating excitation (260 – 600 nm, with 10 nm step size), and emission (270 – 800 nm, with 2 nm step size) monochromators.

4.2.3 Electrochemical characterization

For electrochemical characterization Electrochemical Impedance Spectroscopy (EIS) was used, and parameters were defined as described previously in *Chapter 1.3.1* and *Chapter 2.2.2*. Three electrode setup was assembled in Faraday-cage with Ag/AgCl reference electrode (ET072-1, eDAQ Pty Ltd., *Australia*), platinum wire as counter electrode and recording site as working electrode. Experimental control and data Gamry Reference 600 (Gamry Instruments, *Warminster, PA, US*) potentiostat was used to control the experiments, in a frequency range of 1 Hz – 10 kHz. Small amplitude sinusoidal alternative current (AC) was used as excitation signal (25 mV RMS) on a cell, with five points per decade and 0.01 M PBS (pH = 7.4 @ 25 °C, Merck KGaA, Germany) solution was used as electrolyte.

Because lots of results have been reached and presented in this thesis regarding the characterization of polyimide – based devices with platinum electrodes, present chapter will mainly focus on the effect of ITO on the long-term stability of polymer-encapsulated structures. μECoG devices with 32 recording sites were constantly soaked in 0.01 M PBS solution for 16 days at room temperature. Bode plots were recorded every day in the same PBS solution at RT as well.

Electrochemical characterization of Parylene HT-based μECoG were tested in harsher-than physiological conditions to demonstrate device reliability and long-term stability. Accelerated aging test method, when using elevated temperature, is a time saving way to simulate the degradation mechanism of complex electrode structures, where polymer and conductive materials are stacked. As described

previously in *Chapter 1.3*, based on empirical observations [17], rate of chemical reactions increases exponentially with increasing temperature and can be expressed with the following equation:

$$T_{Simulated} = T_{Experimental} \cdot Q_{10}^{\Delta T/10} \quad (18)$$

,where Q_{10} is the aging factor for 10 °C increase or decrease in temperature, and it equals two [18], $\Delta T = T - T_{ref}$, where T_{ref} will be the body temperature (37 °C).

Functional μECoG devices with 32 recording sites were constantly soaked in 0.01 M PBS solution at elevated temperature of 67 °C, to decrease the time of stability experiment. Long-term degradation mechanism of the proposed structure was monitored in a daily manner during EIS measurements at room temperature.

Gamry Framework 7.8 and Gamry Echem Analyst 7.8 software were used for experimental control, data acquisition and equivalent circuit analyses. In the Impedance Model Editor of Gamry Echem Analyst software, common and simple Randles circuit as an equivalent electrical circuit was constructed. Randles circuit consists of the resistance of the electrolyte (R_S) in series with the parallel combination of the Constant Phase Element (C_{CPE}), replacing the Double Layer Capacity (C_{DL}) and the impedance of faradaic reactions (R_{CT}). Diffusion of ions from the electrolyte to the electrode's surface is represented by Warburg element (W_D), in series with R_{CT}. The C_{CPE} is modeled using two terms: Y that is the coefficient or real part of the capacitance and independent from frequency and α that is a parameter defined by the phase angle and expresses the frequency dependence. When $\alpha = 1$ and $\theta = 90°$, is identical to an ideal capacitor but considering real surfaces with inhomogenities $0 < \alpha < 1$ and is believed proportional to surface roughness and charge uniformity [21].

4.2.4 Mechanical characterization

These electrodes had to stand mechanical loads, mainly bending loads during the positioning of the electrical connector attached to the μECoG and primarily during the surgical procedure, as all device components are fixed after closing the cranial chamber. Cyclic bending loads are presented only during the implantation, when devices are perfectly positioned into the cranial window and are fixed underneath the dura mater. ITO – based electrode structures are believed to be sensitive to mechanical loads and show failure due to breaking because of the delicate metal-oxide structures.

Figure 23. is representing the bending principles, copied from F. Kohler *et al.* [44], where they used the same test principles, only the implementation and test apparatus is different. For "sandwiched" polymer/conductive layer/polymer structures, flexural or bending stiffness is the measure that defines structural integrity. Bending stiffness $(E \cdot I)$ can be defined as [44]:

$$E \cdot I = \frac{M_b}{r} \tag{19}$$

$E = Young's\ modulus\ \left(Pa = \frac{kg}{m \cdot s^2}\right)$

$I = Moment\ of\ inertia\ (kg \cdot m^2)$

$M_b = Bending\ moment\ (N \cdot m)$

$r = \text{Bending radius}\ (m)$

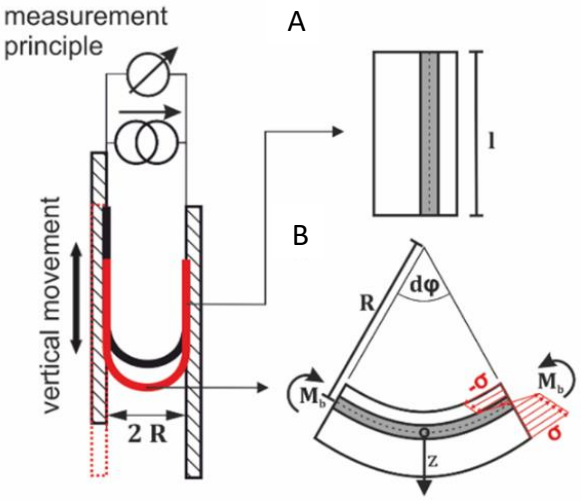

Figure 23. Functional principle of the bending test with simultaneous 4-wire resistance measurement. a) Outline of a non-bended electrode segment (length l), b) shows a segment under bending load including stress (σ) development and bending moment M_b. R is representing the bending radius, dφ is the bending angle. Copied from [44].

To demonstrate the robustness of the proposed constructions based on polyimide and Parylene HT, an individually adaptable, custom-designed bending device was developed controlled by a stepper-motor and Arduino board. Measurements were conducted with the help of a GPIB-USB-HS (National Instruments, US) controller with Keithley 236 and Keithley 707 integrated as Source Measurement Unit (SMU) and Switching Matrix respectively. Photograph of the measurement setup can be seen in **Figure 24. (a).**, including the bending device, breadboard and BT-305 Power Supply. Data acquisition and hardware operation were operated by LabVIEW. Assembly of the bending device can be seen in **Figure 24. (b).** Plastic table served

as the frame for the bending device, stepper-motor was fixed at one side of the frame so that the axis of rotation is in line with the axis of bending. For the positioning and fixing of the cylinder (define the bending axis with diameter of 1 mm) adjusting elements were 3D printed using Witbox 2 printer (BQ, Spain) and polylactic acid (PLA) filament and designed with SolidWorks 2015 CAD software. Different test structures were used for mechanical characterization of polyimide and Parylene-based arrays. Test structures used for bending experiments with their main parameters can be seen in **Figure 24. (d & e).** ITO and platinum was used as conductive layer for polyimide encapsulation material. Test structures that contained platinum or gold conductive traces were used as reference for mechanical characterization of polyimide and Parylene-based constructions with ITO. Parylene C was used with gold as ITO has poor adhesion to Parylene C and also because Parylene C / gold is a common material composition that can be used as reference in comparative experiments.

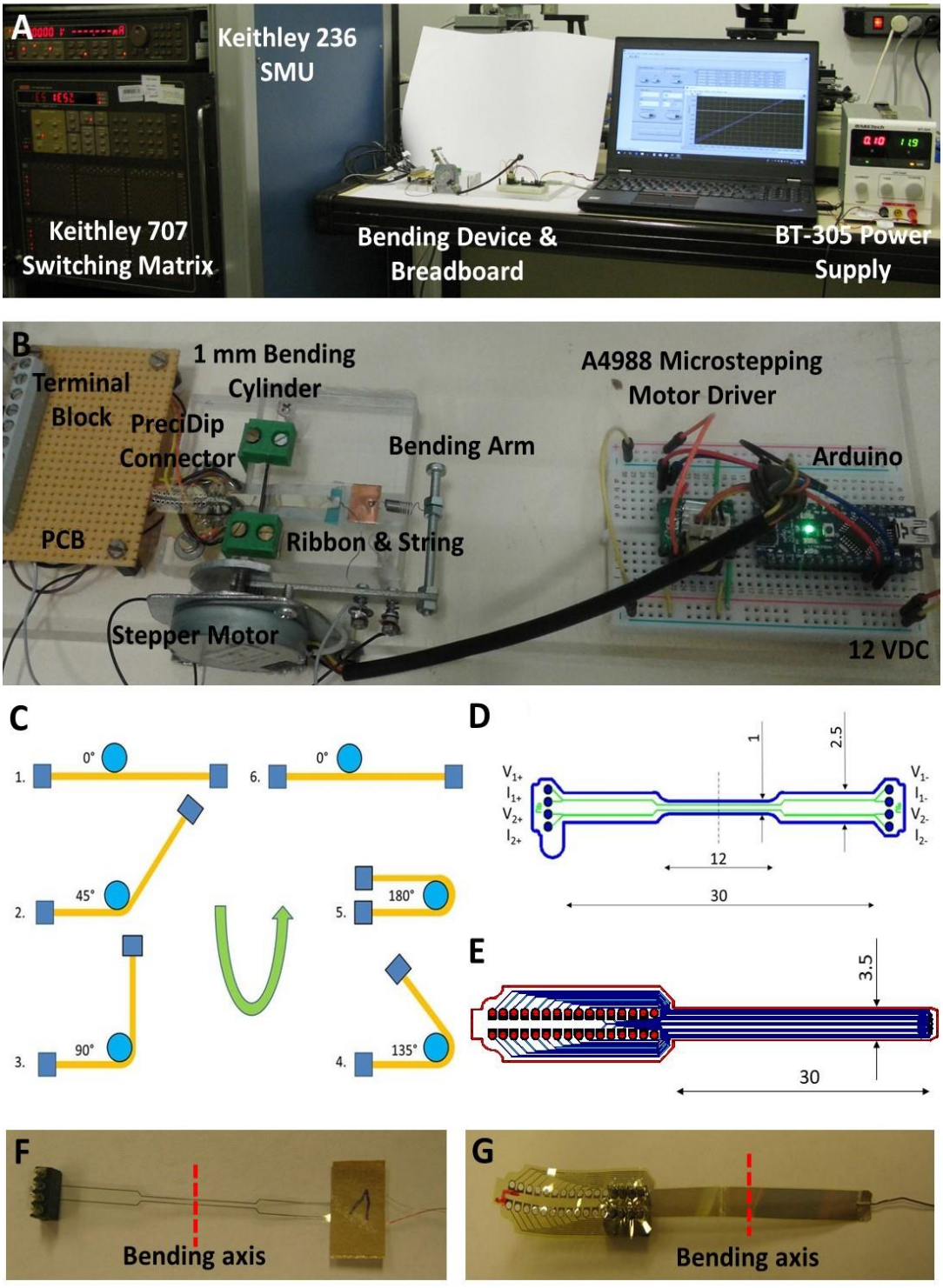

Figure 24. (a) Photograph of the complete measurement setup. (b) Assembly of custom-designed bending device.(c) Schematic describing the notations used for the evaluation of positions dependence during cyclic bending tests. (d & e) Dimensions in mm of Parylene (above) and polyimide (below) test samples. (f & g) Representative photo of Parylene (left) and polyimide (right) test samples for mechanical analysis.

The samples were firmly fixed on a frame, which translated the motion through a stepping motor and bent the middle of test samples around cylinder of 1 mm in diameter. Electrical resistance measurements were used to monitor the change in resistance at 0, 45, 90, 135 and 180 degree positions around the cylinder. Four-point resistance measuring technique was used to make more accurate measurements than the simpler two-wire sensing. Altogether, results on five samples were analyzed in a bending cycle of 100, 1000 and in one case 10,000.

4.2.5 *In vivo* experiments on polyimide based μECoG in IOSI

Electrophysiological recording and optical imaging of intrinsic signals were performed to map the layout of functional modules, so-called orientation domains, in the visual cortex of adult cats. Briefly, craniotomy and durotomy were made above the primary visual cortex, and a Teflon-chamber was implanted using bone screws and dental cement. The chamber was filled with artificial cerebrospinal fluid and covered with a glass plate to restore intracranial pressure. During IOSI, the cortex was illuminated with orange light (λ = 609 nm) using optic fibers and intrinsic signals were recorded with a CCD camera focused at a depth of 600-1000 μm below the cortical surface. Visual stimuli were generated using VSD Series 3 stimulus generator system (Cambridge Research System, Oxford, UK), placed at 28.5 cm in front of the cat's eye. Visual stimuli contained full field square wave luminance gratings with high contrast at eight equally spaced orientations. For visualizing signal intensity, imaging the functional architecture at various time-steps and to characterize the performance of intrinsic imaging through the μECoG electrode array, vascular images (green illumination) and orientation maps (2D color coded maps that are representing anatomical structure) were analyzed to detect the spatio-temporal patterns. Vascular image is a representation of the cortical surface illuminated with green light to emphasize the vasculature, while orientation preference map is an image representing the activity of different cortical columns evoked by visual stimulation with gratings projected at different angles. The cortical image is captured when the animal (eg. cat) viewed lines of a selected orientation and is subtracted from the average of the images captured when the animal viewed all the orientations or any control (eg. blank) images.

Recorded signals from 32 channels were amplified and digitalized with an Amplipex 256-channel multiplexed biosignal amplifier system (KJE-1001, Amplipex LTD*, Szeged, Hungary*) using a sampling rate of 20 kHz. An extra channel was used to record the visual stimulus synchronicity signal. The recorded local field potentials were preprocessed with a first-order bandpass Butterworth filter to observe activities in the frequency region of interest.

Detailed explanation of animal surgery, EEG recordings and data analysis, visual stimulation protocol and analysis of optical images are not subject of this thesis. More detailed description can be found in Zátonyi *et al*. [260].

4.3 Results and discussion

4.3.1 Optical evaluation

When combining surface μECoG devices with neural imaging techniques (eg. IOSI, two-photon imaging), substrate materials with highly compatible optical properties are desired. Polyimide shows transparency greater than 80 % above 530 - 540 nm, while the exhibited transparency for Parylene HT was greater than 90 % between 400 - 980 nm, presented in **Figure 25. (a & b)**. This implied that in case of IOSI recordings (illumination at 609 nm, detection between 540 - 900 nm) with polyimide – based (PI2611, HD MicroSystems GmbH) cortical devices, 30 – 35 % drop in signal intensity can be predicted.

When evaluating the functional compatibility of Parylene HT with two-photon imaging during electrophysiological experiments, the polymer has to show high transmittance in the wavelength range of both two-photon excitation and emission, also its auto-fluorescence should be as low as possible in order to not suppress the fluorescence signal of excited cells. For fluorimetric investigations, wavelength range between 260 – 600 nm was chosen to excite the polymer structures and the emitted fluorescence signals were collected between 270 – 800 nm. Results were evaluated and depicted (see in **Figure 25. (c)**) at excitation wavelength of 510 nm, near to the emission band of fluorescence protein calcium sensors (approx. 512 nm). During fluorimetric experiments, Parylene C samples with same thickness were applied as reference and frequently used material with comparable chemical structure.

Based on the obtained fluorescence and transmittance spectra, the optical transparency of Parylene HT is remarkably higher than that of polyimide, Polyethylene terephthalate (PET) [261], slightly higher than that of Parylene C and similar to that of SU-8 substrates [262] and Polydimethylsiloxane (PDMS) [263]. In comparison with Parylene C, the initial lower auto-fluorescence of Parylene HT film was attributed to the strength of C-F bond that is much higher than C-H bond. Parylene HT tends to be less sensitive to dehydrogenation, consequently the amount of C=C bonds, which are responsible for higher auto-fluorescence intensity, remains low under UV illumination [237].

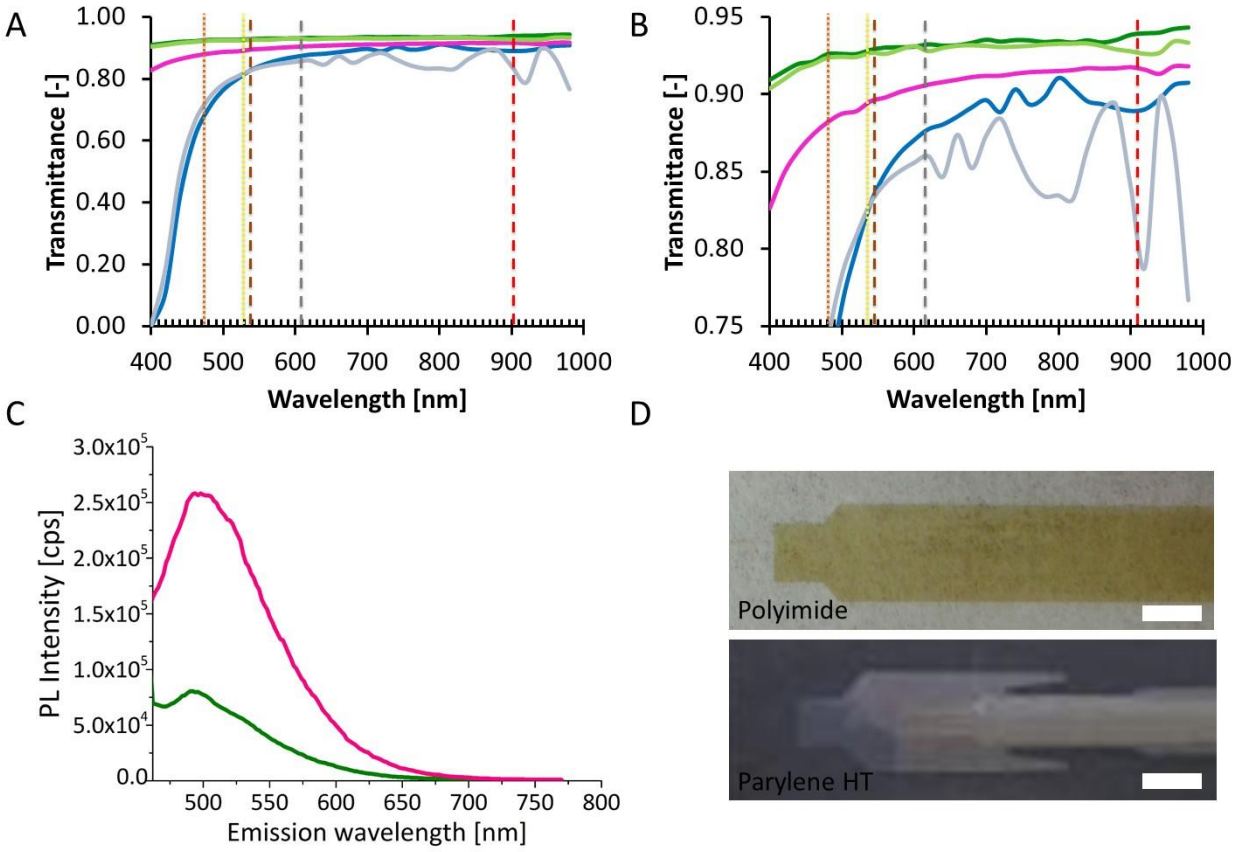

Figure 25. (a & b) Transmittance spectra of Parylene HT (dark green), Parylene HT/ITO (pale green), Parylene C (pink), polyimide (dark blue) and polyimide/ITO (pale blue) in the wavelength range between 400 and 980 nm. Vertical lines are denoting wavelengths important in neuroimaging. Dashed lines are representing wavelengths that are relevant in this work and dotted lines are representingn wavelengths that are not presented in this thesis but populars in neuroscience. IOSI detection from 540 nm (brown), IOSI illumination @ 609 nm (grey), 2P excitation @ 910 nm (red); optogenetics @ 475 nm (orange), Voltage-Sensitive Dye Imaging (VSDI) @ 530 nm (yellow). (c) Emission spectra of Parylene C (pink) and Parylene HT (green) at the excitation wavelength of 510 nm close to the emission wavelength of GCaMP6f (approx. 512 nm) relevant to evaluate autofluorescence behaviour. (d) Ready-to-use μECoG devices to visualize the difference between the transparency of the two substrate materials: polyimide (above) and Parylene HT (below) both with ITO conductive layer. Scale bar is 2 mm.

4.3.2 Electrochemical performance

Polyimide

Full spectra electrochemical impedance spectroscopy (EIS) data are plotted for a selected recording site out of 32, in Bode plots of impedance magnitude and phase angle versus frequency during the 16-days

of electrochemical stability experiment at day 1, day 8 and day 16 for polyimide/ITO/polyimide (**Figure 26. (a)**) with diameter of 300 μm and polyimide/Pt/polyimide (**Figure 26. (b)**) μECoG devices with diameter of 500 μm. Polyimide – based devices with platinum conductive traces were used as reference structures. Neither the characteristics of impedance curves, nor the characteristics of phase angle curves have changed significantly during the soaking experiment.

Average magnitude of impedance values of 32 recording sites, measured at 1 kHz versus soaking days can be seen in **Figure 26. (c & d)**. After an initial, significant drop, the impedance for both ITO and platinum based structures were stabilized after 5 soaking days. Impedance varied from 50.7 ± 4.3 kΩ (@ day 1) to 43.7 ± 4.3 kΩ (@ day 16) for ITO and between 6.7 ± 0.4 kΩ (@ day 1) and 6.2 ± 0.1 kΩ (@ day 16) for Pt recording sites (n = 32). Altogether, the initial impedance decreased by 13.8 % for ITO and 7.9 % for Pt devices by the end of the soaking experiment. The initial drop can be attributed to the activation of electrochemically inactive species after the first EIS measurement, where the cell was driven away from equilibrium for the first time by applying a small AC sine wave signal. During the first soaking day, ions from the electrolyte (K^+, Na^+, Cl^-, PO_3^-) could react activated species at the electrode's surface, therefore a new equilibrium was formed. This hypothesis was strengthened by equivalent circuit parameters. Regarding ITO coated electrodes, R_{CT} decreased, while W_D and Y increased after the first day, resulted in a lower magnitude of impedance. Variances in Z after the 5th soaking day, may be related to the refilling of the electrolyte solution due to unavoidable evaporation. Based on microscopic observation, mechanical damages like delamination, breakage or disruption of conductive films were avoided during the course of experiment.

Nyquist plots reveal the difference between the electrochemical responses and demonstrate the difference in the contribution of circuit elements to the response of electrodes made of ITO or Pt (**Figure 26. (e & f)**). For ITO, the conduction is free from Faradaic reactions, while platinum shows a pseudocapacitive electrochemical behaviour. In the case of recording electrodes used for neural purposes, current flow across the electrode-electrolyte interface is minimal [15], which criteria is fulfilled by both conductive materials.

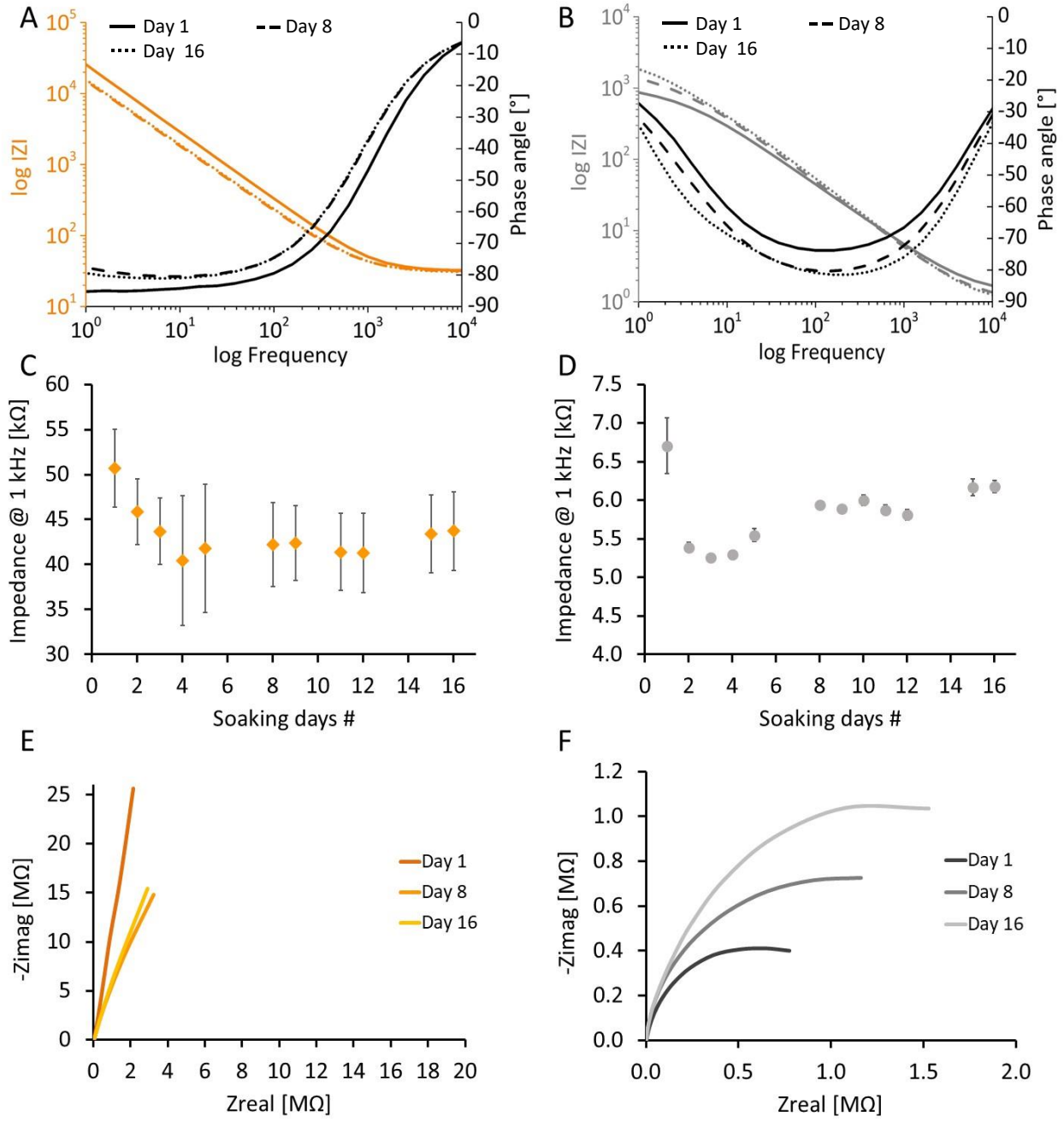

Figure 26. Evaluation of Bode plots represented by a selected ITO (a) or platinum (b) recording site during soaking experiment to test the long term stability of the so-called sandwich structures on polyimide substrates. Magnitude of impedance is represented by orange (ITO) or grey (Pt) lines at different stages of soaking experiment: day 1 (solid line), day 8 (dashed line), day 16 (dotted line). Phase angle is represented by black solid (day 1), dashed (day 8) and dotted (day 16) lines. Average impedance values of 32 recording sites, measured at 1 kHz, in a 16 day long soaking test for (c) ITO (orange rhombus) and (d) Pt (grey circle) electrodes. Magnitude of impedances are presented as Mean ± S.D. (n = 16 days). Nyquist plots of a selected recordign site out of 32 for (e) ITO (orange lines) and (f) Pt (gray lines) electrodes at soaking days of 1 (dark lines), 8 (beween dark & pale lines), and 16 (pale lines).

Parylene

Results of EIS data presented as Bode Plot are summarized in **Figure 27**. The 32-channel ECoG was constantly soaked in 0.01 M PBS at 67 °C for four experimental days, which means 24 simulated days of accelerated aging time based on **Equation 19**. ITO recording sites have a diameter of 150 μm. Impedance magnitude and phase angle of a representative μECoG array are plotted against frequency on the first day in **Figure 27. (a)**, during the whole time of the aging experiment in **Figure 27. (b),** and on the first and last day with fitted curves in **Figure 27. (c)**. Pale lines represent single recording sites, while thick lines represent the average values (n= 22 as other sites were non-functional because of the delamination of ITO during lift-off process or connection issues with Preci-Dip connector pins), see in **Figure 27. (a).** Impedance varied from 369 ± 42 kΩ to 345 ± 130 kΩ at 1 kHz in the aging experiment (**Figure 27. (c)**). Acceptance criteria was set to 500 kΩ @ 1 kHz (d = 150 μm), meanwhile recording sites were suspected to fail during soak testing when its impedance reached the upper limit of 1 MΩ.

Curve fitting and equivalent circuit analysis were applied to the measured data employing a common Randles circuit (**Figure 27. (d)**). The fitted spreading resistance (R_S), that is independent from the active surface area, remained in the same range (R_S = 0.3 MΩ) during the whole course of aging experiment. The charge transfer resistance (R_{CT}) did not change significantly, while the constant phase element (C_{CPE}) and its coefficient (α) slightly moved to a less perfect capacitive state (α = 1 for ideal capacitor; α = 0 for resistor). Decrease in α suggests a possible penetration of moisture through Parylene HT, resulted in a higher contact area on the electrode-electrolyte interface. Since the diffusion path length of the ions was short and higher, than 1 Hz was used, Warburg impedance (W_D) did not vary with time.

Besides the typical measurements at 1 kHz, I provide a more detailed analysis at five frequencies (10 kHz, 1 kHz, 100 Hz, 10 Hz and 1 Hz), shown in **Figure 27**. **(e & f)**. EIS showed a slight decrease in impedance magnitude between 1 Hz to 10 kHz with higher standard deviation at lower frequencies, since EIS recording is less certain and reliable at lower frequencies. The phase angle increased at all frequencies except at 1 Hz, where the highest standard deviation was observed. Systematic variation in the impedance magnitude and the phase angle at all frequencies reveals a less dominant capacitive behaviour of electrochemical performance than on the first day of ageing test. Since Parylene HT exhibits the lowest permeability to moisture, fluids and gases (< 0.01 % water absorption after 24 hours, based on its datasheet [236]) the changes occurred at the ITO/Parylene HT material interface, where adhesion forces are less powerful and therefore an additional adhesion promoting agent was also used.

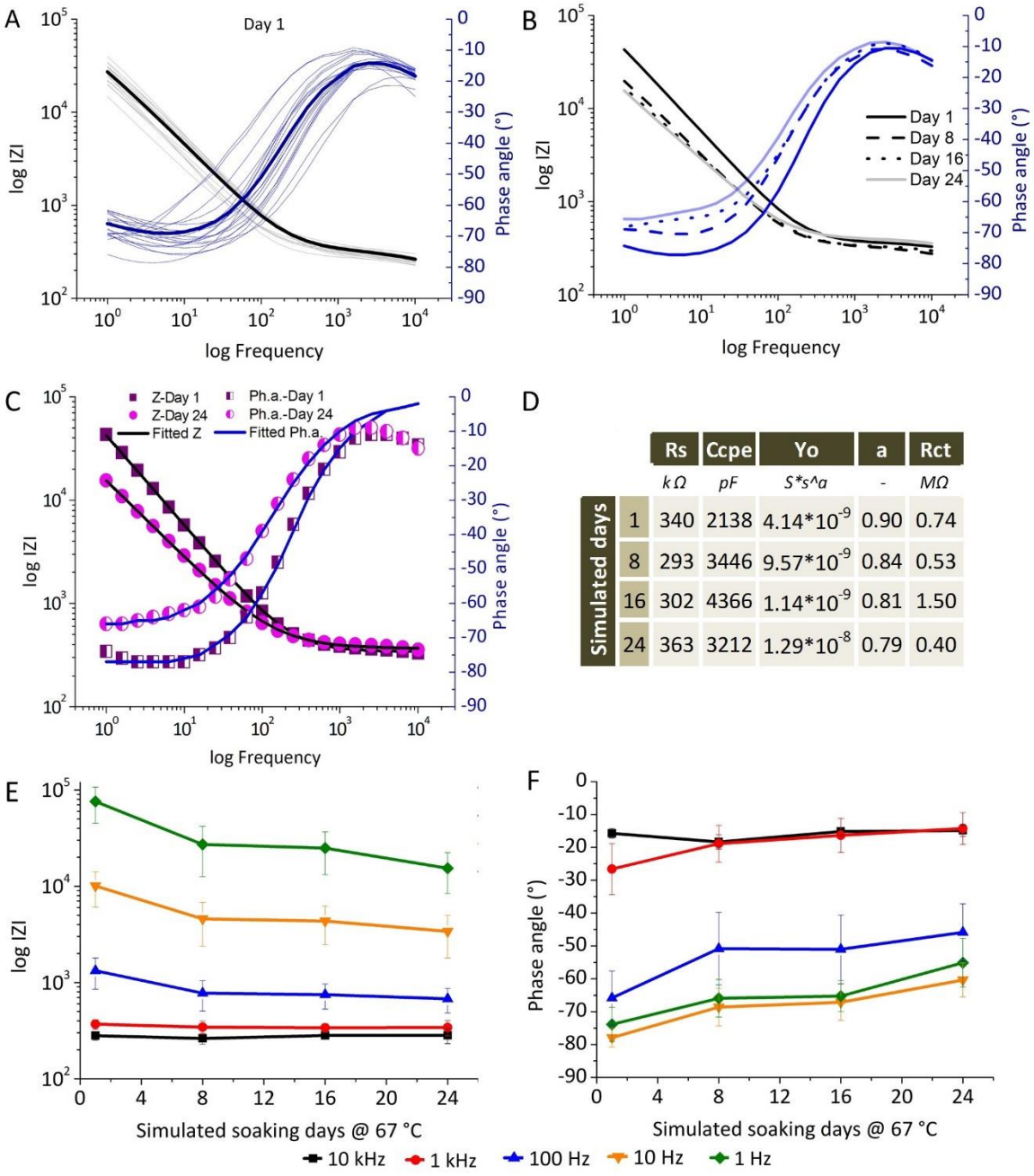

Simulated days	Rs (kΩ)	Ccpe (pF)	Yo (S*s^a)	a (-)	Rct (MΩ)
1	340	2138	$4.14*10^{-9}$	0.90	0.74
8	293	3446	$9.57*10^{-9}$	0.84	0.53
16	302	4366	$1.14*10^{-9}$	0.81	1.50
24	363	3212	$1.29*10^{-8}$	0.79	0.40

Figure 27. (a) Impedance magnitude and phase angle of 22 recording sites at the first day of the experiment, measured in 0.01 M PBS at 67 °C. Pale grey lines represent the Z magnitude of single recording sites, the black is the average of all sites; pale blue lines represent the phase angle characteristics of single recording sites, dark blue line is the average of all sites. (b) Representative Bode plot of a selected channel (black-Z, blue-Phase angle) on the first four days of the accelerated aging experiment (which means 1, 8, 16 and 24 simulated days) (c). Representative Bode plot and the relevant fitted curves of a selected channel on the first and simulated 24 days (at 67°C) of the experiment. (Full squares: Z values on the first day, full circles: Z values on the 24 day; half square: Phase angle on the first day, half circle: Phase angle on the 24 day; continuous black lines: fitted Z curves, continuous blue lines: fitted Phase curves). (d) Fitted equivalent circuit parameters during the accelerated aging experiment (RS: resistance of the bulk electrolyte, CCPE: constant phase element modeling with Y0 coefficient and α, RCT: charge transfer resistance). Average 10 kHz (black square), 1 kHz (red circle), 100 Hz (blue triangle), 10 Hz (orange triangle), 1 Hz (green rhombus) impedances (e) and phase angles (f) of 22 sites at 67°C. Data is presented as mean values ± standard deviation.

4.3.3 Tolerance to cyclic bending loads

ITO deposited on different polymer substrates (polyimide and Parylene HT) was in the focus of mechanical stability experiments as this metal – oxide had been considered as brittle material in previous publications [208], [209], [212], [264], thus, inconvenient for flexible neural interfaces. Mechanical stability of the proposed multilayer has to be tested by mimicking harsh conditions of handling during surgical procedures that may deteriorate the electrode functionality due to the bending and conformation on curved brain surfaces [265].

Cyclic bending test was applied and change in wire resistance was measured using polyimide/ITO/polyimide, compared with polyimide/Pt/polyimide and Parylene HT/ITO/Parylene HT, compared with Parylene C/Au/Parylene C test structures (see **Figure 24. (d – g)).** Resistance was measured at bending angles of 0°, 45°, 90°, 135°, 180° and results are presented for in **Figure 28**. & **Figure 29**. To enhance the tolerance of ITO to bending loads, metal – oxide layers were formed in the neutral axis of the thin film stack that was proven to be efficient when using fragile materials [45]. Results of bending tests presented in this thesis confirmed that the proposed material composition can withstand the load through more than 1000 cycles, which is definitely enough to prove electrical stability to external mechanical impacts during surgical procedures.

Polyimide

Variation in resistance at bending angles of 0°and 180°during 100 cycles for five samples was compared, designed with ITO (**Figure 28. (a)**) or platinum (**Figure 28. (b)**) conductive layer. Resistance varied between 65 – 75 kΩ and 372 – 380 Ω for all ITO and Pt samples, respectively. The difference in resistance (ΔR) of a selected channel between the first and the last bending cycles (100 or 1000 cycles), remained below 3 % ± S.D. for ITO (**Figure 28. (c)**) and 0.03 % ± S.D. for Pt (**Figure 28. (d)**) electrodes considering every bending angles of 0°, 45°, 90°, 135°, 180°. Variation in resistance of a selected channel can be seen in **Figure 28. (e & f)** during 1000 (ITO and Pt) and 10,000 (Pt) bending cycles at 0°and 180° angles. Considering ITO, resistance varied between 65 – 71 kΩ independently from the bending angle (see **Figure 28. (e)**). For Pt samples, resistance stays within 1 Ω for a selected channel and the variation did not rise above 1 Ω after 10,000 bending cycles as well (see **Figure 28. (f)**).

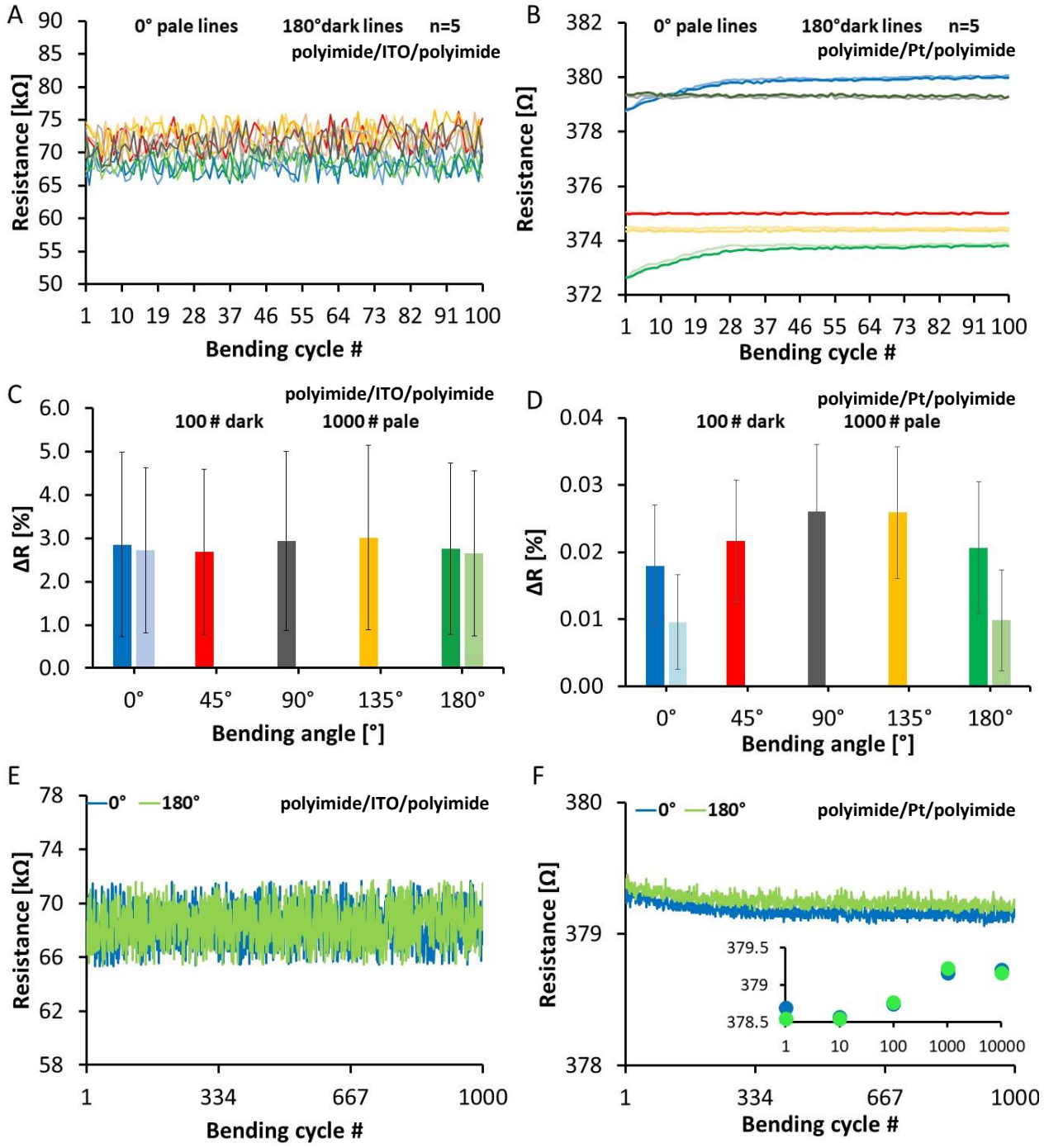

Figure 28. Tolerance to cyclic bending loads on polyimide/ITO/polyimide (a, c, e) and on polyimide/Pt/polyimide structures (b, d, f). (a & b) Resistance measured during 100 bending cycles at bending agle of 0° (pale lines) and 180° (dark lines), test on five individual samples. (c & d) Change in resistance (ΔR) of samples at various bending angle (blue – 0°, red - 45°, grey – 90°, yellow – 135°, green – 180°) during the course of cyclic load (dark columns – 100 , pale columns – 1000 #). (e & f) Resistance plotted against cycle number (1000 #) during the course of bending test on a selected sample at bending angle of 0° (blue line) and 180° (green line). The inset shows variation in resistance during 10,000 bending cycles on a polyimide/Pt/polyimide sample.

Parylene HT

The comparison of resistance measured at bending positions of 0° and 180° is presented in **Figure 29. (a)** for Parylene HT/ITO/Parylene HT on five channels and **Figure 29**. **(b)** for Parylene C/gold/Parylene C on two channels during 100 bending cycles. Resistance varied between 118 – 132 kΩ and 74 – 77 Ω for ITO and Au samples, respectively. Although the thickness of ITO was 100 nm equally in every sample, the variation in resistance comparing polyimide and Parylene HT-based samples, arise from the difference in nanoscale surface morphology and different deposition technology of the two polymer substrates. Change in resistance (ΔR) at various positions are below 1 % (**Figure 29. (c)**) for ITO and below 0.02 % ± S.D. (**Figure 29. (d)**) for Au samples, which proves the mechanical stability of the created structures. Variation in resistance of a selected channel can be seen in **Figure 29. (e & f)** during 1000 (ITO and Au) and more than 1000 (Au) bending cycles later, because extreme increase in resistance was measured with gold channels. Considering ITO resistance varied between 137 - 140 kΩ independently from the bending angle (see **Figure 29. (e)**). For Au samples, failure of the traces was strated when the resistance increased above 145 Ω after 1217 cycles, and reached maximum 5100 Ω, then the negative value was measured at first after 1260 bending cycles, which indicated the failure of the gold traces due to breaking (see **Figure 29. (f)**). Based on visual investigation, the connection points were stable, therefore this phenomenon can be attributed to the weak adhesion of gold to Parylene C that plays an important role in the stability of multilayer structures under mechanical loads. In spite of the observations on Parylene C/gold structures neither adhesion issues, nor resistance changes arise from the brittleness of ITO were explored after 1000 bending cycles on Parylene HT and polyimide samples as well. Cyclic mechanical tests confirmed that ITO forms a reliable conductive layer encapsulated in polyimide or Parylene HT and is not prone to failure when exposed to bending.

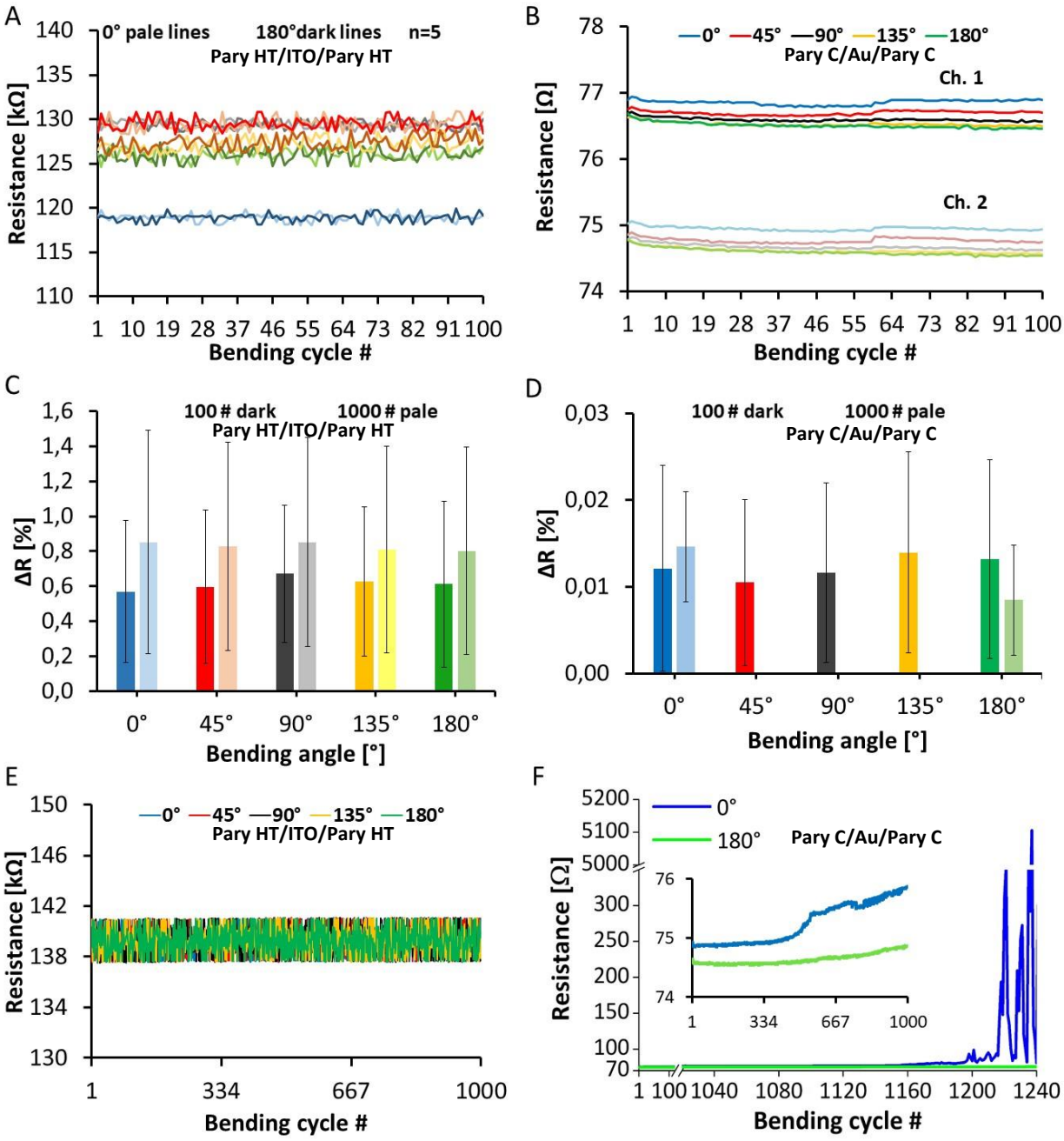

Figure 29. Tolerance to cyclic bending loads on Parylene HT/ITO/Parylene HT (a, c, e) and on Parylene C/Au/Parylene C structures (b, d, f). (a & b) Resistance measured during 100 bending cycles at bending agle of 0° (pale lines) and 180° (dark lines), test on five (a) and two (b) individual samples. (c & d) Change in resistance (ΔR) of samples at various bending angle (blue – 0°, red - 45°, grey – 90°, yellow – 135°, green – 180°) during the course of cyclic load (dark columns – 100 , pale columns – 1000 #). (e & f) Resistance plotted against cycle number (1000 #) during the course of bending test on a selected sample at bending angle of 0°, 45°, 90°, 180° (e) and 0°, 180° (f). The inset shows the failure (started from 1160th cycle) and finally disruption (at 1220th cycle) of conductive layer (Au), measured at 0°.

4.3.4 Performance of polyimide – based μECoG during *in vivo* experiments

To characterize the *in vivo* performance of polyimide – based μECoG electrodes vascular images (green light illumination) and orientation preference maps were compared in two cases, when the exposed region of cat visual cortex (A18) was covered or uncovered with a μECoG electrode. In the first case, the μECoG electrode was positioned precisely in the light path. On orientation preference maps, each color marking a group or column of neurons that are responding selectively to a particular orientation in space (red - 0° or horizontal lines, yellow - 45° or lines diagonally down from upper-left corner, green - 90° or vertical lines, blue - 135° or lines diagonally up from lower-left corner). Iso-orientation patches are organized radially in a pinwheel-like fashion or around so-called orientation centers (pinwheels) [266], [267] and are formed by neurons involved in the perception of patterns.

For comparing optical imaging data obtained with (covered) and without μECoG electrode (intact), these pinwheels were identified on the orientation maps and on the corresponding vascular images, and labeled with numbered white and black circles. Each number refers to the position of the same pinwheel. The positions of recording sites are marked with red dots in each image. It should be noted that the vascular arrangement was slightly different, which is physiologically normal, but may also be caused partially by the implantation procedure of the electrode positioned underneath the cut edges of the dura mater. Since the cranial chamber is pressurized, the slight changes in the index of refraction do not induce significant shift in the angular information due to the relatively flat cortical tissue. Based on these results, we concluded the determination of orientation preference in the visual cortex is feasible through the transparent electrode array within reasonably large field of view (4.7 mm x 1.5 mm).

Broadband and narrowband gamma activity (approx. 50 – 100 Hz) is considered as optical stimulus dependent frequency band [268]–[271], however the neurophysiological processes behind are still debated. The electrophysiological data recorded from the anaesthetized cats showed constant spectral activity in the lower frequency ranges until 40 Hz. Above that, only temporarily noticeable activity was recorded, represented by sharp peaks, that connected solely to the visual stimuli at a very narrow frequency band between 78 - 82 Hz. The lack of this response was observed, when a blank screen was presented. Considering the simultaneously recorded optical (hemodynamic changes) and electrophysiological data (changes in cortical gamma band activity), we can conclude that power map of narrowband gamma signals recorded by our device is dependent on stimulus patterns, and shows similarities to the orientation angle map obtained from single stimulus conditions. Results of IOSI are

summarized in **Figure 30**. More detailed electrophysiological and optical analysis is provided in Zátonyi *et al.* [260].

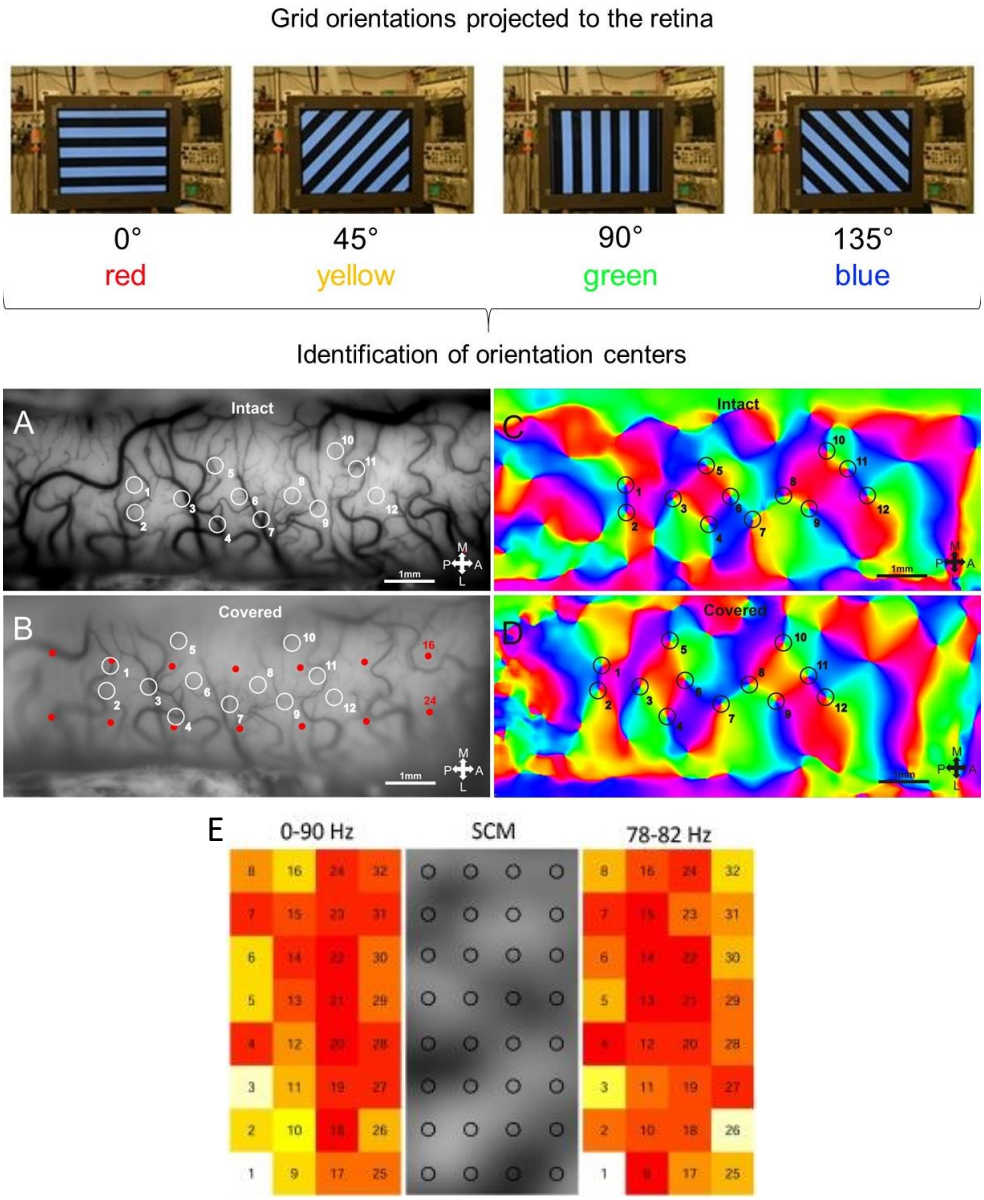

Figure 30. Upper image: representation of different grid orientations projected to cat's retina. Bottom image: Identification of orientation centers. Vascular images of the exposed region of cat visual cortex A18 uncovered (a) and covered with a μECoG electrode (b). Orientation maps in each case are represented by (c) and (d). White and black circles with numbers and red dots show pinwheels and recording site positions of the electrode, respectively. Each numbered circle refers to the position of the same pinwheel on each picture. Panel (e) is composed of individual angle maps (in grayscale) belonging to 0°, and power distribution maps belonging to the same stimuli. The power distribution was calculated from the first 4 seconds of the averaged waveforms belonging to the given type of stimuli in two frequency band: wideband (0 – 90 Hz: most likely dominated by lower frequency range – Left) and a narrowband filtered waveform average (78 - 82 Hz – Right). The numbering of the channels is shown on the power maps. The scaling for the power maps are always normalized to maximize the visibility of the spatial pattern of power distribution. Channel 1 is white because it was not working properly and it was excluded from the calculation.

4.3.5 Our results in comparison with other polymer materials for neural interfaces

Since the scope of my work was to fabricate and investigate material properties of a transparent, mechanically robust and durable μECoG array that can be used concurrent neural imaging and electrophysiology recording, the best polymer material was selected that satisfies all these rigorous requirements. ITO was selected to serve as conductive grade in multimodal applications. It has to be considered that ITO is a brittle thin film material, we enhanced tolerance to bending loads by forming the conductive layer in the neutral axis of the thin film stack [45], which is especially complicated e.g. in the case of ITO coated Polyethylene terephthalate (PET) substrates. Unlike Polydimethylsiloxane (PDMS), Parylene HT has lower gas permeability that resulted in longer lifetime and reliable recording ability during chronic implantations. Adhesion promoters are recommended when fabricating neural interfaces from SU-8 or Parylene C [272] polymer materials, in the former case partly because of its susceptibility to water absorption [273]. Precise comparison of relevant material properties of various polymer substrates used for neural interfaces can be seen in **Table 6**.

Table 6. Comparison of different polymer substrates used for neural interfacing (recommended, tested (+++); suitable (++); uncertain, questionable (+); inappropriate (-)).

	Parylene HT	*Parylene C*	*PI (PI 2611)*	*SU-8*	*PET*	*PDMS*
Batch fabrication	*+++ (based on our result)*	*+++ (based on our result)*	*+++ (based on our results)* [260]	*+++* [117]	*+* [214]	*+++* [274]
Water absorption	*<0.01%* [236]	*<0.1%* [236]	*0.5%* [275]	*0.55%* [273]	*highly variable but tend to hydrolytic decomposition*	*>0.5%* [276]
Tensile strength	*52 MPa* [236]	*69 MPa* [236]	*350 MPa* [277]	*73 MPa* [273]	*50-80 MPa* [278], [279]	*3.9 MPa* [276]
Young's modulus	*2.6 GPa* [236]	*2.76 GPa* [236]	*8.5 GPa* [277]	*2.0 GPa* [273]	*2-4 GPa* [279]	*0.36-0.87 MPa* [280]
Transmittance	*> 90 % at 400–900 nm (with ITO) (based on our result)*	*slightly lower, than Parylene HT*	*≥80% at 530-980 nm (with ITO) (based on our results)* [260]	*>90%@> 500 nm* [273]	*>80% at 480 – 680nm (with ITO)* [214]	*<80% at 480 - 700nm (with ITO-PET layers)* [281]
Autofluorescence	*better performance than other poly(para-xylylenes)* [237]	*worse performance than Parylene HT*	*worse perform. than poly(p-xylylenes) (based on our res)* [237]	*incomparable when the instrumentation, thickness, material compositions, measurement parameters etc. are different*		
Compatibility with microfab.	*+++ (based on our result)*	*+/++ (adhesion*	*+++ (based on our and other*	*+++* [282]	*++* [214]	*+++* [274]

processes		*issues)*	*results)* [196], [260]			
ITO in neutral axis	*+++ (based on our result)*	*+, because of adhesion issues*	*+++ (based on or results)* [260]	*not presented but feasible*	– [214]	*+++* [274]

4.4 Conclusion and future concept

In case of Intrinsic Optical Signal Imaging (IOSI), polyimide was selected and characterized as substrate material. In comparison ITO – coated PET substrates used in similar application (Voltage – Sensitive Dye Imaging - VSD) provides the same order of magnitude in transparency [214] and artificial dura mater materials made of silicone [283], propose slightly higher light transmission. Reconstruction of the functional domains through this transparent array was possible using 609 nm illumination of the exposed cortical surface. During the surgical procedure, positioning them into the cranial chamber and fixing them underneath the dura mater likely cause failures in the case of various material compositions. In our approach, we took the advantage of polyimide's superior tensile strength (350 MPa) that visibly ensured durability of the device during surgical procedures. As far as I know, this is the first *in vivo* demonstration of a polyimide - based μECoG array, used for the simultaneous detection of intrinsic optical signals in conjunction with intracranial EEG.

In case of two-photon imaging, Parylene HT was selected and characterized as biocompatible substrate and encapsulation material. Combination of ITO with Parylene HT is not common, however our results proved that it has several advantages by improving the useful area for neuroimaging through our transparent μECoG device that was prior limited to the close vicinity of the recording sites made of transparent materials eg. graphene [284] or bilayer – nanomesh structures [39].

The fabrication scheme of our devices is based on simple MEMS processes, therefore provides cost-effective, straightforward and reliably reproducible technology. Other approaches relying on stacking of graphene monolayers require complicated steps, which deteriorates uniformity and process reproducibility. Our approach requires simple instrumentation in the clean room facility, as spin-coater and hot plate in contrast to the expensive CVD equipment used for Parylene deposition. Besides, the primary material of polyimide (viscous solution in primary form) is less expensive, commercially available.

In the future, chronic *in vivo* experiments are being planned to test the long term reliability and stability of the recording and imaging quality.

Thesis statement related to this chapter

I designed and developed flexible, transparent μECoG devices to demonstrate concurrent neural imaging and intracranial EEG recording. I utilized polyimide / ITO / polyimide layer structure to fabricate μECoG interface for concurrent intrinsic optical signal imaging and electrophysiological recording, and Parylene HT / ITO / Parylene HT layer structure to form μECoG interface for concurrent two – photon imaging and electrophysiological recording. Based on optical measurements, I proved the superb optical performance of Parylene HT, transmittance of Parylene HT is 2.4 % higher at the wavelength range of 900 – 920 nm, and photoluminescence intensity of Parylene C was 3.6 % higher at the maximum of emission spectral distribution at 510 nm excitation wavelength. I demonstrated the electrochemical stability of μECoG devices. The impedance values remained below 100 kΩ at 1 kHz with electrode diameter of 300 μm and below 500 kΩ at 1 kHz with electrode diameter of 150 μm. I demonstrated the mechanical durability of the proposed material compositions to cyclic bending loads, up to 1000 cycles. Change in resistance (ΔR) at various bending positions are below 1 % for ITO electrodes. I contribute to in vivo validation of transparent microprobes in concurrent neuroimaging and electrophysiological experiments, where multimodal functionality of μECoG devices have been proven.

Scientific papers related to this thesis statement

A. Zátonyi *et al.*, Functional brain mapping using optical imaging of intrinsic signals and simultaneous high-resolution cortical electrophysiology with a flexible, transparent microelectrode array, *Sensors & Actuators B-Chemical*, 273, 519-526, **2018**

A. Zátonyi *et al.*, "Transparent, low-autofluorescence microECoG device for simultaneous Ca2+ imaging and cortical electrophysiology *in vivo*.," *J. Neural Eng.*, Dec. **2019.**

5 BIBLIOGRAPHY

[1] "Principles of Neural Science, Fifth Edition | AccessNeurology | McGraw-Hill Medical." [Online]. Available: https://neurology.mhmedical.com/book.aspx?bookID=1049. [Accessed: 08-Jan-2020].

[2] A. L. Hodgkin, "Evidence for electrical transmission in nerve," *J. Physiol.*, vol. 90, no. 2, pp. 183–210, Jul. 1937.

[3] A. L. Hodgkin and A. F. Huxley, "Resting and action potentials in single nerve fibres," *J. Physiol.*, vol. 104, no. 2, pp. 176–195, Oct. 1945.

[4] A. L. Hodgkin and A. F. Huxley, "A quantitative description of membrane current and its application to conduction and excitation in nerve," *Bull. Math. Biol.*, vol. 52, no. 1–2, pp. 25–71, Jan. 1990.

[5] H. Lodish, A. Berk, S. L. Zipursky, P. Matsudaira, D. Baltimore, and J. Darnell, "The Action Potential and Conduction of Electric Impulses," 2000.

[6] "Topic 6.5: Neurones and Synapses - AMAZING WORLD OF SCIENCE WITH MR. GREEN." [Online]. Available: https://www.mrgscience.com/topic-65-neurones-and-synapses.html. [Accessed: 08-Jan-2020].

[7] "Chapter 7." [Online]. Available: http://droualb.faculty.mjc.edu/Course Materials/Physiology 101/Chapter Notes/Fall 2011/chapter_7 Fall 2011.htm. [Accessed: 07-Jan-2020].

[8] S. B. Baumann, D. R. Wozny, S. K. Kelly, and F. M. Meno, "The electrical conductivity of human cerebrospinal fluid at body temperature," *IEEE Trans. Biomed. Eng.*, vol. 44, no. 3, pp. 220–223, 1997.

[9] Y. Kajikawa and C. E. Schroeder, "Generation of field potentials and modulation of their dynamics through volume integration of cortical activity," *J. Neurophysiol.*, vol. 113, no. 1, pp. 339–351, Jan. 2015.

[10] S. Perel *et al.*, "Single-unit activity, threshold crossings, and local field potentials in motor cortex differentially encode reach kinematics," *J. Neurophysiol.*, vol. 114, no. 3, pp. 1500–1512, Sep. 2015.

[11] G. Buzsáki, C. A. Anastassiou, and C. Koch, "The origin of extracellular fields and currents-EEG, ECoG, LFP and spikes," *Nat. Rev. Neurosci.*, vol. 13, no. 6, pp. 407–420, 2012.

[12] H. Petsche, H. Pockberger, and P. Rappelsberger, "On the search for the sources of the electroencephalogram," *Neuroscience*, vol. 11, no. 1, pp. 1–27, 1984.

[13] D. Khodagholy *et al.*, "NeuroGrid: recording action potentials from the surface of the brain," *Nat. Neurosci.*, vol. 18, no. 2, pp. 310–315, 2014.

[14] W. Franks, I. Schenker, P. Schmutz, and A. Hierlemann, "Impedance Characterization and Modelling of Electrodes for Biomedical Applications," *IEEE Trans. Biomed. Eng.*, vol. 52, no. 7, pp. 1295–1302, 2005.

[15] S. F. Cogan, “Neural Stimulation and Recording Electrodes,” *Annu. Rev. Biomed. Eng.*, vol. 10, no. 1, pp. 275–309, Aug. 2008.

[16] P. L. Bégin and E. Kaminska, “Thermal accelerated ageing test method development,” *Restaurator*, vol. 23, no. 2, pp. 89–105, 2002.

[17] D. W. L. Hukins, A. Mahomed, and S. N. Kukureka, “Accelerated aging for testing polymeric biomaterials and medical devices,” *Med. Eng. Phys.*, vol. 30, no. 10, pp. 1270–1274, 2008.

[18] S. M. Devices, “ASTM F1980-16 Standard Guide for Accelerated Aging of Sterile Barrier Systems for Medical Devices,” vol. 07, no. 2011, pp. 1–7, 2017.

[19] A. Allagui, T. J. Freeborn, A. S. Elwakil, and B. J. Maundy, “Reevaluation of Performance of Electric Double-layer Capacitors from Constant-current Charge/Discharge and Cyclic Voltammetry,” *Sci. Rep.*, vol. 6, no. 1, p. 38568, Dec. 2016.

[20] N. A. Alba, Z. J. Du, K. A. Catt, T. D. Y. Kozai, and X. T. Cui, “In vivo electrochemical analysis of a PEDOT/MWCNT neural electrode coating,” *Biosensors*, vol. 5, no. 4, pp. 618–646, 2015.

[21] J. B. Jorcin, M. E. Orazem, N. Pébère, and B. Tribollet, “CPE analysis by local electrochemical impedance spectroscopy,” *Electrochim. Acta*, vol. 51, no. 8–9, pp. 1473–1479, 2006.

[22] J. P. Neto *et al.*, “Does impedance matter when recording spikes with polytrodes?,” *Front. Neurosci.*, vol. 12, no. OCT, Oct. 2018.

[23] J. E. Ferguson, C. Boldt, and A. D. Redish, “Low-impedance tetrode plating procedure,” no. 1, pp. 1–2, 2009.

[24] S. F. Lempka, M. D. Johnson, M. A. Moffitt, K. J. Otto, D. R. Kipke, and C. C. McIntyre, “Theoretical analysis of intracortical microelectrode recordings,” *J. Neural Eng.*, vol. 8, no. 4, p. 045006, 2011.

[25] S. F. Lempka *et al.*, “Optimization of Microelectrode Design for Cortical Recording Based on Thermal Noise Considerations,” *Annu. Int. Conf. IEEE Eng. Med. Biol. - Proc.*, pp. 3361–3364, 2006.

[26] M. Vomero *et al.*, “Highly Stable Glassy Carbon Interfaces for Long-Term Neural Stimulation and Low-Noise Recording of Brain Activity,” *Sci. Rep.*, vol. 7, p. 40332, Jan. 2017.

[27] J. M. Doña Rodríguez, J. a. Herrera Melián, and J. Pérez Peña, “Determination of the Real Surface Area of Pt Electrodes by Hydrogen Adsorption Using Cyclic Voltammetry,” *J. Chem. Educ.*, vol. 77, no. 9, p. 1195, 2000.

[28] M. Antioxidant, “Cyclic voltammetry,” no. d, pp. 1–9, 2016.

[29] G. Márton, I. Bakos, Z. Fekete, I. Ulbert, and A. Pongrácz, “Durability of high surface area platinum deposits on microelectrode arrays for acute neural recordings,” *J. Mater. Sci. Mater. Med.*, vol. 25, no. 3, pp. 931–940, 2014.

[30] A. Kloke, F. Von Stetten, R. Zengerle, and S. Kerzenmacher, “Strategies for the fabrication of porous platinum electrodes,” *Adv. Mater.*, vol. 23, no. 43, pp. 4976–5008, 2011.

[31] N. Silpa, “Nanostructured Sensors for in- Vivo Neurochemical Recording,” 2007.

[32] V. Castagnola, “Implantable microelectrodes on soft substrate with nanostructured surface for stimulation and recording of brain activities,” no. September, 2014.

[33] D. Khodagholy *et al.*, “In vivo recordings of brain activity using organic transistors,” *Nat. Commun.*, vol. 4, 2013.

[34] T. D. Y. Kozai *et al.*, “Chronic In Vivo evaluation of PEDOT/CNT for stable neural recordings,” *IEEE Trans. Biomed. Eng.*, vol. 63, no. 1, pp. 111–119, 2016.

[35] S. J. Wilks, S. M. Richardson-Burns, J. L. Hendricks, D. C. Martin, and K. J. Otto, “Poly(3,4-ethylenedioxythiophene) as a micro-neural interface material for electrostimulation,” *Front. Neuroeng.*, vol. 2, no. JUN, Jun. 2009.

[36] X. T. Cui and D. D. Zhou, “Poly (3,4-ethylenedioxythiophene) for chronic neural stimulation,” *IEEE Trans. Neural Syst. Rehabil. Eng.*, vol. 15, no. 4, pp. 502–508, Dec. 2007.

[37] K. A. Ludwig, J. D. Uram, J. Yang, D. C. Martin, and D. R. Kipke, “Chronic neural recordings using silicon microelectrode arrays electrochemically deposited with a poly(3,4-ethylenedioxythiophene) (PEDOT) film,” *J. Neural Eng.*, vol. 3, no. 1, pp. 59–70, Mar. 2006.

[38] Y. Qiang *et al.*, “Bilayer Nanomesh Structures for Transparent Recording and Stimulating Microelectrodes,” *Adv. Funct. Mater.*, vol. 27, no. 48, pp. 1–11, 2017.

[39] Y. Qiang *et al.*, “Transparent arrays of bilayer-nanomesh microelectrodes for simultaneous electrophysiology and two-photon imaging in the brain,” *Sci. Adv.*, vol. 4, no. 9, p. eaat0626, 2018.

[40] S. P. Zankowski and P. M. Vereecken, “Electrochemical determination of porosity and surface area of thin films of interconnected nickel nanowires,” *J. Electrochem. Soc.*, vol. 166, no. 6, pp. D227–D235, 2019.

[41] A. M. Feltham and M. Spiro, “Platinized platinum electrodes,” *Chem. Rev.*, vol. 71, no. 2, pp. 177–193, 1971.

[42] J. L. (Jimmy L. Davidson, Electrochemical Society., Electrochemical Society. Sensor Division., Electrochemical Society. Dielectric Science and Technology Division., Electrochemical Society. Electronics Division., and H. Electrochemical Society. Meeting (206th : 2004 : Honolulu, *Microfabricated Systems and MEMS VII : proceedings of the international symposium*. Electrochemical Society, 2004.

[43] M. Schuettler, D. Pfau, J. S. Ordonez, C. Henle, P. Woias, and T. Stieglitz, “Stretchable tracks for laser-machined neural electrode arrays,” *Proc. 31st Annu. Int. Conf. IEEE Eng. Med. Biol. Soc. Eng. Futur. Biomed. EMBC 2009*, pp. 1612–1615, 2009.

[44] F. Kohler, R. Michiels, M. Schuettler, and T. Stieglitz, “Development of a bending test procedure for the characterization of flexible ECoG electrode arrays,” *Curr. Dir. Biomed. Eng.*, vol. 1, no. 1, Sep. 2015.

[45] S. Lee *et al.*, “Bendability optimization of flexible optical nanoelectronics via neutral axis engineering,” *Nanoscale Res. Lett.*, vol. 7, pp. 1–18, 2012.

[46] W. Wang *et al.*, “Neural Interface Technology for Rehabilitation: Exploiting and Promoting

Neuroplasticity," *Phys. Med. Rehabil. Clin. N. Am.*, vol. 21, no. 1, pp. 157–178, 2010.

[47] E. C. Leuthardt, G. Schalk, J. R. Wolpaw, J. G. Ojemann, and D. W. Moran, "A brain-computer interface using electrocorticographic signals in humans," *J. Neural Eng.*, vol. 1, no. 2, pp. 63–71, Jun. 2004.

[48] K. M. Szostak, L. Grand, and T. G. Constandinou, "Neural interfaces for intracortical recording: Requirements, fabrication methods, and characteristics," *Frontiers in Neuroscience*, vol. 11, no. DEC. Frontiers Media S.A., 07-Dec-2017.

[49] C. Kim, J. Jeong, and S. J. Kim, "Recent progress on non-conventional microfabricated probes for the chronic recording of cortical neural activity," *Sensors (Switzerland)*, vol. 19, no. 5. MDPI AG, 01-Mar-2019.

[50] P. K. Campbell, K. E. Jones, R. J. Huber, K. W. Horch, and R. A. Normann, "A Silicon-Based, Three-Dimensional Neural Interface: Manufacturing Processes for an Intracortical Electrode Array," *IEEE Trans. Biomed. Eng.*, vol. 38, no. 8, pp. 758–768, 1991.

[51] A. Branner, R. B. Stein, E. Fernandez, Y. Aoyagi, and R. A. Normann, "Long-Term Stimulation and Recording with a Penetrating Microelectrode Array in Cat Sciatic Nerve," *IEEE Trans. Biomed. Eng.*, vol. 51, no. 1, pp. 146–157, Jan. 2004.

[52] N. Obidin, F. Tasnim, and C. Dagdeviren, "The Future of Neuroimplantable Devices : A Materials Science and Regulatory Perspective," vol. 1901482, pp. 1–26, 2019.

[53] A. Lecomte, E. Descamps, and C. Bergaud, "A review on mechanical considerations for chronically-implanted neural probes," *J. Neural Eng.*, vol. 15, no. 3, p. aa8b4f, 2018.

[54] R. W. Griffith and D. R. Humphrey, "Long-term gliosis around chronically implanted platinum electrodes in the Rhesus macaque motor cortex," *Neurosci. Lett.*, vol. 406, no. 1–2, pp. 81–86, Oct. 2006.

[55] J. N. Turner *et al.*, "Cerebral astrocyte response to micromachined silicon implants," *Exp. Neurol.*, vol. 156, no. 1, pp. 33–49, 1999.

[56] D. H. Szarowski *et al.*, "Brain responses to micro-machined silicon devices," *Brain Res.*, vol. 983, no. 1–2, pp. 23–35, Sep. 2003.

[57] J. K. Nguyen *et al.*, "Mechanically-compliant intracortical implants reduce the neuroinflammatory response," *J. Neural Eng.*, vol. 11, no. 5, pp. 1–27, 2014.

[58] E. Giannessi, M. R. Stornelli, A. Coli, and P. N. Sergi, "A quantitative investigation on the peripheral nerve response within the small strain range," *Appl. Sci.*, vol. 9, no. 6, pp. 1–13, 2019.

[59] E. Spedden, J. D. White, E. N. Naumova, D. L. Kaplan, and C. Staii, "Elasticity Maps of Living Neurons Measured by Combined Fluorescence and Atomic Force Microscopy," 2012.

[60] J. Muthuswamy, A. Sridharan, and M. Okandan, "MEMS Neural Probes," in *Encyclopedia of Nanotechnology*, Springer Netherlands, 2016, pp. 1993–2009.

[61] B. Burle, L. Spieser, C. Roger, L. Casini, T. Hasbroucq, and F. Vidal, "Spatial and temporal resolutions of EEG: Is it really black and white? A scalp current density view," *Int. J.*

Psychophysiol., vol. 97, no. 3, pp. 210–220, Sep. 2015.

[62] J. Kim *et al.*, "Flexible thin film electrode arrays for minimally-invasive neurological monitoring," *Proc. 31st Annu. Int. Conf. IEEE Eng. Med. Biol. Soc. Eng. Futur. Biomed. EMBC 2009*, pp. 5506–5509, 2009.

[63] N. J. Hill *et al.*, "Recording Human Electrocorticographic (ECoG) Signals for Neuroscientific Research and Real-time Functional Cortical Mapping," *J. Vis. Exp.*, no. 64, pp. 1–5, 2012.

[64] A. Kuruvilla and R. Flink, "Intraoperative electrocorticography in epilepsy surgery: Useful or not?," *Seizure*, vol. 12, no. 8, pp. 577–584, 2003.

[65] P. Brunner *et al.*, "A practical procedure for real-time functional mapping of eloquent cortex using electrocorticographic signals in humans.," *Epilepsy Behav.*, vol. 15, no. 3, pp. 278–86, Jul. 2009.

[66] E. Asano *et al.*, "Origin and propagation of epileptic spasms delineated on electrocorticography," *Epilepsia*, vol. 46, no. 7, pp. 1086–1097, Jul. 2005.

[67] H. Sugano, H. Shimizu, and S. Sunaga, "Efficacy of intraoperative electrocorticography for assessing seizure outcomes in intractable epilepsy patients with temporal-lobe-mass lesions.," *Seizure*, vol. 16, no. 2, pp. 120–7, Mar. 2007.

[68] R. A. Malkin and B. D. Pendley, "Construction of a very high-density extracellular electrode array," *Am. J. Physiol. - Hear. Circ. Physiol.*, vol. 279, no. 1 48-1, 2000.

[69] O. A. Petroff, D. D. Spencer, I. I. Goncharova, and H. P. Zaveri, "A comparison of the power spectral density of scalp EEG and subjacent electrocorticograms," *Clin. Neurophysiol.*, vol. 127, no. 2, pp. 1108–1112, Feb. 2016.

[70] M. Shokoueinejad *et al.*, "Progress in the field of micro-electrocorticography," *Micromachines*, vol. 10, no. 1, pp. 1–19, 2019.

[71] G. Schalk and E. C. Leuthardt, "Brain-Computer Interfaces Using Electrocorticographic Signals," *IEEE Rev. Biomed. Eng.*, vol. 4, pp. 140–154, 2011.

[72] K. A. Moxon and G. Foffani, "Brain-machine interfaces beyond neuroprosthetics," *Neuron*, vol. 86, no. 1, pp. 55–67, 2015.

[73] G. Schalk, D. J. Mcfarland, T. Hinterberger, N. Birbaumer, J. R. Wolpaw, and A. B. I. B. C. I. Technology, "BCI2000 : A General-Purpose Brain-Computer Interface (BCI) System," vol. 51, no. 6, pp. 1034–1043, 2004.

[74] E. C. Leuthardt, G. Schalk, J. R. Wolpaw, J. G. Ojemann, and D. W. Moran, "A brain-computer interface using electrocorticographic signals in humans," *J. Neural Eng.*, vol. 1, no. 2, pp. 63–71, 2004.

[75] D. A. Moses, M. K. Leonard, J. G. Makin, and E. F. Chang, "Real-time decoding of question-and-answer speech dialogue using human cortical activity," *Nat. Commun.*, vol. 10, no. 1, Dec. 2019.

[76] J. W. Salatino, K. A. Ludwig, T. D. Y. Kozai, and E. K. Purcell, "Glial responses to implanted electrodes in the brain," *Nat. Biomed. Eng.*, vol. 1, no. 11, pp. 862–877, 2017.

[77] M. Jorfi, J. L. Skousen, C. Weder, and J. R. Capadona, “Progress towards biocompatible intracortical microelectrodes for neural interfacing applications.,” *J. Neural Eng.*, vol. 12, no. 1, p. 011001, Feb. 2015.

[78] V. S. Polikov, P. A. Tresco, and W. M. Reichert, “Response of brain tissue to chronically implanted neural electrodes.,” *J. Neurosci. Methods*, vol. 148, no. 1, pp. 1–18, Oct. 2005.

[79] R. Biran, D. C. Martin, and P. A. Tresco, “The brain tissue response to implanted silicon microelectrode arrays is increased when the device is tethered to the skull,” *J. Biomed. Mater. Res. - Part A*, vol. 82, no. 1, pp. 169–178, Jul. 2007.

[80] C. Marin and E. Fernández, “Biocompatibility of intracortical microelectrodes: Current status and future prospects,” *Front. Neuroeng.*, vol. 3, no. MAY, May 2010.

[81] M. Welkenhuysen, A. Andrei, L. Ameye, W. Eberle, and B. Nuttin, “Effect of insertion speed on tissue response and insertion mechanics of a chronically implanted silicon-based neural probe.,” *IEEE Trans. Biomed. Eng.*, vol. 58, no. 11, pp. 3250–9, Nov. 2011.

[82] D. J. Edell, V. V Toi, V. M. McNeil, and L. D. Clark, “Factors influencing the biocompatibility of insertable silicon microshafts in cerebral cortex.,” *IEEE Trans. Biomed. Eng.*, vol. 39, no. 6, pp. 635–43, Jun. 1992.

[83] Z. Fekete, A. Németh, G. Márton, I. Ulbert, and A. Pongrácz, “Experimental study on the mechanical interaction between silicon neural microprobes and rat dura mater during insertion.,” *J. Mater. Sci. Mater. Med.*, vol. 26, no. 2, p. 70, Feb. 2015.

[84] A. Gilletti and J. Muthuswamy, “Brain micromotion around implants in the rodent somatosensory cortex.,” *J. Neural Eng.*, vol. 3, no. 3, pp. 189–95, Sep. 2006.

[85] R. H. Britt and G. T. Rossi, “Quantitative analysis of methods for reducing physiological brain pulsations.,” *J. Neurosci. Methods*, vol. 6, no. 3, pp. 219–29, Sep. 1982.

[86] Y.-T. Kim, R. W. Hitchcock, M. J. Bridge, and P. A. Tresco, “Chronic response of adult rat brain tissue to implants anchored to the skull.,” *Biomaterials*, vol. 25, no. 12, pp. 2229–37, May 2004.

[87] A. M. Stiller *et al.*, “Chronic intracortical recording and electrochemical stability of thiol-ene/acrylate shape memory polymer electrode arrays,” *Micromachines*, vol. 9, no. 10, pp. 1–14, 2018.

[88] T. D. Y. Kozai, A. S. Jaquins-Gerstl, A. L. Vazquez, A. C. Michael, and X. T. Cui, “Dexamethasone retrodialysis attenuates microglial response to implanted probes in vivo,” *Biomaterials*, vol. 87, pp. 157–169, May 2016.

[89] L. Uebersax, M. Mattotti, M. Papaloïzos, H. P. Merkle, B. Gander, and L. Meinel, “Silk fibroin matrices for the controlled release of nerve growth factor (NGF),” *Biomaterials*, vol. 28, no. 30, pp. 4449–4460, Oct. 2007.

[90] W. Shi *et al.*, “BDNF blended chitosan scaffolds for human umbilical cord MSC transplants in traumatic brain injury therapy,” *Biomaterials*, vol. 33, no. 11, pp. 3119–3126, Apr. 2012.

[91] Z. Bérces *et al.*, “Neurobiochemical changes in the vicinity of a nanostructured neural implant,” *Sci. Rep.*, vol. 6, Oct. 2016.

[92] H. S. Sohal *et al.*, "The sinusoidal probe: A new approach to improve electrode longevity," *Front. Neuroeng.*, vol. 7, no. APR, Apr. 2014.

[93] M. P. Ward, P. Rajdev, C. Ellison, and P. P. Irazoqui, "Toward a comparison of microelectrodes for acute and chronic recordings," *Brain Res.*, vol. 1282, pp. 183–200, Jul. 2009.

[94] M. A. Hopcroft, W. D. Nix, and T. W. Kenny, "What is the Young's modulus of silicon?," *J. Microelectromechanical Syst.*, vol. 19, no. 2, pp. 229–238, Apr. 2010.

[95] J. C. Barrese *et al.*, "Failure mode analysis of silicon-based intracortical microelectrode arrays in non-human primates.," *J. Neural Eng.*, vol. 10, no. 6, p. 066014, Dec. 2013.

[96] A. Sridharan, J. K. Nguyen, J. R. Capadona, and J. Muthuswamy, "Compliant intracortical implants reduce strains and strain rates in brain tissue in vivo.," *J. Neural Eng.*, vol. 12, no. 3, p. 036002, Jun. 2015.

[97] M. Polanco, H. Yoon, and S. Bawab, "Micromotion-induced dynamic effects from a neural probe and brain tissue interface," *J. Micro/Nanolithography, MEMS, MOEMS*, vol. 13, no. 2, p. 023009, Jun. 2014.

[98] K. B. Bjugstad, K. Lampe, D. S. Kern, and M. Mahoney, "Biocompatibility of poly(ethylene glycol)-based hydrogels in the brain: An analysis of the glial response across space and time," *J. Biomed. Mater. Res. - Part A*, vol. 95, no. 1, pp. 79–91, Oct. 2010.

[99] K. C. Spencer, J. C. Sy, K. B. Ramadi, A. M. Graybiel, R. Langer, and M. J. Cima, "Characterization of Mechanically Matched Hydrogel Coatings to Improve the Biocompatibility of Neural Implants," *Sci. Rep.*, vol. 2017, no. MAY, pp. 1–16, 2017.

[100] U. A. Aregueta-Robles, A. J. Woolley, L. A. Poole-Warren, N. H. Lovell, and R. A. Green, "Organic electrode coatings for next-generation neural interfaces," *Front. Neuroeng.*, vol. 7, no. MAY, May 2014.

[101] J. L. Skousen, M. J. Bridge, and P. A. Tresco, "A strategy to passively reduce neuroinflammation surrounding devices implanted chronically in brain tissue by manipulating device surface permeability," *Biomaterials*, vol. 36, pp. 33–43, Jan. 2015.

[102] C. D. Lee *et al.*, "Matrigel coatings for Parylene sheath neural probes," pp. 357–368, 2015.

[103] A. Guiseppi-Elie, "Electroconductive hydrogels: Synthesis, characterization and biomedical applications," *Biomaterials*, vol. 31, no. 10, pp. 2701–2716, 2010.

[104] G. L. Mario Cheong, K. S. Lim, A. Jakubowicz, P. J. Martens, L. A. Poole-Warren, and R. A. Green, "Conductive hydrogels with tailored bioactivity for implantable electrode coatings," *Acta Biomater.*, vol. 10, no. 3, pp. 1216–1226, Mar. 2014.

[105] R. A. Green, G. J. Suaning, L. A. Poole-Warren, and N. H. Lovell, "Bioactive conducting polymers for neural interfaces: Application to vision prosthesis," in *2009 4th International IEEE/EMBS Conference on Neural Engineering, NER '09*, 2009, pp. 60–63.

[106] K. Y. Lee, J. A. Rowley, P. Eiselt, E. M. Moy, K. H. Bouhadir, and D. J. Mooney, "Controlling Mechanical and Swelling Properties of Alginate Hydrogels Independently by Cross-Linker Type and Cross-Linking Density," *Macromolecules*, vol. 33, no. 11, pp. 4291–4294, May 2000.

[107] Y. Y. Chen *et al.*, "Design and fabrication of a polyimide-based microelectrode array: Application in neural recording and repeatable electrolytic lesion in rat brain," *J. Neurosci. Methods*, vol. 182, no. 1, pp. 6–16, Aug. 2009.

[108] K. C. Cheung, P. Renaud, H. Tanila, and K. Djupsund, "Flexible polyimide microelectrode array for in vivo recordings and current source density analysis," *Biosens. Bioelectron.*, vol. 22, no. 8, pp. 1783–1790, 2007.

[109] A. Mercanzini *et al.*, "Demonstration of cortical recording using novel flexible polymer neural probes," *Sensors Actuators, A Phys.*, vol. 143, no. 1, pp. 90–96, 2008.

[110] S. Takeuchi, T. Suzuki, K. Mabuchi, and H. Fujita, "3D flexible multichannel neural probe array," *J. Micromechanics Microengineering*, vol. 14, no. 1, pp. 104–107, Jan. 2004.

[111] P. J. Rousche, D. S. Pellinen, D. P. Pivin, J. C. Williams, R. J. Vetter, and D. R. Kipke, "Flexible polyimide-based intracortical electrode arrays with bioactive capability," *IEEE Trans. Biomed. Eng.*, vol. 48, no. 3, pp. 361–370, 2001.

[112] B. A. Wester, R. H. Lee, and M. C. LaPlaca, "Development and characterization of in vivo flexible electrodes compatible with large tissue displacements.," *J. Neural Eng.*, vol. 6, no. 2, p. 024002, 2009.

[113] S. Takeuchi, D. Ziegler, Y. Yoshida, K. Mabuchi, and T. Suzuki, "Parylene flexible neural probes integrated with microfluidic channels.," *Lab Chip*, vol. 5, no. 5, pp. 519–523, 2005.

[114] J. T. W. Kuo *et al.*, "Novel flexible Parylene neural probe with 3D sheath structure for enhancing tissue integration.," *Lab Chip*, vol. 13, no. 4, pp. 554–561, 2013.

[115] B. J. Kim *et al.*, "3D Parylene sheath neural probe for chronic recordings," *J. Neural Eng.*, vol. 10, no. 4, Aug. 2013.

[116] S. A. Hara, B. J. Kim, J. T. W. Kuo, and C. D. Lee, "Long-term stability of intracortical recordings using perforated and arrayed Parylene sheath electrodes," 2016.

[117] G. Márton, G. Orbán, M. Kiss, R. Fiáth, A. Pongrácz, and I. Ulbert, "A Multimodal, SU-8 - Platinum - Polyimide Microelectrode Array for Chronic In Vivo Neurophysiology," *PLoS One*, vol. 10, no. 12, p. e0145307, Dec. 2015.

[118] S. H. Huang, S. P. Lin, and J. J. J. Chen, "In vitro and in vivo characterization of SU-8 flexible neuroprobe: From mechanical properties to electrophysiological recording," *Sensors Actuators, A Phys.*, vol. 216, pp. 257–265, Sep. 2014.

[119] K. S. Min *et al.*, "A liquid crystal polymer-based neuromodulation system: An application on animal model of neuropathic pain," *Neuromodulation*, vol. 17, no. 2, pp. 160–169, 2014.

[120] J. Subbaroyan, D. C. Martin, and D. R. Kipke, "A finite-element model of the mechanical effects of implantable microelectrodes in the cerebral cortex," *J. Neural Eng.*, vol. 2, no. 4, pp. 103–113, Dec. 2005.

[121] Y. Kato, I. Saito, T. Hoshino, T. Suzuki, and K. Mabuchi, "Preliminary study of multichannel flexible neural probes coated with hybrid biodegradable polymer," in *Annual International Conference of the IEEE Engineering in Medicine and Biology - Proceedings*, 2006, pp. 660–663.

[122] C. Hassler, J. Guy, M. Nietzschmann, D. T. T. Plachta, J. F. Staiger, and T. Stieglitz, “Intracortical polyimide electrodes with a bioresorbable coating,” *Biomed. Microdevices*, vol. 18, no. 5, Oct. 2016.

[123] S. Takeuchi, D. Ziegler, Y. Yoshida, K. Mabuchi, and T. Suzuki, “Parylene flexible neural probes integrated with microfluidic channels,” *Lab Chip*, vol. 5, no. 5, p. 519, Apr. 2005.

[124] J. Agorelius, F. Tsanakalis, A. Friberg, P. T. Thorbergsson, L. M. E. Pettersson, and J. Schouenborg, “An array of highly flexible electrodes with a tailored configuration locked by gelatin during implantation-initial evaluation in cortex cerebri of awake rats,” *Front. Neurosci.*, vol. 9, no. SEP, pp. 1–12, 2015.

[125] Z. Xiang, S. Yen, N. Xue, and T. Sun, “Ultra-thin flexible polyimide neural probe embedded in a dissolvable maltose-coated microneedle.”

[126] F. Wu, M. Im, and E. Yoon, “A flexible fish-bone-shaped neural probe strengthened by biodegradable silk coating for enhanced biocompatibility,” in *2011 16th International Solid-State Sensors, Actuators and Microsystems Conference, TRANSDUCERS’11*, 2011, pp. 966–969.

[127] A. Lecomte *et al.*, “Silk and PEG as means to stiffen parylene probes for insertion in the brain: a comparison,” *J. Micromechanics Microengineering*, vol. 125003, no. September, 2015.

[128] M. E. Gomes and R. L. Reis, “Biodegradable polymers and composites in biomedical applications: From catgut to tissue engineering Part 2 Systems for temporary replacement and advanced tissue regeneration,” *International Materials Reviews*, vol. 49, no. 5. pp. 274–285, Oct-2004.

[129] H.-J. Jin *et al.*, “Water-Stable Silk Films with Reduced β-Sheet Content,” *Adv. Funct. Mater.*, vol. 15, no. 8, pp. 1241–1247, Aug. 2005.

[130] L. Cooperman and D. Michaeli, “The immunogenicity of injectable collagen. I. A 1-year prospective study,” *J. Am. Acad. Dermatol.*, vol. 10, no. 4, pp. 638–646, 1984.

[131] S. Felix *et al.*, “Removable silicon insertion stiffeners for neural probes using polyethylene glycol as a biodissolvable adhesive,” in *Proceedings of the Annual International Conference of the IEEE Engineering in Medicine and Biology Society, EMBS*, 2012, pp. 871–874.

[132] F. Barz, P. Ruther, S. Takeuchi, and O. Paul, “Flexible silicon-polymer neural probe rigidified by dissolvable insertion vehicle for high-resolution neural recording with improved duration,” in *Proceedings of the IEEE International Conference on Micro Electro Mechanical Systems (MEMS)*, 2015, vol. 2015-February, no. February, pp. 636–639.

[133] D. P. O’Brien, T. R. Nichols, and M. G. Allen, “Flexible microelectrode arrays with integrated insertion devices,” in *Proceedings of the IEEE Micro Electro Mechanical Systems (MEMS)*, 2001, pp. 216–219.

[134] T. D. Y. Kozai and D. R. Kipke, “Insertion shuttle with carboxyl terminated self-assembled monolayer coatings for implanting flexible polymer neural probes in the brain,” *J. Neurosci. Methods*, vol. 184, no. 2, pp. 199–205, Nov. 2009.

[135] K. K. Lee *et al.*, “Polyimide-based intracortical neural implant with improved structural stiffness,” *J. Micromechanics Microengineering*, vol. 14, no. 1, pp. 32–37, Jan. 2004.

[136] E. G. R. Kim *et al.*, "A hybrid silicon–parylene neural probe with locally flexible regions," *Sensors Actuators B Chem.*, vol. 195, pp. 416–422, May 2014.

[137] F. Pilate, A. Toncheva, P. Dubois, and J. M. Raquez, "Shape-memory polymers for multiple applications in the materials world," *Eur. Polym. J.*, vol. 80, pp. 268–294, 2016.

[138] Q. Zhao, H. J. Qi, and T. Xie, "Recent progress in shape memory polymer: New behavior, enabling materials, and mechanistic understanding," *Prog. Polym. Sci.*, vol. 49–50, pp. 79–120, 2015.

[139] S. M. Hosseini *et al.*, "Softening Shape Memory Polymer Substrates for Bioelectronic Devices With Improved Hydrolytic Stability," *Front. Mater.*, vol. 5, no. November, pp. 1–12, 2018.

[140] M. D. Hager, S. Bode, C. Weber, and U. S. Schubert, "Shape memory polymers: Past, present and future developments," *Prog. Polym. Sci.*, vol. 49–50, pp. 3–33, 2015.

[141] J. R. Capadona, K. Shanmuganathan, D. J. Tyler, S. J. Rowan, and C. Weder, "Stimuli-responsive polymer nanocomposites inspired by the sea cucumber dermis," *Science (80-.).*, vol. 319, no. 5868, pp. 1370–1374, Mar. 2008.

[142] J. P. Harris *et al.*, "Mechanically adaptive intracortical implants improve the proximity of neuronal cell bodies," *J. Neural Eng.*, vol. 8, no. 6, Dec. 2011.

[143] T. Ware *et al.*, "Fabrication of Responsive, Softening Neural Interfaces," *Adv. Funct. Mater.*, vol. 22, no. 16, pp. 3470–3479, Aug. 2012.

[144] T. Ware *et al.*, "Three-dimensional flexible electronics enabled by shape memory polymer substrates for responsive neural interfaces," *Macromol. Mater. Eng.*, vol. 297, no. 12, pp. 1193–1202, Dec. 2012.

[145] T. Ware *et al.*, "Thiol-ene = acrylate substrates for softening intracortical electrodes," pp. 1–11, 2013.

[146] D. M. Simon *et al.*, "Design and demonstration of an intracortical probe technology with tunable modulus," *J. Biomed. Mater. Res. - Part A*, vol. 105, no. 1, pp. 159–168, 2017.

[147] A. J. Shoffstall *et al.*, "Characterization of the neuroinflammatory response to thiol-ene shape memory polymer coated intracortical microelectrodes," *Micromachines*, vol. 9, no. 10, pp. 1–18, 2018.

[148] B. J. Black *et al.*, "In vitro compatibility testing of thiol-ene/acrylate-based shape memory polymers for use in implantable neural interfaces," *J. Biomed. Mater. Res. - Part A*, vol. 106, no. 11, pp. 2891–2898, 2018.

[149] A. Sridharan, S. D. Rajan, and J. Muthuswamy, "Long-term changes in the material properties of brain tissue at the implant-tissue interface," *J. Neural Eng.*, vol. 10, no. 6, Dec. 2013.

[150] A. Zátonyi *et al.*, "A softening laminar electrode for recording single unit activity from the rat hippocampus," *Sci. Rep.*, vol. 9, no. 1, p. 2321, Dec. 2019.

[151] D.-H. Do, M. Ecker, and W. E. Voit, "Characterization of a Thiol-Ene/Acrylate-Based Polymer for Neuroprosthetic Implants," *ACS Omega*, vol. 2, no. 8, pp. 4604–4611, 2017.

[152] Y. M. Lee, S. H. Kim, and C. S. Cho, “Synthesis and swelling characteristics of pH and thermoresponsive interpenetrating polymer network hydrogel composed of poly(vinyl alcohol) and poly(acrylic acid),” *J. Appl. Polym. Sci.*, vol. 62, no. 2, pp. 301–311, 1996.

[153] H. S. Sohal, K. Vassilevski, A. Jackson, S. N. Baker, and A. O’Neill, “Design and Microfabrication Considerations for Reliable Flexible Intracortical Implants ,” *Front. Mech. Eng.* , vol. 2, no. June, pp. 1–11, 2016.

[154] I. Peter Ledochowitsch, Elisa Olivero, Tim Blanche, and Michel M. Maharbiz, Member, “A transparent uECoG array for simultaneuos recording and optogenetic stimulation,” in *Conf Proc IEEE Eng Med Biol Soc*, 2011, pp. 2937–40.

[155] H. P. Neves, *Materials for implantable systems*. Woodhead Publishing Limited, 2013.

[156] O. Sinitsyna, P. Paralikar, R. Pandit, and M. Rai, “Platinum in biomedical applications,” in *Biomedical Applications of Metals*, Springer International Publishing, 2018, pp. 151–165.

[157] M. Leber *et al.*, “Long term performance of porous platinum coated neural electrodes,” *Biomed. Microdevices*, vol. 19, no. 3, p. 62, Sep. 2017.

[158] G. Marton *et al.*, “Deep-brain silicon multielectrodes with surface-modified Pt recording sites,” *Proc. IEEE Sensors*, 2012.

[159] B. Ilic, D. Czaplewski, P. Neuzil, T. Stanczyk, J. Blough, and G. J. Maclay, “Preparation and characterization of platinum black electrodes,” *J. Mater. Sci.*, vol. 35, no. 14, pp. 3447–3457, 2000.

[160] X. T. Cui and D. D. Zhou, “Poly (3,4-ethylenedioxythiophene) for chronic neural stimulation,” *IEEE Trans. Neural Syst. Rehabil. Eng.*, vol. 15, no. 1, pp. 502–508, 2007.

[161] Y. Xia, K. Sun, and J. Ouyang, “Highly conductive poly(3,4-ethylenedioxythiophene):Poly(styrene sulfonate) films treated with an amphiphilic fluoro compound as the transparent electrode of polymer solar cells,” *Energy Environ. Sci.*, vol. 5, no. 1, pp. 5325–5332, 2012.

[162] M. Sessolo *et al.*, “Easy-to-fabricate conducting polymer microelectrode arrays,” *Adv. Mater.*, vol. 25, no. 15, pp. 2135–2139, 2013.

[163] N. Yi and M. R. Abidian, *10 - Conducting polymers and their biomedical applications*. 2016.

[164] J. Ouyang, Q. Xu, C. Chu, Y. Yang, G. Li, and J. Shinar, “On the mechanism of conductivity enhancement in through solvent treatment,” vol. 45, pp. 8443–8450, 2004.

[165] Y. Xia and J. Ouyang, “Significant conductivity enhancement of conductive poly(3,4-ethylenedioxythiophene): Poly(styrenesulfonate) films through a treatment with organic carboxylic acids and inorganic acids,” *ACS Appl. Mater. Interfaces*, vol. 2, no. 2, pp. 474–483, 2010.

[166] P. Li, K. Sun, and J. Ouyang, “Stretchable and Conductive Polymer Films Prepared by Solution Blending,” *ACS Appl. Mater. Interfaces*, vol. 7, no. 33, pp. 18415–18423, 2015.

[167] A. Schander *et al.*, “Design and fabrication of novel multi-channel floating neural probes for intracortical chronic recording,” *Sensors Actuators, A Phys.*, vol. 247, pp. 125–135, 2016.

[168] K. Lim *et al.*, “Improving Electrical Conductivity of PEDOT:PSS with Phase Separation by Applying Electric Fields,” *Bull. Korean Chem. Soc.*, vol. 39, no. 4, pp. 469–476, 2018.

[169] J. Liu, X. Wang, D. Li, N. E. Coates, R. A. Segalman, and D. G. Cahill, “Thermal conductivity and elastic constants of PEDOT:PSS with high electrical conductivity,” *Macromolecules*, vol. 48, no. 3, pp. 585–591, 2015.

[170] Y. Furukawa, A. Shimada, K. Kato, H. Iwata, and K. Torimitsu, “Monitoring neural stem cell differentiation using PEDOT-PSS based MEA,” *Biochim. Biophys. Acta - Gen. Subj.*, vol. 1830, no. 9, pp. 4329–4333, 2013.

[171] C. L. Kolarcik *et al.*, “Evaluation of poly(3,4-ethylenedioxythiophene)/carbon nanotube neural electrode coatings for stimulation in the dorsal root ganglion,” *J. Neural Eng.*, vol. 12, no. 1, p. 016008, 2015.

[172] H. J. Lee, Y. Son, J. Kim, C. J. Lee, E. S. Yoon, and I. J. Cho, “A multichannel neural probe with embedded microfluidic channels for simultaneous in vivo neural recording and drug delivery,” *Lab Chip*, vol. 15, no. 6, pp. 1590–1597, 2015.

[173] A. Leblois and C. Pouzat, “Multi-Unit Recording,” in *Neurobiology of Motor Control*, John Wiley & Sons, Inc., 2017, pp. 55–73.

[174] M. I. Chelaru and M. S. Jog, “Spike source localization with tetrodes,” *J. Neurosci. Methods*, vol. 142, no. 2, pp. 305–315, Mar. 2005.

[175] F. Mechler, J. D. Victor, I. Ohiorhenuan, A. M. Schmid, and Q. Hu, “Three-dimensional localization of neurons in cortical tetrode recordings,” *J. Neurophysiol.*, vol. 106, no. 2, pp. 828–848, Aug. 2011.

[176] H. Y. Gao, C. de Solages, and C. Lena, “Tetrode recordings in the cerebellar cortex,” *J. Physiol. Paris*, vol. 106, no. 3–4, pp. 128–136, May 2012.

[177] G. Buzsáki and X.-J. Wang, “Mechanisms of Gamma Oscillations,” *Annu. Rev. Neurosci.*, vol. 35, no. 1, pp. 203–225, Jul. 2012.

[178] W. Franks, I. Schenker, P. Schmutz, and A. Hierlemann, “Impedance characterization and modeling of electrodes for biomedical applications,” *IEEE Trans. Biomed. Eng.*, vol. 52, no. 7, pp. 1295–1302, 2005.

[179] M. Bariatto and A. Fontes, “Impedance Characterization and Modeling of Microelectrodes for Neural Recording,” *Natl. Inst. Astrophys. Opt. Electron.*, pp. 108–113.

[180] C. V. Chaparro, L. V. Herrera, A. M. Meléndez, and D. A. Miranda, “Considerations on electrical impedance measurements of electrolyte solutions in a four-electrode cell,” in *Journal of Physics: Conference Series*, 2016, vol. 687, no. 1.

[181] T. Rongyu *et al.*, “Fabrication of strongly adherent platinum black coatings on microelectrodes array,” vol. 57, no. April, pp. 1–10, 2014.

[182] S. Bhunia, S. Majerus, and M. Sawan, *Implantable biomedical microsystems : design principles and applications*. .

[183] T. Fakult, B. Vorgelegt, A. Kloke, and D. N. Eth, “Highly Porous Platinum Electrodes for the Use in Potentially Implantable Glucose Fuel Cells,” 2012.

[184] P. Takmakov, K. Ruda, K. Scott Phillips, I. S. Isayeva, V. Krauthamer, and C. G. Welle, “Rapid evaluation of the durability of cortical neural implants using accelerated aging with reactive oxygen species,” *J. Neural Eng.*, vol. 12, no. 2, p. 026003, Apr. 2015.

[185] J. P. Seymour, Y. M. Elkasabi, H. Y. Chen, J. Lahann, and D. R. Kipke, “The insulation performance of reactive parylene films in implantable electronic devices,” *Biomaterials*, vol. 30, no. 31, pp. 6158–6167, 2009.

[186] E. M. Davis, N. M. Benetatos, W. F. Regnault, K. I. Winey, and Y. A. Elabd, “The influence of thermal history on structure and water transport in Parylene C coatings,” *Polymer (Guildf).*, vol. 52, no. 23, pp. 5378–5386, Oct. 2011.

[187] B. Łosiewicz, R. Jurczakowski, and A. Lasia, “Kinetics of hydrogen underpotential deposition at polycrystalline platinum in acidic solutions,” *Electrochim. Acta*, vol. 80, pp. 292–301, Oct. 2012.

[188] A. Więckowski, *Interfacial electrochemistry : theory, experiment, and applications*. Marcel Dekker, 1999.

[189] C. Masarapu, H. F. Zeng, K. H. Hung, and B. Wei, “Effect of Temperature on the Capacitance of Carbon Nanotube Supercapacitors,” *ACS Nano*, vol. 3, no. 8, pp. 2199–2206, Aug. 2009.

[190] W. Wang *et al.*, “Hydrous Ruthenium Oxide Nanoparticles Anchored to Graphene and Carbon Nanotube Hybrid Foam for Supercapacitors,” *Sci. Rep.*, vol. 4, no. 1, p. 4452, May 2015.

[191] R. J. Vetter, J. C. Williams, J. F. Hetke, E. A. Nunamaker, and D. R. Kipke, “Chronic neural recording using silicon-substrate microelectrode arrays implanted in cerebral cortex,” *IEEE Trans. Biomed. Eng.*, vol. 51, no. 6, pp. 896–904, Jun. 2004.

[192] A. D. Degenhart *et al.*, “Histological evaluation of a chronically-implanted electrocorticographic electrode grid in a non-human primate,” *J. Neural Eng.*, vol. 13, no. 4, Jun. 2016.

[193] N. Helassa, B. Podor, A. Fine, and K. Török, “Design and mechanistic insight into ultrafast calcium indicators for monitoring intracellular calcium dynamics,” *Sci. Rep.*, vol. 6, no. December, pp. 1–14, 2016.

[194] Z. Fekete and A. Pongrácz, “Multifunctional soft implants to monitor and control neural activity in the central and peripheral nervous system: A review,” *Sensors Actuators, B Chem.*, vol. 243, pp. 1214–1223, 2017.

[195] B. Rubehn, C. Bosman, R. Oostenveld, P. Fries, and T. Stieglitz, “A MEMS-based flexible multichannel ECoG-electrode array,” *J. Neural Eng.*, vol. 6, no. 3, 2009.

[196] T. Stieglitz, H. Beutel, M. Schuettler, and J.-U. Meyer, “Micromachined, Polyimide-Based Devices for Flexible Neural Interfaces,” *Biomed. Microdevices*, vol. 2, no. 4, pp. 283–294, 2000.

[197] J. Kim, J. A. Wilson, J. C. Williams, A. Microfabrication, and E. Arrays, “A Cortical Recording Platform Utilizing μ ECoG Electrode Arrays - Kim et al. - 2007.pdf,” vol. 2721, no. c, pp. 5353–5357, 2007.

[198] B. A. Hollenberg, C. D. Richards, R. Richards, D. F. Bahr, and D. M. Rector, “A MEMS fabricated flexible electrode array for recording surface field potentials,” *J. Neurosci. Methods*, vol. 153, no. 1, pp. 147–153, May 2006.

[199] A. A. Schendel *et al.*, “A cranial window imaging method for monitoring vascular growth around chronically implanted micro-ECoG devices,” *J. Neurosci. Methods*, vol. 218, no. 1, pp. 121–130, Aug. 2013.

[200] T. J. Richner *et al.*, “Optogenetic micro-electrocorticography for modulating and localizing cerebral cortex activity.,” *J. Neural Eng.*, vol. 11, no. 1, p. 016010, 2014.

[201] R. Muller *et al.*, “A Minimally Invasive 64-Channel Wireless µeCoG Implant,” *IEEE J. Solid-State Circuits*, vol. 50, no. 1, pp. 344–359, 2015.

[202] S. Gong *et al.*, “Fabrication of Highly Transparent and Flexible NanoMesh Electrode via Self-assembly of Ultrathin Gold Nanowires,” *Adv. Electron. Mater.*, vol. 2, no. 7, 2016.

[203] C. Hébert *et al.*, “Flexible Graphene Solution-Gated Field-Effect Transistors: Efficient Transducers for Micro-Electrocorticography,” *Adv. Funct. Mater.*, vol. 28, no. 12, p. 1703976, Mar. 2018.

[204] D.-W. Park *et al.*, “Graphene-based carbon-layered electrode array technology for neural imaging and optogenetic applications.,” *Nat. Commun.*, vol. 5, p. 5258, Oct. 2014.

[205] B. M. Blaschke *et al.*, “Mapping brain activity with flexible graphene micro-transistors,” *2D Mater.*, vol. 4, no. 2, p. 025040, Feb. 2017.

[206] J. Zhang *et al.*, “Stretchable Transparent Electrode Arrays for Simultaneous Electrical and Optical Interrogation of Neural Circuits in Vivo,” *Nano Lett.*, vol. 18, no. 5, pp. 2903–2911, 2018.

[207] V. Castagnola *et al.*, “Parylene-based flexible neural probes with PEDOT coated surface for brain stimulation and recording,” *Biosens. Bioelectron.*, vol. 67, pp. 450–457, 2015.

[208] K. Y. Kwon, S. Member, B. Sirowatka, A. Weber, and W. Li, “Opto- Array : A Hybrid Neural Interface With Transparent Electrode Array and Integrated LEDs for Optogenetics,” vol. 7, no. 5, pp. 593–600, 2013.

[209] E. H. Kim, C. W. Yang, and J. W. Park, “Improving the delamination resistance of indium tin oxide (ITO) coatings on polymeric substrates by O2 plasma surface treatment,” *Curr. Appl. Phys.*, vol. 10, no. SUPPL. 3, pp. S510–S514, 2010.

[210] K. Ellmer, “Past achievements and future challenges in the development of optically transparent electrodes,” *Nature Photonics*, vol. 6, no. 12. pp. 809–817, Dec-2012.

[211] R. Paetzold, K. Heuser, D. Henseler, S. Roeger, G. Wittmann, and A. Winnacker, “Performance of flexible polymeric light-emitting diodes under bending conditions,” *Appl. Phys. Lett.*, vol. 82, no. 19, pp. 3342–3344, May 2003.

[212] P. Ledochowitsch, E. Olivero, and M. M. Maharbiz, “An Optically Transparent , Gold-ITO-Hybrid Electrode Array for Integration of Electrocorticography with Optogenetic Techniques,” vol. 3, p. 94720, 2011.

[213] C. G. . H. A. Granqvist, “Transparent and Conducting ITO Films: New Developments and

Applications," *Thin Solid Films*, vol. 411, pp. 1–5, 2002.

[214] N. Kunori and I. Takashima, "A transparent epidural electrode array for use in conjunction with optical imaging.," *J. Neurosci. Methods*, vol. 251, pp. 130–7, 2015.

[215] P. Ledochowitsch *et al.*, "Strategies for optical control and simultaneous electrical readout of extended cortical circuits," *J. Neurosci. Methods*, vol. 256, pp. 220–231, Dec. 2015.

[216] O. Mryasov and A. Freeman, "Electronic band structure of indium tin oxide and criteria for transparent conducting behavior," *Phys. Rev. B*, vol. 64, no. 23, p. 233111, Dec. 2001.

[217] D. Park *et al.*, "Fabrication and utility of a transparent graphene neural electrode array for electrophysiology , in vivo imaging , and optogenetics," *Nat. Protoc.*, vol. 11, no. 11, pp. 2201–2222, 2016.

[218] Y. Zhang *et al.*, "Direct observation of a widely tunable bandgap in bilayer graphene," *Nature*, vol. 459, no. 7248, pp. 820–823, Jun. 2009.

[219] D. Kuzum *et al.*, "Transparent and flexible low noise graphene electrodes for simultaneous electrophysiology and neuroimaging," *Nat. Commun.*, vol. 5, no. May, p. 5259, 2014.

[220] M. Thunemann *et al.*, "Deep 2-photon imaging and artifact-free optogenetics through transparent graphene microelectrode arrays," *Nat. Commun.*, vol. 9, no. 1, p. 2035, Dec. 2018.

[221] Y. Lu *et al.*, "Ultralow Impedance Graphene Microelectrodes with High Optical Transparency for Simultaneous Deep Two-Photon Imaging in Transgenic Mice," *Adv. Funct. Mater.*, vol. 28, no. 31, pp. 1–9, 2018.

[222] T. D. Y. Kozai and A. L. Vazquez, "Photoelectric artefact from optogenetics and imaging on microelectrodes and bioelectronics: new challenges and opportunities," *J. Mater. Chem. B*, vol. 3, no. 25, pp. 4965–4978, Jul. 2015.

[223] J. Selvakumaran, M. P. Hughes, D. J. Ewins, and P. R. Richards, "BIOCOMPATIBILITY STUDIES OF MATERIALS USED FOR CHRONICALLY," pp. 521–525, 2000.

[224] J. Selvakumaran, M. P. Hughes, J. L. Keddie, and D. J. Ewins, "ASSESSING BIOCOMPATIBILITY OF MATERIALS FOR IMPLANTABLE MICROELECTRODES USING CYTOTOXICITY AND PROTEIN ADSORPTION STUDIES," pp. 261–264, 2002.

[225] D.-H. Baek *et al.*, "A thin film polyimide mesh microelectrode for chronic epidural electrocorticography recording with enhanced contactability.," *J. Neural Eng.*, vol. 11, no. 4, p. 046023, 2014.

[226] S. Dong, W. Chen, X. Wang, S. Zhang, K. Xu, and X. Zheng, "Flexible ECoG electrode for implantation and neural signal recording applications," *Vacuum*, vol. 140, pp. 96–100, Jun. 2017.

[227] M. Komatsu, E. Sugano, H. Tomita, and N. Fujii, "A Chronically Implantable Bidirectional Neural Interface for Non-human Primates," *Front. Neurosci.*, vol. 11, Sep. 2017.

[228] B. Ji *et al.*, "Flexible polyimide-based hybrid opto-electric neural interface with 16 channels of micro-LEDs and electrodes," *Microsystems Nanoeng.*, vol. 4, no. 1, Dec. 2018.

[229] Y. X. Kato, S. Furukawa, K. Samejima, N. Hironaka, and M. Kashino, “Photosensitive-polyimide based method for fabricating various neural electrode architectures,” *Front. Neuroeng.*, no. JUNE, Jun. 2012.

[230] G. Márton, G. Orbán, M. Kiss, R. Fiáth, A. Pongrácz, and I. Ulbert, “A multimodal, SU-8 - Platinum - Polyimide microelectrode array for chronic in vivo neurophysiology,” *PLoS One*, vol. 10, no. 12, pp. 1–16, 2015.

[231] J.-M. Kim, C. Im, and W. Lee, “Plateau-Shaped Flexible Polymer Microelectrode Array for Neural Recording,” *Polymers (Basel).*, vol. 9, no. 12, p. 690, Dec. 2017.

[232] Liang Guo and S. P. DeWeerth, “Implementation of integratable PDMS-based conformable microelectrode arrays using a multilayer wiring interconnect technology,” in *2009 Annual International Conference of the IEEE Engineering in Medicine and Biology Society*, 2009, pp. 1619–1622.

[233] A. Lecestre, A. Lecomte, D. Bourrier, and P. Dubreuil, “Plasma etching of thick Parylene C for fabrication of biocompatible electrodes,” *Conf. PESM*, vol. 315, 2015.

[234] W. S. Konerding, U. P. Froriep, A. Kral, and P. Baumhoff, “New thin-film surface electrode array enables brain mapping with high spatial acuity in rodents,” *Sci. Rep.*, vol. 8, no. 1, 2018.

[235] A. A. Schendel *et al.*, “The effect of micro-ECoG substrate footprint on the meningeal tissue response,” *J. Neural Eng.*, vol. 11, no. 4, p. 046011, Aug. 2014.

[236] Specialty Coating Systems, “SCS Parylene Properties,” *Accessed From Http//Scscoatings.Com/Corporate/Library.Aspx*, p. 12, 2016.

[237] B. Lu, S. Zheng, B. Q. Quach, and Y.-C. Tai, “A study of the autofluorescence of parylene materials for microTAS applications.,” *Lab Chip*, vol. 10, no. 14, pp. 1826–34, 2010.

[238] E. Meng, P. Y. Li, and Y. C. Tai, “A biocompatible Parylene thermal flow sensing array,” *Sensors Actuators, A Phys.*, vol. 144, no. 1, pp. 18–28, 2008.

[239] X. Z. Xie, L. Rieth, P. Tathireddy, and F. Solzbacher, “Long-term in-vivo investigation of parylene-C as encapsulation material for neural interfaces,” *Procedia Eng.*, vol. 25, pp. 483–486, 2011.

[240] S. Kuppusami and R. H. Oskouei, “Parylene Coatings in Medical Devices and Implants: A Review,” *Univers. J. Biomed. Eng.*, vol. 3, no. 2, pp. 9–14, 2015.

[241] R. Huang, C. Pang, Y. C. Tai, J. Emken, C. Ustun, and R. Andersen, “Parylene coated silicon probes for neural prosthesis,” *3rd IEEE Int. Conf. Nano/Micro Eng. Mol. Syst. NEMS*, pp. 947–950, 2008.

[242] R. D. Frostig, S. A. Masino, M. C. Kwon, and C. H. Chen, “Using light to probe the brain:intrinsic signal optical imaging,” *Int.J.Imag.Syst.Technol.*, vol. 6, pp. 216–224, 1995.

[243] R. D. Frostig, *In Vivo Optical Imaging of Brain Function, Second Edition*, vol. 20091928. 2009.

[244] A. Grinvald *et al.*, “In-vivo Optical Imaging of Cortical Architecture and Dynamics,” in *Modern Techniques in Neuroscience Research*, Springer Berlin Heidelberg, 1999, pp. 893–969.

[245] H. D. Lu, G. Chen, J. Cai, and A. W. Roe, “Intrinsic signal optical imaging of visual brain activity:

Tracking of fast cortical dynamics," *Neuroimage*, vol. 148, pp. 160–168, Mar. 2017.

[246] R. A. Stepnoski, A. LaPorta, F. Raccuia-Behling, G. E. Blonder, R. E. Slusher, and D. Kleinfeld, "Noninvasive detection of changes in membrane potential in cultured neurons by light scattering," *Proc. Natl. Acad. Sci. U. S. A.*, vol. 88, no. 21, pp. 9382–9386, 1991.

[247] T. Bonhoeffer and A. Grinvald, "Optical imaging based on intrinsic signals: The methodology." 1996.

[248] A. Grinvald, E. Lieke, R. D. Frostig, C. D. Gilbert, and T. N. Wiesel, "Functional architecture of cortex revealed by optical imaging of intrinsic signals," *Nature*, vol. 324, no. 6095, pp. 361–364, 1986.

[249] A. J. Blood, S. M. Narayan, and A. W. Toga, "Stimulus Parameters Influence Characteristics of Optical Intrinsic Signal Responses in Somatosensory Cortex," *J. Cereb. Blood Flow Metab.*, vol. 15, no. 6, pp. 1109–1120, Nov. 1995.

[250] R. D. Frostig, E. E. Lieke, D. Y. Ts'o, and A. Grinvald, "Cortical functional architecture and local coupling between neuronal activity and the microcirculation revealed by in vivo high-resolution optical imaging of intrinsic signals," *Proc. Natl. Acad. Sci. U. S. A.*, vol. 87, no. 16, pp. 6082–6086, 1990.

[251] "Essential Overview of CCD Spatial Resolution - Andor Learning Centre." [Online]. Available: https://andor.oxinst.com/learning/view/article/ccd-spatial-resolution. [Accessed: 17-Jan-2020].

[252] V. Gautam, J. Drury, J. M. C. Choy, C. Stricker, H.-A. Bachor, and V. R. Daria, "Improved two-photon imaging of living neurons in brain tissue through temporal gating," *Biomed. Opt. Express*, vol. 6, no. 10, p. 4027, 2015.

[253] Z. F. Mainen, M. Maletic-Savatic, S. H. Shi, Y. Hayashi, R. Malinow, and K. Svoboda, "Two-photon imaging in living brain slices.," *Methods*, vol. 18, no. 2, pp. 231–9, 1999.

[254] J. Nakai, M. Ohkura, and K. Imoto, "A high signal-to-noise Ca2+ probe composed of a single green fluorescent protein," *Nat. Biotechnol.*, vol. 19, no. 2, pp. 137–141, Feb. 2001.

[255] B. P. Kerekes *et al.*, "Combined two-photon imaging, electrophysiological, and anatomical investigation of the human neocortex *in vitro*," *Neurophotonics*, vol. 1, no. 1, p. 011013, 2014.

[256] B. Chiovini *et al.*, "Enhanced Dendritic Action Potential Backpropagation in Parvalbumin-positive Basket Cells During Sharp Wave Activity," *Neurochem. Res.*, vol. 35, no. 12, pp. 2086–2095, Dec. 2010.

[257] A. Mitani and T. Komiyama, "Real-Time Processing of Two-Photon Calcium Imaging Data Including Lateral Motion Artifact Correction," *Front. Neuroinform.*, vol. 12, Dec. 2018.

[258] M. Brini, T. Calì, D. Ottolini, and E. Carafoli, "Neuronal calcium signaling: Function and dysfunction," *Cellular and Molecular Life Sciences*, vol. 71, no. 15. Birkhauser Verlag AG, pp. 2787–2814, 2014.

[259] C. Zhong and J. Schleifenbaum, "Genetically Encoded Calcium Indicators: A New Tool in Renal Hypertension Research," *Front. Med.*, vol. 6, Jun. 2019.

[260] A. Zátonyi *et al.*, “Functional brain mapping using optical imaging of intrinsic signals and simultaneous high-resolution cortical electrophysiology with a flexible, transparent microelectrode array,” *Sensors Actuators B Chem.*, vol. 273, pp. 519–526, Nov. 2018.

[261] W. L. Ong, Q. X. Low, W. Huang, J. A. Van Kan, and G. W. Ho, “Patterned growth of vertically-aligned ZnO nanorods on a flexible platform for feasible transparent and conformable electronics applications,” *J. Mater. Chem.*, vol. 22, no. 17, pp. 8518–8524, 2012.

[262] V. Prajzler, P. Nekvindova´, P. Hypsˇ, O. Lyutakov, and V. Jerˇa´bek, “Flexible polymer planar optical waveguides,” *Radioengineering*, vol. 23, no. 3, pp. 776–782, 2014.

[263] J. Liu, G. Zong, L. He, Y. Zhang, C. Liu, and L. Wang, “Effects of fumed and mesoporous silica nanoparticles on the properties of sylgard 184 polydimethylsiloxane,” *Micromachines*, vol. 6, no. 7, pp. 855–864, 2015.

[264] K. Y. Kwon, B. Sirowatka, W. Li, and A. Weber, “Opto-??ECoG array: Transparent ??eCoG electrode array and integrated LEDs for optogenetics,” *2012 IEEE Biomed. Circuits Syst. Conf. Intell. Biomed. Electron. Syst. Better Life Better Environ. BioCAS 2012 - Conf. Publ.*, pp. 164–167, 2012.

[265] K. Alzoubi, M. M. Hamasha, S. Lu, and B. Sammakia, “Bending fatigue study of sputtered ITO on flexible substrate,” *IEEE/OSA J. Disp. Technol.*, vol. 7, no. 11, pp. 593–600, 2011.

[266] K. Ohki, S. Chung, P. Kara, M. Hübener, T. Bonhoeffer, and R. C. Reid, “Highly ordered arrangement of single neurons in orientation pinwheels,” *Nature*, vol. 442, no. 7105, pp. 925–928, Aug. 2006.

[267] P. Buzás, K. Kovács, A. S. Ferecskó, J. M. L. Budd, U. T. Eysel, and Z. F. Kisvárday, “Model-based analysis of excitatory lateral connections in the visual cortex,” *J. Comp. Neurol.*, vol. 499, no. 6, pp. 861–881, Dec. 2006.

[268] N. Brunet, M. Vinck, C. A. Bosman, W. Singer, and P. Fries, “Gamma or no gamma, that is the question,” *Trends in Cognitive Sciences*, vol. 18, no. 10. Elsevier Ltd, pp. 507–509, 01-Oct-2014.

[269] N. Brunet *et al.*, “Visual cortical gamma-band activity during free viewing of natural images,” *Cereb. Cortex*, vol. 25, no. 4, pp. 918–926, Apr. 2015.

[270] D. Hermes, K. J. Miller, B. A. Wandell, and J. Winawer, “Stimulus dependence of gamma oscillations in human visual cortex,” *Cereb. Cortex*, vol. 25, no. 9, pp. 2951–2959, Sep. 2015.

[271] C. M. Lewis, C. A. Bosman, T. Womelsdorf, and P. Fries, “Stimulus-induced visual cortical networks are recapitulated by spontaneous local and interareal synchronization,” *Proc. Natl. Acad. Sci. U. S. A.*, vol. 113, no. 5, pp. E606–E615, Feb. 2016.

[272] J. M. Hsu, L. Rieth, R. A. Normann, P. Tathireddy, and F. Solzbacher, “Encapsulation of an integrated neural interface device with parylene C,” *IEEE Trans. Biomed. Eng.*, vol. 56, no. 1, pp. 23–29, 2009.

[273] R. Description, F. M. Properties, and F. E. Properties, “SU-8 Permanent Photoresists SU-8 Permanent Photoresists,” 2000.

[274] K. W. Meacham, R. J. Giuly, L. Guo, S. Hochman, and S. P. DeWeerth, “A lithographically-

patterned, elastic multi-electrode array for surface stimulation of the spinal cord," *Biomed. Microdevices*, vol. 10, no. 2, pp. 259–269, 2008.

[275] F. Sarabia, "HD Microsystems Polyimide PI 2611," pp. 5–6.

[276] A. Mata, A. J. Fleischman, and S. Roy, "Characterization of polydimethylsiloxane (PDMS) properties for biomedical micro/nanosystems.," *Biomed. Microdevices*, vol. 7, no. 4, pp. 281–293, 2005.

[277] P. Details, A. A. Promoter, and A. P. Precursor, "PI-2600 Series – Low Stress Applications," *Stress Int. J. Biol. Stress*, no. September, pp. 1–4, 2009.

[278] T. Czvikovszky, P. Nagy, and J. Gaál, "A polimertechnika alapjai," pp. 1–453, 2000.

[279] J. E. Mark, *Physical Properties of Polymers Handbook*. 2007.

[280] Y. Qin, M. M. R. Howlader, M. J. Deen, Y. M. Haddara, and P. R. Selvaganapathy, "Polymer integration for packaging of implantable sensors," *Sensors Actuators, B Chem.*, vol. 202, pp. 758–778, 2014.

[281] Y.-L. Lai, Y.-K. Lai, C.-Y. Zheng, G.-H. Xu, Y.-M. Wang, and S.-C. Chen, "Fabrication of working and counter electrodes on plastic substrates for flexible dye-sensitized solar cells," *MATEC Web Conf.*, vol. 123, p. 00031, 2017.

[282] P. Rezai, W.-I. Wu, and P. R. Selvaganapathy, "Mems for Biomedical Applications," *Mems Biomed. Appl.*, pp. 3–45, 2012.

[283] C. Heo *et al.*, "A soft, transparent, freely accessible cranial window for chronic imaging and electrophysiology," *Sci. Rep.*, vol. 6, Jun. 2016.

[284] D. Kuzum *et al.*, "Transparent and flexible low noise graphene electrodes for simultaneous electrophysiology and neuroimaging," *Nat. Commun.*, vol. 5, no. May, pp. 1–10, 2014.

[285] D. A. Borkholder, "CELL BASED BIOSENSORS USING MICROELECTRODES," 1998.

[286] D. W. Kumsa, N. Bhadra, E. M. Hudak, S. C. Kelley, D. F. Untereker, and J. T. Mortimer, "Electron transfer processes occurring on platinum neural stimulating electrodes: a tutorial on the i (V_e) profile," *J. Neural Eng.*, vol. 13, no. 5, p. 052001, 2016.

[287] A. Campbell and C. Wu, "Chronically implanted intracranial electrodes: Tissue reaction and electrical changes," *Micromachines*, vol. 9, no. 9. MDPI AG, 2018.

[288] G. Buzsáki, C. a Anastassiou, and C. Koch, "The origin of extracellular fields and currents--EEG, ECoG, LFP and spikes.," *Nat. Rev. Neurosci.*, vol. 13, no. 6, pp. 407–20, 2012.

6 ACKNOWLEDGEMENT

I would like to express my thanks to all the people whose contribution was indispensable for the completion of the work presented in this thesis.

I would like to express my sincere thanks to my supervisor, Dr. Zoltán Fekete for overall guiding and support, manuscript reading and corrections through the 3 years of my PhD study.

Dr. Péter Fürjes, who provided good conditions to conduct experiments in the clean room of the Microsystems Lab in the Centre for Energy Research.

I want to thank to the cleanroom personnel of CE, for their precise work and persistent support during micromachining processes, especially to Páyer Károlyné who managed my work regarding microfabrication technology, Attila Nagy who did incredible work during packaging of microdevices and Levente Illés who guided my work with SEM measurements.

I consider myself very lucky that many of my colleagues I can also call friends.

I would like to express my gratitude to Dr. Gergely Márton, Dr. Zoltán Kisvárday, Dr. Zsolt Borhegyi, Dr. Zoltán Somogyvári and Gábor Orbán to assist with the in vivo validation of microdevice performance.

I am glad to acknowledge the enormous support I received from the NeuroMEMS research group, including Dr. Anita Pongrácz, Flóra Zsófia Fedor, Róbert Hodován, Ágnes Szabó, Ágoston Csaba Horváth, Bence Csernyus and Csaba Lázár.

I am thankful for the support I received from students, Zita Zsiros, Anna Hoyle, Luca Sinkó and Krisztián Fekete.

I am also very grateful to my family and I cannot forget my friends, which are the salt and pepper of my life, they have made these years easier and unforgettable. Thank you Dániel for all your appreciation, extraordinary patience and persistent support during these years, especially during the last few moths.

Without the help of all of you all, nothing of this would have been possible.

I wish to thank the support of the National Research, Development and Innovation Office (grant: NKFIH K 120143) and the National Brain Research Program (2017_1.2.1_NKP-2017-00002) is acknowledged.

I hope to have not forgotten anyone, in any case thank you for these years so full and meaningful both from scientific and human point of view!

7 LIST OF ACRONYMS

ACSF	Artificial Cerebrospinal Fluid
AP	Action Potential
BCI	Brain Computer Interface
CNS	Central Nervous System
CNT	Carbon Nanotube
CP	Conductive Polymer
CPE	Constant Phase Element
CVP	Chemical Vapor Deposition
DMA	Dimethylacrylate
DRIE	Deep Reactive Ion Etching
ECM	Extracellular Matrix
ECoG	Electrocorticography
EEG	Electroencephalography
FBR	Foreign Body Response
FDA	U.S. Food and Drug Administration
FIB	Focused Ion Beam
FP	Field Potential
ISO	International Organization for Standardization
LCP	Liquid Crystal Polymer
LFP	Local Field Potential
MEA	Microelectrode Array
MEMS	Microelectromechanical System
MRI	Magnetic Resonance Imaging
NCs	Nanocomposites

NMs	Nanomembranes
NWs	Nanowires
PBS	Phosphate Buffer Saline
PDMS	Polydimethylsiloxane
PEDOT	Poly(3,4-ethylenedioxythiophene)
PEEK	Polyetheretherketone
PEG	Polyethylene glycol
PI	Polyimide
PLGA	Poly(lactic-*co*-glycolic acid)
PMMA	Poly(methyl methacrylate)
PPX	Poly(para-xylylene)
PSS	Polystyrene sulfonate
PVA	Polyvinyl alcohol
RIE	Reactive Ion Etching
SEM	Scanning Electron Microscopy
Si	Silicon
SMP	Shape-memory Polymer
SNR	Signal-to-Noise Ration

Appendix A – Microelectrode design for polyimide – based μECoG devices related to *Chapter 3*